

An apparatus
for the measurement
of the electronic spectra of cold ions
in a radio-frequency trap

Inauguraldissertation

Zur Erlangung der Würde eines Doktors der Philosophie
vorgelegt der Philosophisch-Naturwissenschaftlichen Fakultät
der Universität Basel

von

Anatoly Dzhonson
aus Poronaisk (Russland)

Basel, 2007

Genehmigt von der Philosophisch-Naturwissenschaftlichen Fakultät
aus Antrag von
Prof. Dr. John P. Maier und Prof. Dr. Martin Jungen

Basel, den 13. Februar 2007

Prof. Dr. Hans-Peter Hauri

Dekan

To my parents and cat

Acknowledgments

I would like to thank Prof. Dr. John P. Maier for giving me the opportunity to work in his group. The challenging project he proposed prepared me to be ready to take responsibility and make my own decisions, both now and in the future. The excellent working environment and resources available during my studies are greatly appreciated.

Dr. Timothy Schmidt (The University of Sydney, Australia) and Dr. Przemyslaw Kolek (University of Krakow, Poland) are thanked for their help during the initial stages of the instrument's construction. Many thanks to Prof. Dr. Dieter Gerlich (Technical University of Chemnitz, Germany) for his help in the development of the apparatus. Prof. Dr. Evan Bieske (University of Melbourne, Australia) is greatly thanked for his help while collecting spectra of the first trapped ions, and for useful suggestions involving the operating scheme of the whole experiment.

I am also grateful to the people who were technically involved in the experiment: Dieter Wild and Grischa Martin (mechanical workshop) for machining the various vacuum chambers and associated components of the apparatus. The experiment setup is still supported and continuously improved by the workshop. Jacques Lecoultre is also thanked for providing exotic chemical substances and Georg Holderied for building up TTL fast switch, power supplies, RF generators and many other very useful electronic devices, without which the experiment would not work. Thanks to Georg Holderied for being always ready to assist with technical advice.

My sincere appreciations are given to Esther Stalder and Daniela Tischhauser, from secretary the office, for taking care of bureaucratic matters and making life easier. Thanks to Dr. Evan Jochnowitz for his help in correcting this thesis, for scientific discussion and English lessons.

This project has been supported by the Swiss National Science Foundation (No. 200020-100019).

I also would like to thank Prof. Dr. Martin Jungen for acting as the co-referee of this thesis.

TABLE OF CONTENTS

CHAPTER 1	INTRODUCTION.....	8
1.1	INTERSTELLAR MEDIUM.....	8
1.1.1	<i>A brief overview of ISM.</i>	8
1.1.2	<i>A classification of the ISM.</i>	11
1.1.2.1	Dark nebulae.....	11
1.1.2.2	Reflection nebulae.....	12
1.1.2.3	H _{II} regions.....	12
1.1.2.4	Planetary nebulae.....	12
1.1.2.5	Supernova remnants.....	12
1.2	IONS OF ASTROPHYSICAL INTEREST.....	14
1.3	LABORATORY ELECTRONIC SPECTROSCOPY ON MOLECULAR IONS.....	18
1.3.1	<i>N₂O and 1,4-dichlorobenzene cations.</i>	18
1.3.2	<i>2,4-hexadiyne cation.</i>	20
1.3.3	<i>Polyacetylene cations.</i>	22
1.3.4	<i>Protonated polyacetylene cations.</i>	24
CHAPTER 2	EXPERIMENTAL.....	26
2.1	APPARATUS.....	26
2.1.1	<i>Ion source.</i>	28
2.1.2	<i>Quadrupole mass filter.</i>	32
2.1.2.1	Technical details.....	32
2.1.2.2	Principle of operation.....	34
2.1.3	<i>22-pole radio frequency ion trap.</i>	38
2.1.3.1	Technical details.....	38
2.1.3.2	Principle of operation.....	41
2.1.4	<i>Daly detector.</i>	43
2.2	LASER OPTICAL SCHEME.....	46
2.2.1	<i>One-colour experiment.</i>	46
2.2.2	<i>Two-colour experiment.</i>	48
2.3	SOFTWARE AND DATA ACQUISITION CARDS.....	51
2.3.1	<i>ABB Extrel mass spectrometer.</i>	51
2.3.2	<i>Nermag mass spectrometer.</i>	55
2.3.3	<i>Sunlight EX OPO laser spectrometer.</i>	59
2.3.4	<i>Data acquisition cards and electrical connection.</i>	63
2.3.4.1	PCI-6023E (device 1).....	64
2.3.4.2	PCI-6713 (device 2).....	65
2.3.4.3	PCI-DAS6014 (device 3).....	67
2.3.4.4	DAQ cards electrical connections.....	69
2.3.4.5	Software pulse generator.....	70
2.4	EXPERIMENTAL APPROACH.....	72
CHAPTER 3	RESULTS AND DISCUSSION.....	75
3.1	ONE-PHOTON TWO-COLOUR PHOTOFRAGMENTATION SPECTROSCOPY.....	75
3.1.1	<i>N₂O cation.</i>	75
3.1.2	<i>2,4-hexadiyne cation.</i>	76
3.1.2.1	Internal temperature of 2,4-hexadiyne cation.....	76
3.1.2.2	Vibrational structure.....	80

3.2	TWO-PHOTON ONE-COLOUR PHOTOFRAGMENTATION SPECTROSCOPY.	84
3.2.1	<i>1,4-dichlorobenzene cation.</i>	84
3.3	TWO-PHOTON TWO-COLOUR PHOTOFRAGMENTATION SPECTROSCOPY.	91
3.3.1	<i>Polyacetylene cations.</i>	91
3.3.2	<i>Protonated polyacetylene cations.</i>	96
CHAPTER 4	CONCLUSIONS.....	106
CHAPTER 5	OUTLOOK.	109
BIBLIOGRAPHY.....		111

Chapter 1 Introduction.

1.1 Interstellar medium.

While most cosmologists cannot agree on what happened during the first second after the Big Bang, the prevailing viewpoint describes an infinitely hot, dense point that expanded, thinned and cooled to 10^{15} K. The inflation era lasted from 10^{-34} to 10^{-32} s, followed by a change in density and temperature of several orders of magnitude during the first 10^{-12} seconds. During the following 10^{-5} seconds, quarks had fused into protons and neutrons, primordial nucleosynthesis ended, thus producing atoms and ions. The universe became transparent at 3×10^5 years, forming simple molecules, the heaviest of which was lithium hydride, and leaving only the 2.7 K microwave background as a relic of its initially violent beginnings. After 10^9 years, the first galaxies and quasars formed. While galaxies are not forming at the present epoch, the stars within them are, 15 billion years after the Big Bang. The tenuous matter spread across the vast distances between the stars totals just a few percent of the weight of all the visible stars in our own Galaxy and is termed the interstellar medium (ISM).

1.1.1 A brief overview of ISM.

The ISM has two main components: bright and dark regions of mainly hydrogen and helium gas, and dark swathes of dust. These are termed inhomogeneous due to their non-uniform distribution. Most of the ISM is contained within the Galactic disk and the spiral arms in a layer a few hundred parsecs thick.

One cannot explicitly say that the space between the stars is a vacuum, since the ISM is clearly observable. It contains on average only one atom per cm^3 ; fewer atoms than even the best terrestrial laboratory vacuum can achieve. Any chemistry occurring in space will depend on cosmic abundance of a particular element. Table 1 shows the abundance of the most common atoms relative to the hydrogen atom.

Table 1 Fractional abundance of elements relative to hydrogen.

Element	Abundance
H	1
He	0.1
O	7×10^{-4}
C	3×10^{-4}
N	1×10^{-4}
Ne	0.8×10^{-4}
Si	0.3×10^{-4}
Mg	0.3×10^{-4}
S	0.2×10^{-4}
Fe	0.04×10^{-4}

Until 1968, astronomers assumed that the ISM was mostly atomic hydrogen with significantly fewer of the hydrogen atoms being bound with a single carbon or oxygen. Then ammonia NH_3 was discovered near the Galactic center, followed by water vapor H_2O ; thereafter successively more complex molecules such as ethanol $\text{CH}_3\text{CH}_2\text{OH}$ were observed. Table 2 gives a summary of the interstellar molecules observed to date. Currently it is known that the ISM is the site of a complex and varied chemistry that is very different to that one can study on earth.

Table 2 The interstellar molecules found (January 2007).

Number of atoms	Compound
2	H ₂ , AlF, AlCl, C ₂ , CH, CH ⁺ , CN, CO, CO ⁺ , CP, CSi, HCl, KCl, NH, NO, NS, NaCl, OH, PN, SO, SO ⁺ , SiN, SiO, SiS, CS, HF, SH, FeO(?)
3	C ₃ , C ₂ H, C ₂ O, C ₂ S, CH ₂ , HCN, HCO, HCO ⁺ , HCS ⁺ , HOC ⁺ , H ₂ O, H ₂ S, HNC, HNO, MgCN, MgNC, N ₂ H ⁺ , N ₂ O, NaCN, OCS, SO ₂ , c-SiC ₂ , CO ₂ , NH ₂ , H ₃ ⁺ , SiCN, AlNC, SiNC
4	c-C ₃ H, l-C ₃ H, C ₃ N, C ₃ O, C ₃ S, C ₂ H ₂ , CH ₂ D ⁺ (?), HCCN, HCNH ⁺ , HNCO, HNCS, HOCO ⁺ , H ₂ CO, H ₂ CN, H ₂ CS, H ₃ O ⁺ , NH ₃ , SiC ₃ , C ₄
5	C ₅ , C ₄ H, C ₄ Si, l-C ₃ H ₂ , c-C ₃ H ₂ , CH ₂ CN, CH ₄ , HC ₃ N, HC ₂ NC, HCOOH, H ₂ CHN, H ₂ C ₂ O, H ₂ NCN, HNC ₃ , SiH ₄ , H ₂ COH ⁺
6	C ₅ H, l-H ₂ C ₄ , C ₂ H ₄ , CH ₃ CN, CH ₃ NC, CH ₃ OH, CH ₃ SH, HC ₃ NH ⁺ , HC ₂ CHO, NH ₂ CHO, C ₅ N, HC ₄ N
7	C ₆ H, CH ₂ CHCN, CH ₃ C ₂ H, HC ₅ N, HCOCH ₃ , NH ₂ CH ₃ , c-C ₂ H ₄ O, CH ₂ CHOH
8	CH ₃ C ₃ N, HCOOCH ₃ , CH ₃ COOH(?), C ₇ H, H ₂ C ₆ , CH ₂ OHCHO, CH ₂ CHCHO
9	CH ₃ C ₄ H, CH ₃ CH ₂ CN, (CH ₃) ₂ O, CH ₃ CH ₂ OH, HC ₇ N, C ₈ H
10	CH ₃ C ₅ N(?), (CH ₃) ₂ CO, NH ₂ CH ₂ COOH(?), CH ₃ CH ₂ CHO
11	HC ₉ N
12	CH ₃ OC ₂ H ₅
13	HC ₁₁ N

The gaseous component consists of a mixture of atoms and molecules and these may be ionized or neutral. The dust component comprises only 1% of the ISM by mass and consists of *stardust*, which is composed of silicates, graphite and amorphous carbon, made in oxygen- and carbon-rich outflows from late-type giants and planetary nebulae. *Interstellar dust*, which is formed in the interstellar medium, consists of silicates and carbonaceous components, ranging in size from a few microns down to several Angstroms. There is only indirect evidence to suggest that most interstellar dust formation occurs in the *ambient* ISM. Despite its small relative mass, dust plays a key role in the thermodynamics and chemistry of both the ISM and star formation.

Interstellar gas is transparent to photons with energies less than 13.6 eV (the Lyman limit); that is, electromagnetic radiation ranging from the ultraviolet (UV) to the far-infrared (FIR). Dust grains act as thermal intermediaries between photons and gas because they absorb light with extreme efficiency. That is why dust looks dark on optical photographs. The actual effect of

the dust is that it both absorbs and scatters light; collectively called *extinction*. This allows indirect shielding from UV light such that complex, organic molecules can be formed in the gas phase and as ices on the surface of the grains themselves. The extremely varied physical conditions (such as temperature, pressure and different types of electromagnetic radiation) existing within the ISM produce a highly interesting and complex chemistry. Ultimately, interstellar chemistry will produce the raw material available for the formation of planets and life itself. These presolar molecules can be identified from samples buried in cometary and meteoric matter. Without dust, the evolution of our Galaxy would have been very different and the development of planetary systems would not have occurred.

1.1.2 A classification of the ISM.

The gas clouds comprising the ISM are termed *gaseous nebulae* and are highly dynamic structures with relative speeds $\sim 10 \text{ km s}^{-1}$. The following regions are differentiated: dark nebulae, reflection nebulae, H II regions, planetary nebulae, supernova remnants.

1.1.2.1 Dark nebulae.

Dark nebulae can be observed because they obscure background stars or stand out as dark patches against regions of hot, glowing gases. Some are spherically shaped and self-gravitating, named *Bok globules*, and are proposed as sites of star formation in giant molecular clouds complexes. These Bok globules should not be confused with a class of smaller Bok globules seen against ionized regions of ISM, which are not gravitationally bound. Molecular cloud complexes are cool, have a lifetime of order 10^7 years, and as their name suggests, are a rich source of molecules such as hydrogen H_2 and carbon monoxide CO.

1.1.2.2 Reflection nebulae.

A reflection nebulae is a cloud of gas and dust which shines by reflecting light emanating from stars (containing the star's absorption spectrum). This light is scattered by dust grains in the surrounding gas, revealing their presence. The reflection nebula appear bluer than the light coming directly from the stars due to blue light being preferentially scattered relative to red light.

1.1.2.3 H_{II} regions.

H_{II} regions exist where neutral hydrogen (H_I) atoms are exposed to photons of energy greater than 13.6 eV from stars. These photons ionize the hydrogen atoms to form protons and electrons. H_{II} regions are thus bright, ionized regions of hydrogen surrounding newborn hot, bright stars (of spectral types O and B) These region are dominated by intense light emission and thermal radio-continuum. The division between an H_I and H_{II} regions is distinct and resulting sphere of ionized hydrogen around the star.

1.1.2.4 Planetary nebulae.

These are similar to H_{II} regions except that the ionizing source is an old star in its death throes rather than a newborn star. The resulting ionized region is more chemically complex, dense and compact.

1.1.2.5 Supernova remnants.

Supernovae can be roughly classified as Type I or Type II. A Type I supernova occurs in typical binary stars, which consists of a low to medium mass star, which is in the process

of evolving into a red giant phase, and a companion star, which can be a white dwarf, a Wolf-Rayet star, or a helium star. The expanding outer layers of the red giant are effectively dumped onto the surface of the companion star; a process that increases the pressure, and thus temperature, inside the star. At a certain moment in time a fusion process starts in the carbon-rich interior of the companion star, releasing the remaining nuclear energy in a process termed *deflagration*. Deflagration involves the breakup of the entire companion star, leaving only an interstellar rubble.

A Type II supernova occurs when a high-mass star explodes in its last stages of evolution. Generally, it leaves gaseous remnants and a high-density neutron star. If the remnant is young, there will exist an amorphous region emitting a continuous spectrum of synchrotron radiation by electrons spiraling in intense magnetic fields. This (radio) emission from supernovae has thus a non-thermal origin. The X-ray and optical emission from supernova remnants, on the other hand, is thermal radiation arising from shock heating.

Table 3 summaries the physical conditions in the five general types of ISM.

Table 3 A broad classification of five types of interstellar medium.

Phase	η_{H} (cm^{-3})	T_{gas} (K)	% ISM by volume	% ISM by mass
Molecular cloud	10^2 - 10^5	20	< 1	~ 40
H _I regions [cloud]	15	10^2	~ 3	~ 40
H _I regions [intercloud]	0.5	6×10^3 - 10^4	~ 47	~ 20
H _{II} regions	10 - 10^3	10^4	< 1	
Supernova remnants	10^{-3}	10^6	~ 50	

1.2 Ions of astrophysical interest.

The article by A. Douglas published in 1977 proposing that carbon chains are good candidates as carriers of some diffuse interstellar band absorption [1] has continued to be cited. His arguments were based on their likely spectroscopic and photophysical properties; i.e. leading to electronic transitions in visible part of the spectrum and possible broadenings of the absorptions due to intramolecular processes. In order to test this hypothesis, gas phase electronic spectra of the systems he was alluding to, e.g. the bare carbon chains C_n ($n=5, 7, \dots, 15$) were required. Thus as part of research activity of group of Prof. Dr. J.P. Maier dealing with the development and application of the methods to study the electronic spectra of radicals and ions we set ourselves the goal of measuring these spectra in the gas phase.

As a first step the electronic absorption spectra were obtained in neon matrices at 6 K. This was achieved using a cesium sputter source to produce the carbon anions, C_n^- , then co-deposition of the mass-selected species with excess of neon to trap the anions in the matrix thus formed, and finally the neutral entities were generated by photodetachment of the electrons. By this means the electronic spectra of the carbon chains anions, C_n^- $n=3-13$, neutrals C_n $n=4-21$ [2], and most recently of cations, C_n^+ $n=6-9$ [3], could be observed and identified. With this information in hand, gas phase spectra of those species possessing electronic transitions in the DIB range [4], 400-900 nm, were aimed for. These were obtained for a number of carbon cation, neutral and anion chains using supersonic free jets through which a discharge runs. With acetylene seeded in a rare gas numerous such carbon chains can be produced as diagnosed by mass-spectrometry. The electronic transitions were then observed in absorption with pulsed and cw cavity ringdown methods for the cations and neutrals and photodetachment processes for anions. This in turn allowed for the first time a direct comparison of laboratory spectra with astronomical measurements [5].

All the comparisons proved negative, including those for bare carbon chains C_4 , C_5 [6] and for species which are known to be present in diffuse medium, e.g., C_3H [7]. However the upper limits to the column densities derived, typically $<10^{12} \text{ cm}^{-2}$, are consistent with the values obtained for the species detected by rotational spectroscopy [8]. Thus even though species with column densities around the latter values can be detected in the mm-range, the relatively modest values of the oscillator strengths of the electronic transitions, e.g. around 0.004 for C_3H with origin band near 521 nm [7], would lead to DIB with an equivalent width (EW) of less than $1 \text{ m}\text{\AA}$, a hardly detectable DIB. Several such comparisons, lead to the conclusion that Douglas's hypothesis that carbon chains C_n with n lying in the range 5 - 15 are good DIB candidates can be excluded [9]. More generally, this statement applies not only to the bare carbon chains but to also to their derivatives such as those containing a hydrogen, C_nH , comprising up to around a dozen of atoms.

The consequences of this are illustrated with reference to study, which detected C_3 in diffuse clouds [10] and summarized in Table 4.

Table 4 Estimation of column density of a longer carbon chains based on the expected oscillator strength of its ${}^1\Sigma_u^+ \leftarrow X \text{ } {}^1\Sigma_g^+$ transition and the observation made for a rotational line in the ${}^1\Pi_u \leftarrow X \text{ } {}^1\Sigma_g^+$ system of C_3 in diffuse clouds (ref [10]).

	EW (\AA)	f	N (cm^{-2})
C_3	$\sim 10^{-4}$	$\sim 10^{-2}$	10^{10}
$C_{n\sim 21}$	$\sim 10^{-1}$	~ 10	10^{11}

The rotational lines identified corresponded to interstellar absorption lines with EW of $0.1 \text{ m}\text{\AA}$ and summing over all the rotational lines gave a total column density of around 10^{12} cm^{-2} (the N value given in Table 4 is for an individual rotational level of C_3). The electronic transition detected, the origin band of the $A \text{ } {}^1\Pi_u \leftarrow X \text{ } {}^1\Sigma^+$ Comet band system, has an oscillator strength of ~ 0.02 . Thus to observe one of the stronger, narrower DIBs, with EW of 0.1 \AA and FWHM

around 1 \AA , either the column density of the species has to be two orders of magnitude larger than for C_3 or the oscillator strength, f , has to be correspondingly bigger. The latter is the situation with the C_{2n+1} chains for their $A \ ^1\Sigma_u^+ \leftarrow X \ ^1\Sigma_g^+$ transition. This transition is found around 170 nm for C_3 with an f value of around unity [11]. The wavelength of the transition shifts by regular increments with the length of the carbon chains as can be seen in Figure 1-1 and f scales nearly with n .

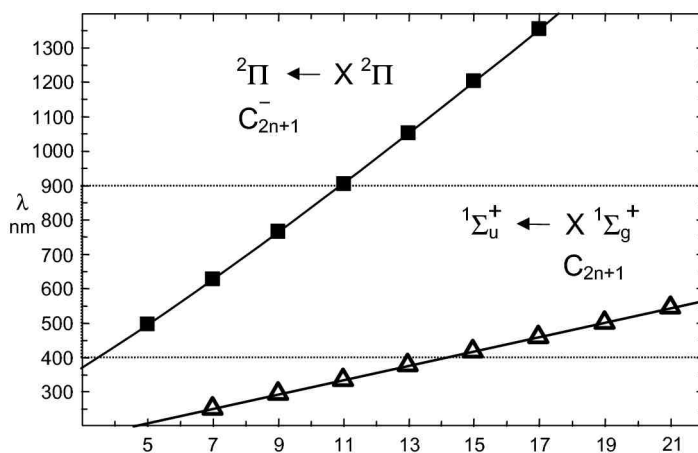


Figure 1-1 Wavelength dependence of the electronic transition (origin band) on the number of carbon atoms for two series of carbon chains. The 400-900 nm DIB range is indicated.

Thus these odd-numbered chains C_{17} , C_{19} ... up to, say, C_{31} have these electronic transitions in the 400-900 nm DIB region with f values in the 1-10 range. Their spectra have been observed in absorption in 6 K neon matrices for up to C_{21} [12]. In Table 4 C_{21} is taken as the example: to obtain a DIB with EW of 0.1 \AA would require a column density of 10^{11} cm^{-2} , not an excessive amount. As a consequence the current goal is to obtain the spectra of the chains of this size, as yet unsuccessfully.

The approach used for this purpose is resonance enhanced two-photon ionization (RE2PI) combined with a laser vaporization source as illustrated by Figure 1-2.

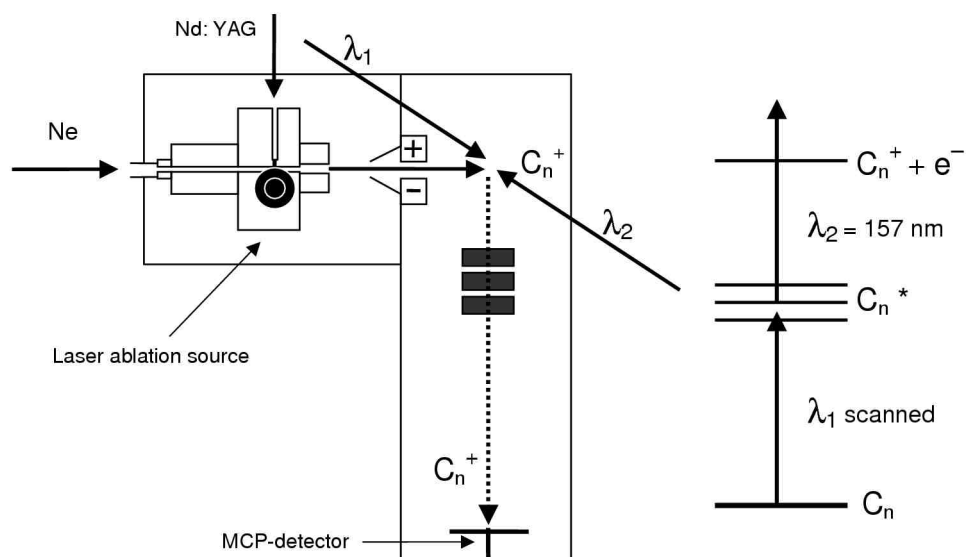


Figure 1-2 Technique used to measure the electronic spectra of the C_{18} ring in the gas phase involving a two-colour excitation ionization scheme.

A tunable laser (λ_1) scans the region where the electronic transitions are expected in view of the spectra observed in neon matrices, and subsequently ionization is induced with a F_2 157 nm laser (λ_2). As the mass-spectrum in Figure 1-3 shows, the sought after C_{17} , C_{19} ... species are formed.

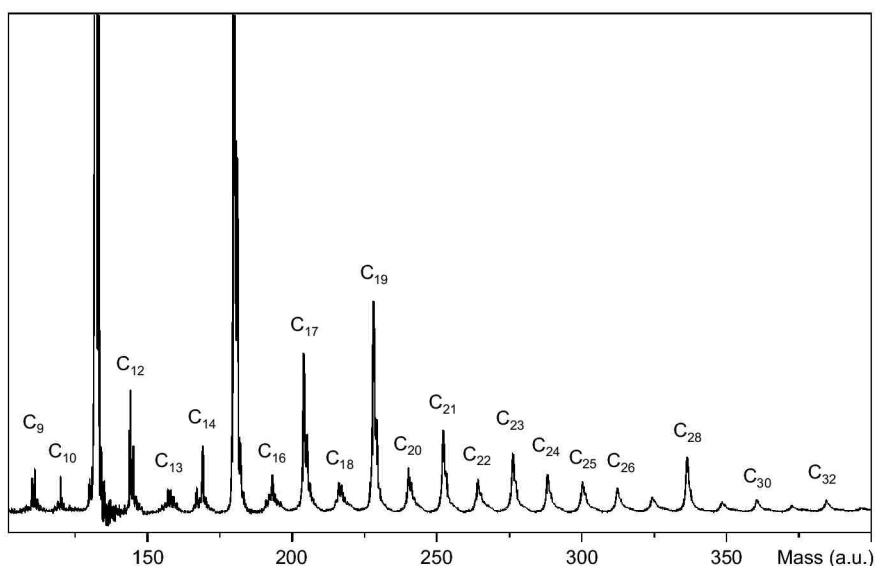


Figure 1-3 Typical mass-spectrum obtained from the laser vaporization source, using a 157 nm laser for the two-photon ionization.

However the RE2PI approach using nanosecond lasers failed to detect the transitions suggesting that the lifetimes of the excited electronic states are in the picosecond range. On the other hand the electronic spectra of C_{18} and C_{22} could be observed [13].

The similarity of the C_{18} origin band profile to the DIBs may suggest that one should look also for the laboratory spectra of cyclic ring cations with large oscillator strength. For such a purpose we have built up an instrument based on 22-pole trap to measure such spectra of large cations, which have been collisionally equilibrated to 20-30 K temperatures pertinent to the diffuse interstellar clouds. Low rotational temperatures are more easily obtained in supersonic free jets, but the vibrational modes are not cooled. The first measurements with this instrument were to demonstrate that both the rotations and vibrations have been relaxed.

1.3 Laboratory electronic spectroscopy on molecular ions.

1.3.1 N_2O and 1,4-dichlorobenzene cations.

A significant challenge remains the measurement of the electronic spectra of large molecular ions in the gas phase and at low internal temperature. Problems include low ion densities and spectral congestion due to the presence of species with overlapping absorptions and vibrational hot bands. Sometimes it is feasible to generate sufficient densities of molecular ions in a plasma or discharged supersonic expansion so that laser absorption, laser induced fluorescence, or cavity ringdown spectra can be recorded. However, due to the chemical complexity of plasma environments there are often difficulties in associating spectral features with a particular molecular species.

An alternative approach to obtaining electronic spectra is by resonance enhanced photodissociation, exposing the molecular ions to a tuneable laser beam in a tandem mass spectrometer while detecting photofragment ions as a function of laser wavelength. The advantages are that the parent molecular ions and photofragments can be mass-selected removing any ambiguity in their identity, and that the photofragments can be detected with almost unit efficiency conferring high sensitivity. In some cases, such as N_2O^+ , it is possible to access predissociative rovibronic states through the absorption of a single visible or UV photon. Alternatively, if a single photon does not provide sufficient energy to fragment the molecule it is possible that absorption of multiple photons will. For example, many organic ions undergo rapid internal conversion from excited electronic states, yielding vibrationally hot ions in the ground electronic state. If the vibrational energy exceeds the fragmentation threshold, the ions can dissociate. Otherwise, the absorption/internal conversion process can continue until the ions have sufficient energy to dissociate.

The resonance enhanced photodissociation approach has been used for many years employing a variety of different mass spectrometers and ion traps. [14] One common difficulty is that the molecular ions have considerable internal energy due to the violence of the ionisation process, so that the electronic spectra are congested and difficult to interpret. This is a particular problem for larger molecules. In order to circumvent this difficulty an apparatus has been developed in which the ions' rotational and vibrational degrees of freedom are deactivated by helium buffer gas collisions in a cryogenically cooled 22-pole radio frequency trap. In this paper the technique's advantages are illustrated by presenting the rotationally resolved $\tilde{A} \ ^2\Sigma^+ \leftarrow \tilde{X} \ ^2\Pi_{3/2}^+$ spectrum of N_2O^+ and the vibrationally resolved $\tilde{B} \ ^2B_{3u} \leftarrow \tilde{X} \ ^2B_{2g}$ spectrum of the $p\text{-DCB}^+$ radical cation. Both molecular ions have been subject to previous studies. The N_2O^+ cation is well understood having been investigated extensively through optical emission, [15] lifetime, [16] and photodissociation studies. [17-19] Previously, the N_2O^+ $\tilde{A} \ ^2\Sigma^+ \leftarrow \tilde{X} \ ^2\Pi_{3/2}^+$ electronic spectrum has been obtained by detecting the NO^+ fragment,

a strategy that is effective because the higher vibronic levels of the $\tilde{A} \ ^2\Sigma^+$ state are predissociative and lead to production of NO^+ and O atom fragments. For the 1^2 level of the $\tilde{A} \ ^2\Sigma^+$ state, which is accessed in the current study, around 16 % of the molecules fluoresce with the remainder dissociating. [16]

The $p\text{-DCB}^+$ radical cation was investigated initially using the techniques of photoelectron and emission spectroscopies in a molecular beam, [20] and later by absorption in the rare gas matrixes. [21, 22] From pulsed electron beam excitation and emission intensity measurements it has been estimated that the internal conversion rate is $\approx 10^{11} \text{ s}^{-1}$. [20] As discussed in latter article, fluorescence from the $\tilde{B} \ ^2B_{3u} \ 0^0$ level is weak, a situation attributed to rapid internal conversion mediated by coupling with the $\tilde{C} \ ^2B_{2u}$ state. The current study is the first time that a high-resolution gas-phase spectrum has been reported.

1.3.2 2,4-hexadiyne cation.

One of the challenges related to astronomical observations, in particular of absorptions in diffuse interstellar clouds, is to measure in the laboratory the electronic spectra of larger and transient ions where not only the rotational but also vibrational degrees of freedom have been equilibrated to low temperatures. Once these become available, a direct comparison of the two sets of data can be made [23] with the objective of identifying the carriers. A number of such studies have proven possible in the last decade by producing cold smaller polyatomic cations in pulsed discharge sources and measuring their electronic absorption spectra with sensitive techniques such as cavity ring-down with pulsed and cw lasers [24]. The species could be identified by analysis of the rotational structure in the spectra and/or previous knowledge on the location of these electronic transitions from absorption measurements of mass-selected

species in neon matrices [2]. In the case of anions, and transient neutral species, identification of the molecules can be made by mass-selection using multi-photon dissociation processes.

The usual approaches to study the electronic spectra of cold ions in the gas phase have used molecular beams. This leads to low rotational temperatures but not all vibrational modes are relaxed. For this reason some experiments have been carried using ions cooled to liquid nitrogen temperatures for laser induced fluorescence [14] or photodissociation studies [25]. Another interesting way to improve the quality of such spectra was been using tagging methods [26], whereby a rare gas is attached to the ion parent ion. The spectra can become significantly sharper, but the rare gas causes a shift in transition energies compared to the bare ion [27].

Thus the goal of the present experiment is to relax both the rotational and vibrational motions by collisions to low temperatures as pertinent to the interstellar medium, e.g. 10-50 K. In this mass-selected ions are injected into a 22-pole radio-frequency trap where they are brought to the low temperatures by collisions with cryogenically cooled helium gas [28]. The electronic absorption is induced by tunable laser excitation and the process is detected by production of fragment ions either in one or several photon processes.

Whether the cooling has been achieved can be shown on small ions by the resolution of the rotational structure (e.g. N_2O^+ in ref. [28]) but for the larger organic ions such structure is not resolved. This has been circumvented in this study by choosing an ion with K-structure, i.e. a system with hydrogen atoms off a central carbon chain axis, which can be observed with modest laser resolution, 2,4-Hexadiyne cation is the example chosen enabling the rotational temperature to be determined. It was important to show that also such large ions are efficiently cooled in the trap and the proof is provided here.

Related approaches employing photodissociation have been carried out in the past using icr or tandem mass-spectrometers [29, 30], though cooling by collisions with helium atoms to low temperatures as 10-20 K was not implemented, and most of the experiments sampled ions with not well defined internal energy [31]. However this is a crucial aspect for the measurements

aimed at astronomical observations. In order to demonstrate the approach, a large organic cation was chosen, 2,4-hexadiyne isomer of $C_6H_6^+$, because its electronic spectrum, $\tilde{A} \ ^2E_u \leftarrow \tilde{X} \ ^2E_g$ transition, has been characterized in molecular beams in emission [32], by laser induced fluorescence [33], and the excited electronic state leads to fragmentation. Precisely, on formation of the upper state, there is competition between fluorescence to the ground state and dissociation. Both these decay channels have been studied; one by determination of the fluorescence quantum yield [34] and the other via branching ratios of fragment ions [35]. For example on production of the ion in the lowest vibrational level of the excited 2E_u state, $\sim 74\%$ of the time the ion falls back down to the ground $\tilde{X} \ ^2E_g$ state, and the rest fragments to produce dominantly $C_6H_5^+$ with minor amounts of $C_6H_4^+$ and $C_4H_4^+$. As the measured breakdown curves show, the yield of $C_6H_5^+$ and $C_4H_4^+$ remains constant (around 0.20 and 0.05, respectively) on increasing the internal energy in the 2E_u state by around 4000 cm^{-1} [34].

Because the ion is a symmetric top (with assumed D_{3h} symmetry) the K-structure (rotation around the carbon containing axis) within the $\tilde{A} \ ^2E_u \leftarrow \tilde{X} \ ^2E_g$ transition can be observed with modest resolution, enabling the temperature to be read-off from the spectrum. By this means the viability and the concept of the approach has been tested and the results are presented here. Most striking is the improvement in quality of the spectrum showing numerous narrow vibronic bands with increasing complexity as the upper states are accessed, in part due amplification of weaker bands by saturation. This new spectroscopic information on the vibrational manifold in the $\tilde{A} \ ^2E_u$ excited electronic state is presented.

1.3.3 Polyacetylene cations.

A number of polyacetylene cation chains have been studied in neon matrices [36, 37] and in the gas phase. [38-43] Interest in these species stems from the observation

of hydrocarbons in combustion and interstellar environments. [44-47] In terms of astrophysical relevance, large carbon chains are often speculated as being possible carriers of the unidentified absorptions in diffuse interstellar clouds. In this vein, spectroscopic studies in the laboratory are essential for astronomical assignments and help in the detection of new species in the interstellar medium. Approximately 100 of the more than 130 molecules that have been detected in the interstellar medium or circumstellar shells contain carbon. Because microwave spectra of the linear polyacetylene cations are not available due to their centrosymmetric nature, electronic spectroscopy offers a means of identification in the diffuse clouds.

It is crucial for a molecule to have a strong electronic transition moment in order to assist astrophysical detection. One way to search for strong optical transitions is to examine longer hydrocarbon chains for which the oscillator strength scales with size. [9] Carbon atoms have an ability to easily create covalent bonds with themselves and form larger systems, both ringed and linear. While smaller acetylene chains are apt to self-reaction, [48] larger ones are predicted to be important intermediates toward the formation of soot, and thus may display higher stability. [49, 50]

It has been suggested that the degree of ionization in interstellar clouds could be quite large. [51] The ionization potentials of the polyacetylene hydrocarbon chains have been measured up to HC_8H , and the trend shows that while diacetylene's value is 10.2 eV, that of all larger carbon chains is less than 9 eV. [52, 53] Thus there may be a large abundance of such ionized species located in the diffuse clouds.

Electronic absorption spectra obtained in 6 K neon matrices already exist for the large acetylene cation series, [36] however gas phase values are needed for direct comparison with astrophysical observations. In this paper results utilizing a technique that has been recently developed in Basel for measuring the gas phase spectrum of collisionally cooled ions using a two-colour two-photon approach are presented. [54] Ions are typically cooled to vibrational and rotational temperatures on the order of 30-80 K, mimicking conditions that are relevant

in diffuse interstellar clouds. Such low temperatures also eliminate the presence of vibrational hot bands, rendering assignments of the origin band straightforward.

While the neutral polyacetylene chains have been well documented and studied up to HC_{28}H in the gas phase, [55, 56] the cations have only been studied up to HC_{10}H^+ , with origin bands for HC_nH^+ ($n = 4,6,8$) having been rotationally resolved. Those for $n=10$ and greater will have rotational constants on the order of 0.01 cm^{-1} or less, [38] thus creating difficulties in trying to elucidate the spectroscopic structure of these larger chains.

Previous observations of the absorption spectra of the $A \ ^2\Pi - X \ ^2\Pi$ transition for HC_{12}H^+ , HC_{14}H^+ and HC_{16}H^+ in 6 K neon matrices locate the origin bands at 934.1 nm, 1047.1 nm, and 1159.8 nm respectively. [36] Typically the gas phase transitions for smaller polyacetylene cations are blue shifted by $100\text{-}130 \text{ cm}^{-1}$ with respect to the neon matrix values. [38] Taking into account such shifts places these transitions at $923.1 - 925.7 \text{ nm}$, $1033.3 - 1036.5 \text{ nm}$, and $1142.9 - 1146.8 \text{ nm}$ in the gas phase. As the number of carbon atoms increases the strong $A \ ^2\Pi - X \ ^2\Pi$ electronic transition of the polyacetylene cations shifts linearly (in nm) to the red.

1.3.4 Protonated polyacetylene cations.

Previous studies of the protonated polyacetylene cations include data from calculations, [57-60] mass spectrometry, [60-62] and matrix-isolation experiments of their electronic absorption spectra; [63] to this day the gas phase spectra have not been reported. To measure these an apparatus has been built which incorporates the cooling capabilities of a 22-pole ion trap. [28] Thus thermally cooled species can be spectroscopically interrogated.

The protonated polyacetylenes were chosen due to their chemical and astrophysical significance. Unsaturated hydrocarbons have been shown to be present in the ISM and model predictions also anticipate the presence of large polyacetylenic chains. [45, 46]

As many chemical reactions in the ISM are of the ion-molecule type, then protonated polyacetylenes stand out as important intermediates bridging the gap in the chemistry of carbon chains and cumulenes. [64]

To make significant comparisons to astrophysical observations it is necessary to create ions both rotationally and vibrationally cooled. Previous studies have employed pulsed molecular beam methods to produce cold polyatomic cations. [24, 65, 66] While these methods have proven useful in rotationally cooling the created species, spectral congestion is still present due to the fact that many of the vibrational modes are not fully relaxed. In this experiment a desired species can be collisionally relaxed by trapping the ion in a cryogenically cooled He bath. Both rotational and vibrational motions can be successfully lowered to temperatures comparable to the interstellar medium (10-80 K).

The approach used has been previously tested in a one-photon experiment in which 2,4-hexadiyne cation was cooled and photodissociated. [67] In the latter an electronic absorption was induced using tunable laser excitation and the process was monitored through the collection of fragment ions. Thus the $A\ ^2E_u \leftarrow X\ ^2E_g$ transition of $C_6H_6^+$ was observed and it was shown that rotational and vibrational temperatures of 30 K were attained. In the resulting spectrum all vibrational hot bands were suppressed due to the low temperatures that were reached through the use of cooled helium in the ion trap.

A two-photon one-colour process was utilized to study the spectrum of *p*-dichlorobenzene cation. [28] Here the ions were once again mass selected and cooled in the same helium filled ion trap, but this time two photons were required to probe the $B\ ^2B_{3u} \leftarrow X\ ^2B_{2g}$ transition of *p*-DCB⁺, as the $B\ ^2B_{3u}$ state is bound. A rich vibronic structure was observed and vibrational modes were assigned in the excited states. The photofragment spectrum itself was due to the absorption of two photons of the same colour in a process involving sequential internal conversion.

In this present study a two-photon two-colour photodissociation spectrum of a collisionally cooled trapped cation is reported. The resulting measurement is the first gas phase spectrum of a protonated polyacetylene species. Previously reported electronic absorption spectra in a 6 K neon matrix [63] pinpointed the appropriate region to scan in the gas phase. Besides locating the origin band for the three HC_nH_2^+ ($n = 4,6,8$) species, the matrix results were also able to provide useful vibrational frequencies for both the ground and excited states, which in turn led to the assignment of the C_{2v} nature of the protonated polyacetylenes.

Chapter 2 Experimental.

2.1 Apparatus.

The apparatus (Figure 2-1) consists of an electron impact ion source, a quadrupole mass filter for selecting the desired molecular ion, a cryogenically cooled RF 22-pole trap, a second quadrupole mass filter for selecting the charged photofragments, and a Daly ion detector. [68]

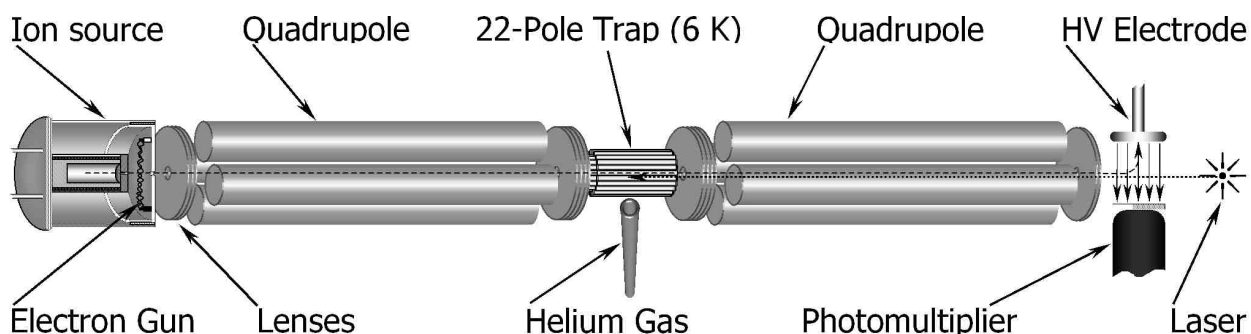


Figure 2-1 A schematic outlay of the 22-pole ion trap instrument.

All chambers are mounted on ball bushings that run along a track consisting of two (\varnothing 2.5 cm) stainless steel rods. This makes it very convenient to open the chambers for

alignment, cleaning, or replacing components. The cryostat cold head is also supported on a track that is oriented perpendicular to the main tracks, for opening up the chamber.

The system is evacuated by 5 turbo pumps. The source chamber is being pumped by one turbo pump TMU 261 (pumping speed 210 l/s) and by its own membrane pump. The chamber is separated from the rest of the system by a differential wall. This is done to protect the quadrupole mass filters from being operated at relatively high pressure (5×10^{-5} mbar) and to avoid gas condensation on the cryogenically cold 22-pole trap. The differential wall has a small orifice (\varnothing 1 mm), which restricts gas flow and subsequently lowers the pressure in the trap region by a factor of 100.

Each of the other four chambers is equipped with the same model turbo pump as the source chamber. Exhaust lines of four turbo pumps are combined using long stainless steel bellows, about 2.5 cm in diameter, which are then pumped out by a small turbo and membrane pumps. Membrane pump is used to avoid oil contamination of the system. When one breaks vacuum, the apparatus is filled with Ar gas to avoid water attachment to the inner walls and surfaces of the system. This procedure significantly shortens the subsequent pumping time.

The system is sealed by conflate (CF) flanges, with soft copper gaskets. The entire system reaches pressure as low as 1×10^{-9} mbar after 2 weeks of pumping. Pressures inside the chambers are measured using Pfeiffer Vacuum Compact Cold Cathode Gauges, type IKR261. The fore line pressures are monitored using a Pfeiffer Compact Pirani Gauge.

All electrical electrodes, ion sources, etc. are made of stainless steel, with the only exception being the 22-pole ion trap, which is made out of oxygen free high conductivity copper (OFHC copper) for good performance at low temperatures.

2.1.1 Ion source.

Figure 2-2 shows the assembled and ready-to-use ion source.

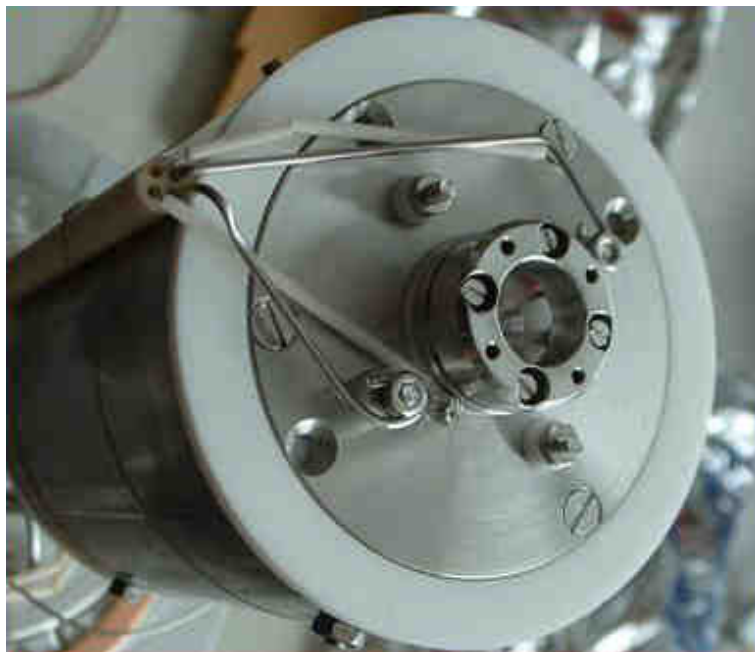


Figure 2-2 Photograph of the ion source, including the part of lens E2 that protrudes past the differential wall.

The ion source is a low-pressure electron impact source and is housed in the source chamber. It consists of an oven to vaporize the solid sample and a gas inlet, which introduces flow of the gaseous or vapors of volatile substances to an ionization region of the source.

The oven, shown in Figure 2-3, is a stainless steel fixture, about 5.5 cm in length and 2.5 cm in diameter, that is threaded on the outside.



Figure 2-3 Photograph of the oven (outer shield and ionizer have been removed).

The oven is wrapped with a heating element that has a twin core heating element. This has the major advantage that when current flows through the heating element, it actually flows through each section of the element in both directions, thus canceling out any magnetic field, generated by the electrical current. This is critical for creating a reproducible ion flux that is not disturbed by the generated magnetic field of the oven heater.

A stainless steel sleeve slips over the heating element helps to minimize heat loss and reach a maximum temperature of 1000 K. The temperature is measured by a thermocouple through a hole drilled into the stainless steel fixture.

The oven is loaded with the molecule of interest, and a cap is screwed on that has an orifice ($\varnothing 0.5$ mm). This is centered on the ionizer show in Figure 2-4. The entire assembly is then surrounded with a second stainless steel heat shield as well.

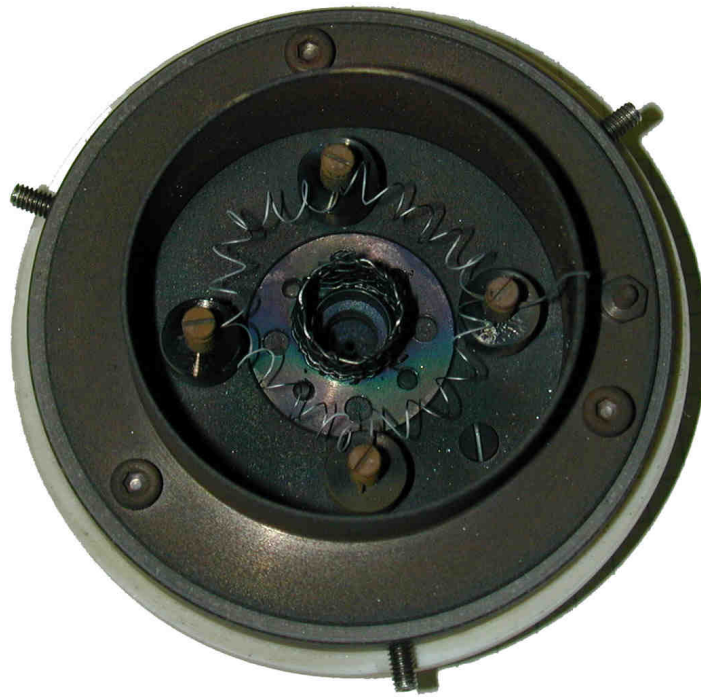


Figure 2-4 Electron Impact Ionizer.

The ionizer contains a thin Thorium doped tungsten wire (Goodfellow, 99.4 % W, 0.6 % Th, annealed, \varnothing 0.1 mm) mounted on four electrically isolated holders. Heated by 2,2 A electrical current the filament emits electrons to the center of the ionizer. The electrons are additionally accelerated by a negative potential (10 – 30 V) applied to the filament with respect to the ground. The principle electrical schematic of the ionizer is shown in Figure 2-5.

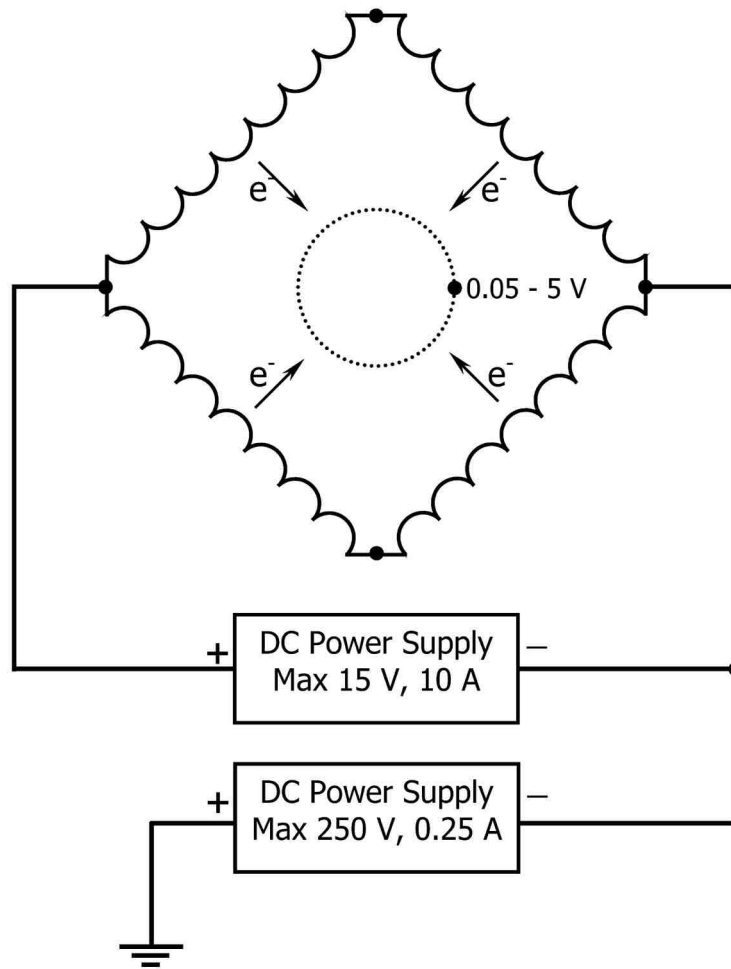


Figure 2-5 Schematic electrical connection of the ionizer.

Ions are created in a small cylindrical piece made of metal mesh (9 mm in diameter, 11 mm long). The cylindrical mesh is mounted only a few mm from the orifice of the oven. The mesh is held at a positive potential in a range of 0.05-5.0 V. This potential actually defines the potential energy of the charge particles. Ions created within the mesh can then escape through the mesh if they have more than 5.0 eV of kinetic energy. Otherwise, they will be trapped and can only escape through the extraction lenses into the first quadrupole. Ions created by an electron impact in the inner volume of the cylindrical mesh are then extracted by the electrode, which is usually at -15 V negative potential.

The entire ionizer assembly mounts onto the outer heat shield of the oven, and the last element of the assembly, an extraction lens, slides into the sleeve (Figure 2-6) of a set

of electrical lenses mounted in the next chamber. Together, these electrical lenses couple the ions produced in the source into the first quadrupole mass spectrometer.

The fixed voltages on the ion lenses are controlled by a bank of resistance dividers that can be connected to either +15 V or -15 V power supplies. The voltages are set by a 10-turn potentiometer, and can be individually monitored by connecting them to a built-in voltage monitor. The entire panel was built by Georg Holderied in the electronics shop.

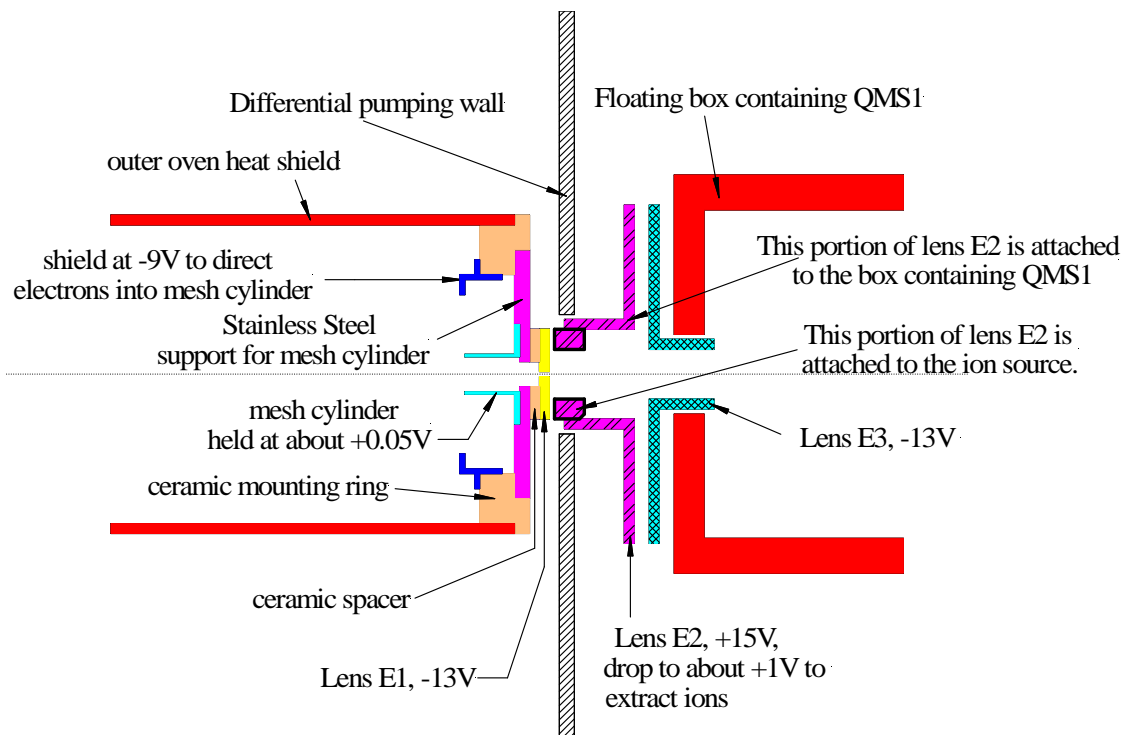


Figure 2-6 Schematic diagram of the ionizer and extraction lenses.

2.1.2 *Quadrupole mass filter.*

2.1.2.1 *Technical details.*

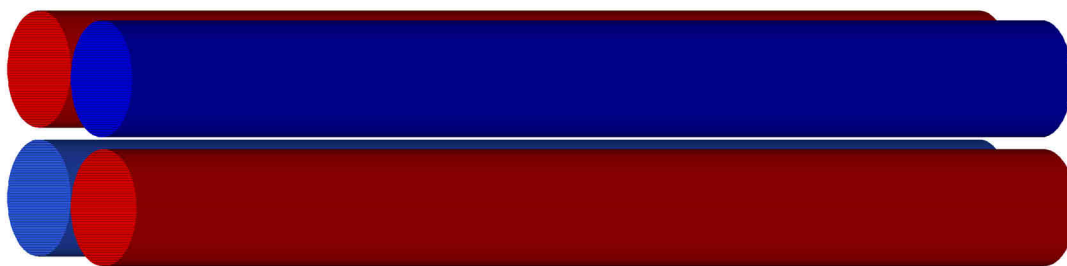


Figure 2-7 A drawing of a quadrupole. Colours indicate connected pairs of the rods.

A quadrupole is just a particular case of a multipole. It has four round rods (Figure 2-7) that are connected to two outputs of RF generator. Four mutually parallel, high mechanical precision, electrically isolated electrodes are oriented such that the electrical field between them is hyperbolic. Opposite pairs of rods are typically electrically connected, yielding a requirement for two electrical connections to the quadrupole.

While some manufacturers have chosen to fabricate high precision hyperbolic surfaced electrodes, a common way to manufacture a quadrupole is to orient four round poles such that their centers coincide with the corners of an imaginary square. The round poles are oriented such that the distance between the faces of opposite poles is nominally $1/1.148$ times the rod diameter. This ratio is chosen such that the geometry center of the quadrupole approximates an ideal hyperbolic field.

The first electric quadrupole in the apparatus is a resurrected Extrel quadrupole, built in 1995. It has a 9.5 mm diameter quadrupole assembly, with a radio frequency supply that provides 300 W of power at 880 kHz and a mass range of 3000 Daltons. The DC power supply is a model U-1272. The RF power supply is a model 150QC quadrupole power supply.

The second (analysis) quadrupole is a Nermag model with 12.5 mm quadrupole diameter, operating at 960 kHz with a mass range of 2000 Daltons.

2.1.2.2 Principle of operation.

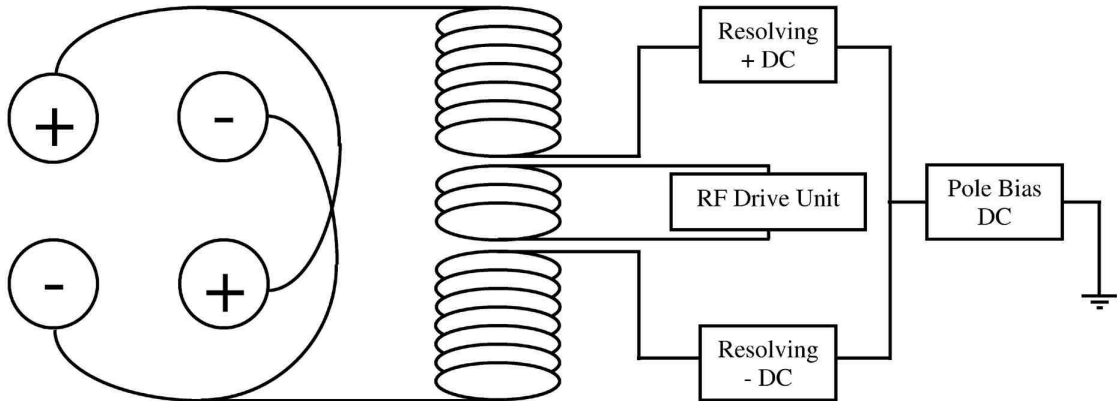


Figure 2-8 Schematic of typical quadrupole power supply connection.

Figure 2-8 shows a schematic of connection for a typical quadrupole power supply. In order to operate a quadrupole one has to provide a combination of precise DC and RF voltages to the rods. Typically a constant RF is in the range of 700 kHz to a few MHz. A high voltage RF transformer circuit has a single primary and two secondaries, which are 180 degrees out of phase with each other. There are also *resolving DC* and *pole bias offset DC* power supplies. The pole bias DC power supply determines the centerline potential of the quadrupole (i.e. same potential and polarity added to both pairs of rods). Two resolving DC supplies provide equal magnitude but opposite polarities to each pair of rods. The potentials for both of these DC supplies are biased from ground by the pole bias supply.

The motion of a particle of charge-to-mass ratio e/m in the potential field of the quadrupole can be described by the differential equations:

$$\frac{d^2x}{dt^2} + \frac{e}{m} \left[\frac{2V_{dc} - V_{ac}}{r_0^2} \cos \Omega t \right] x,$$

$$\frac{d^2y}{dt^2} - \frac{e}{m} \left[\frac{2V_{dc} - V_{ac}}{r_0^2} \cos \Omega t \right] y$$

and

$$\frac{d^2z}{dt^2} = 0,$$

where m is the mass of the ion, e is the charge of an electron, V_{ac} is the applied zero-to-peak RF voltage, V_{dc} is applied DC voltage, r_0 is the effective radius between electrodes and Ω is the applied radio frequency.

Each of the above equations is thus a special case of the Mathieu differential equation, which in its general form is usually written

$$\frac{d^2u}{d\xi^2} + (a_u - 2q_u \cos 2\xi)u = 0,$$

where $\xi = \Omega t/2$, $u = x = y$, $a_u = a_x = -a_y = 8\left(\frac{e}{m}\right)\left(\frac{V_{dc}}{r_0^2}\right)\frac{1}{\Omega^2}$, $q_u = q_x = q_y = 4\left(\frac{e}{m}\right)\left(\frac{V_{ac}}{r_0^2}\right)\frac{1}{\Omega^2}$.

The Mathieu equation is solvable in an infinite series

$$u = \Gamma \sum_{n=-\infty}^{\infty} C_{2n} \exp(2n + \beta)i\xi + \Gamma' \sum_{n=-\infty}^{\infty} C_{2n} \exp-(2n + \beta)i\xi$$

which obviously reduces to a similar infinite sum of sine and cosine functions. But for our purposes, it is acceptable to simply consider ion trajectories to be infinite sums of sine and cosine functions in x-y plane, with each successive term having smaller amplitude and higher frequency.

For a given system, the amplitude of the voltages and frequency determines which mass (or range of masses) will have stable trajectories in the x-y plane and thus pass through the quadrupole in z direction. Ions having unstable trajectories in the x-y planes will be neutralized by striking the quadrupole electrodes.

It was shown that a particle of an any mass has a stable trajectory if the values of a_u and q_u are within the region bounded by curves [69]

$$a_u = -\frac{1}{2}q_u^2 + \frac{7}{128}q_u^4 - \frac{29}{2304}q_u^6 + \frac{68687}{18874368}q_u^8 \text{ corresponding to the special case of } \beta = 0,$$

and

$$a_u = 1 - q_u - \frac{1}{8}q_u^2 + \frac{1}{64}q_u^3 - \frac{1}{1536}q_u^4 - \frac{11}{35864}q_u^5 \text{ corresponding to } \beta = 1.$$

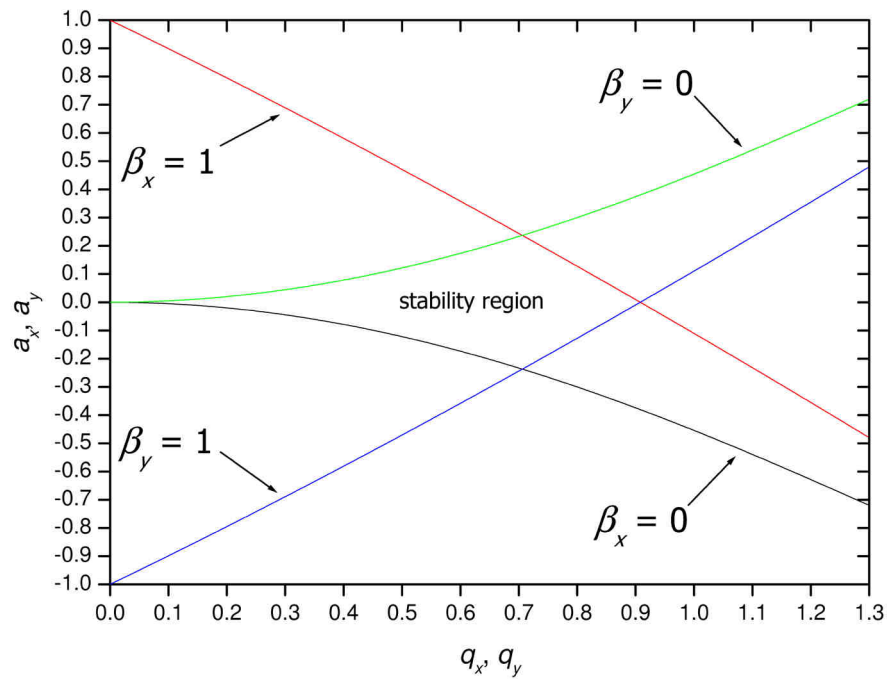


Figure 2-9 One of the stability region of Mathieu Diagram calculated based on equations from reference [69].

Figure 2-9 shows the particular stability region of Mathieu diagram in two dimensions (x and y). The stable a_x, q_x, a_y, q_y values are constrained within the solid boundary curves: black corresponding to $\beta_x = 0$, red to $\beta_x = 1$, green to $\beta_y = 0$, blue to $\beta_y = 1$.

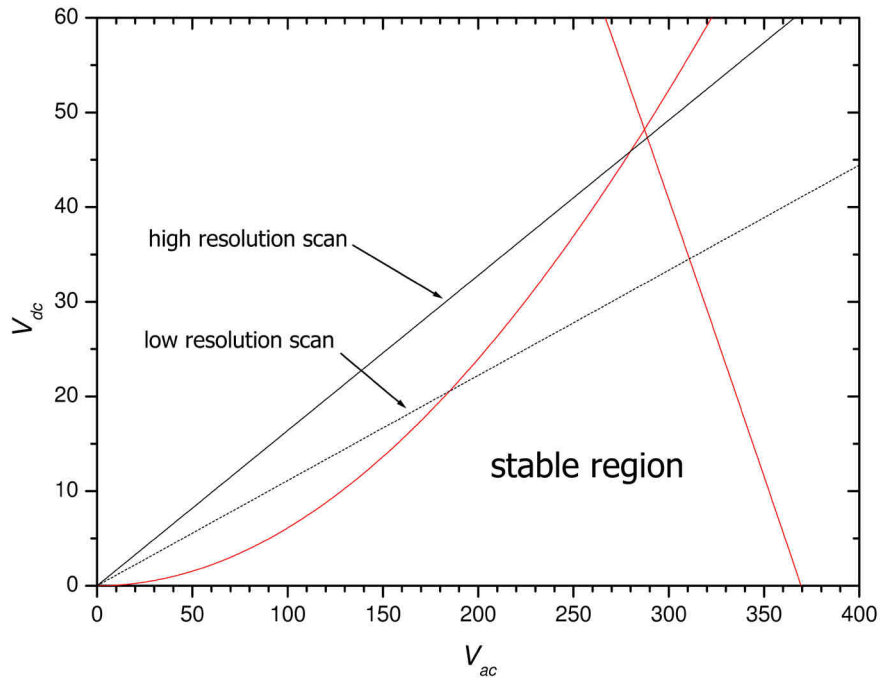


Figure 2-10 Expanded view of stability region of Mathieu diagram with suitable substitutions for a and q to convert into RF and DC space for mass 300 and 9.5 mm quadrupole operated at 880 kHz.

Figure 2-10 is an expanded view of the stability region of Figure 2-9, with suitable substitution for the Mathieu parameters a_x , q_x , a_y , q_y to convert the axes into RF-DC voltage

space for m/z 300, with $r_0 = \frac{d_{rod}}{2 \times 1.148}$ calculated based on a 9.5 mm round Extrel quadrupole

rod diameter, and operating frequency $f = \frac{\Omega}{2\pi} = 880 \text{ kHz}$. For any set of RF and DC voltages,

one could read directly from this figure whether ions of m/z 300 would have stable trajectories through a 9.5 mm quadrupole operated at 880 kHz. It is evident from the figure that when no DC voltage is applied to the rods, the quadrupole will be operating in an integral (ion guide) mode.

Straight (solid and dashed) lines show simultaneous change of DC and RF voltages upon a mass scan. The dashed line is a low resolution scan and solid one is a high resolution. Mass resolution can be increased by simply raising the slope of the scan line and lowering its intercept with the triangle (stability region).

2.1.3 22-pole radio frequency ion trap.

Multipoles are widely used in many different applications. In general a multipole can be driven as an ion guide or trap. To guide ions a certain amplitude of radio frequency is usually applied to a multipole. By adding a small DC float voltage to the RF amplitude one can either accelerate or decelerate ions. A multipole of a special configuration can be used for more challenging purposes, for instance, focusing a charged particle beams to a relatively small sizes [70].

In order to trap ions additional two electrodes in the entrance and in the end of a multipole are required. By applying DC potential to these two electrodes one can accumulate, store ions in principle infinitely. Once ions are trapped inside of a multipole one can do many of different studies, e.g. chemical reactions [71], collisional relaxation and dissociation of cluster ions [72], or resonant photofragmentation spectroscopy [28] and etc.

2.1.3.1 Technical details.

The 22-pole trap (Figure 2-11), which follows the design of Gerlich, [71, 73] consists of 22 stainless steel rods (1 mm diameter, 36 mm length) equally spaced on an inscribed radius of 10 mm.

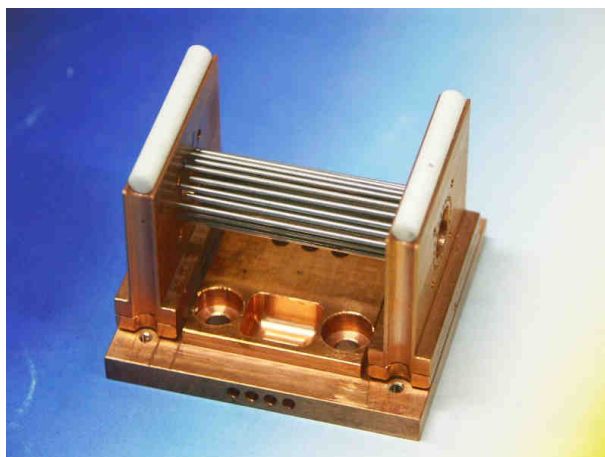


Figure 2-11 22-pole RF Ion Trap.

The described geometry derives from the already established [74] important equation:

$$R = \frac{r_0}{n-1},$$

where R : rod radius; r_0 : inner radius of the rod arrangement or the so-called trap radius and $2n$: the number of rods.

The 22-pole trap is made almost entirely out of oxygen-free high conductivity copper. Two flat pieces of copper on sides have arrays of 11 holes drilled into them. Rods were finally press-fitted into them. The rods were cooled to low temperature and at the same time the copper was heated up. Straight after the rods were quickly inserted into the copper pieces, so that when the copper cools, they are rigidly held in place all the time.

In the Figure 2-11, it is clearly seen that the rods are only supported on one end (look at the left end of the rod assembly, and you will see that half of the rods do not extend far enough to touch the copper plate). This was done especially to avoid electrical contacts between two sets of rods on opposite copper holders.

Moreover copper holders are electrically insulated from the copper trap housing by thin sapphire (Al_2O_3) plates, which have no electrical conductance but have a relatively high heat transmission. Indium foil was placed between the sapphire and copper edges to provide optimal thermal contact. Being very soft, indium leaks into all surface imperfections providing the best heat conductance.

The rod assembly is enclosed by a Π -shaped copper cover. The cover is screwed down onto the trap housing to enclose the box and prevent gas from escaping quickly. It is electrically isolated from the oscillating voltage of the endplates by the long cylindrical ceramic insulators that fit into the hemi-cylindrical grooves. Two are shown in Figure 2-11 on top of the copper endplates. Two additional ones go in the two grooves in the front of the trap, as seen in the figure, and two more go in an analogous pair of grooves on back of the trap.

These last four cylindrical ceramic insulators have a hole bored through them through which a screw passes to hold the top of the box onto the whole system.

The copper box that contains the 22-pole trap is mounted on the second stage of helium cryostat and is additionally surrounded by a heat shield of highly polished aluminum that is bolted to the first stage of the cryostat. This shield is closed on all sides in order to avoid radiative heat transfer from the room temperature surroundings.

Leybold COOLPOWER 5/100 cold head is used as a cryostat, which can provide 6 W of cooling power at 20K, 100W at 80K. The cold head is powered by the Leybold COOLPAK 6000 compressor unit. A thin foil of indium conducts heat between the trap housing and the cold head. Electrical connection wires and the helium buffer gas line are precooled on the first stage of the cryostat to a temperature of 80 K before attachment to the trap. To measure the temperature of the trap a calibrated silicon diode is mounted in the base of the 22-pole trap housing. The lowest temperature achieved is slightly above 5 K.

It is imperative that no electrical connections that are subject to the low temperatures of the trap are made with solder. Under low temperatures and repeated temperature cycling, solder undergoes a phase change and becomes quite brittle, resulting in flaking and unreliable connections under these conditions. Furthermore the ion trap moves by about 3 mm when cooled down to 5 K due to thermal contraction of the cold head. Thus, the cold head has to be on a translatable mount so that it can be aligned when cold. A Linos telescope with cross hairs was used for proper alignment. The objective is a 1.2× magnifier and the two eyepieces are f 25×, 10×. All electrical lenses, quadrupoles, etc. have the ability to mount crosshairs on them (including the 22-pole device), and the telescope can be used to align these objects.

2.1.3.2 Principle of operation.

The rods are alternately connected to the two outputs of the RF generator which is built according to the principles described in [75]. The trap operating frequency was in the range of 1.5 - 2 MHz while the RF peak-to-peak amplitude was in the range of 40-100 V. In addition to the oscillating voltage the system is floated to a potential of +0.4 V, so that the sine waves are not centered at 0 V (Figure 2-12).

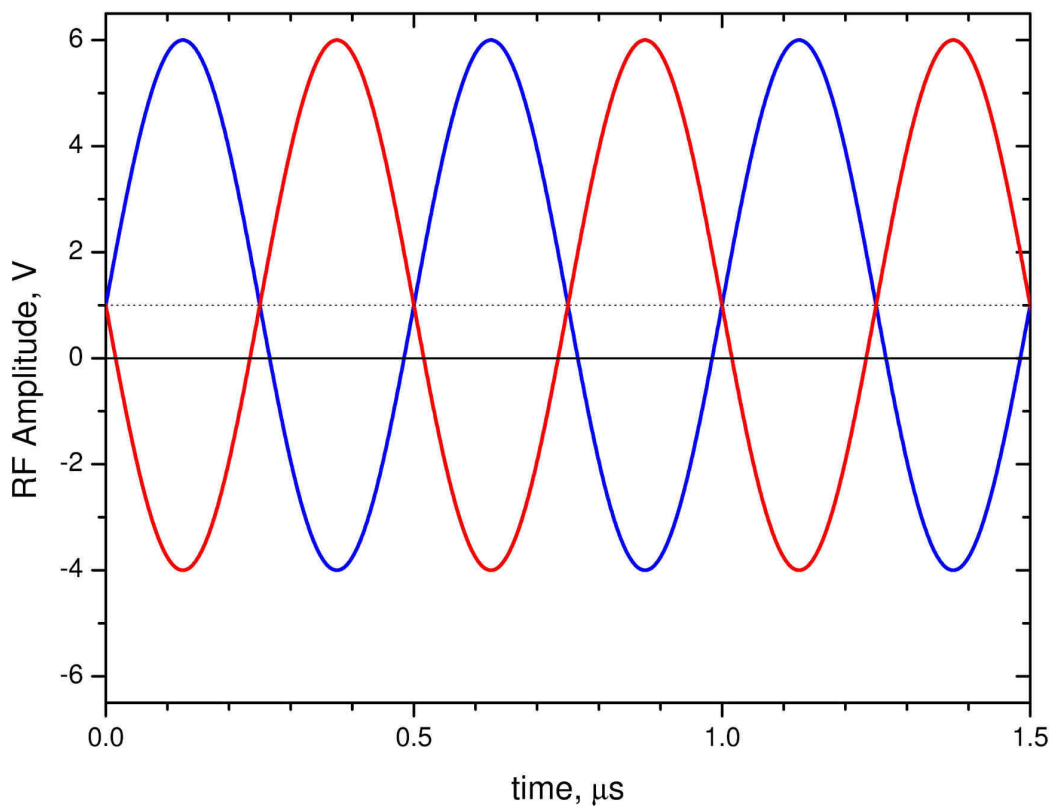


Figure 2-12 RF applied to opposite sets of rods of the 22-pole trap. The RF amplitude, as well as the floating voltage values in the figure, are taken just as an example.

With these parameters the 22-pole trap has a confining potential of approximate cylindrical symmetry, and rising steeply near the periphery (with an R^{20} dependence, Figure 2-13) leading to a large field free volume where the ions are largely unaffected by RF heating and can be effectively thermalized by helium buffer gas cooling.

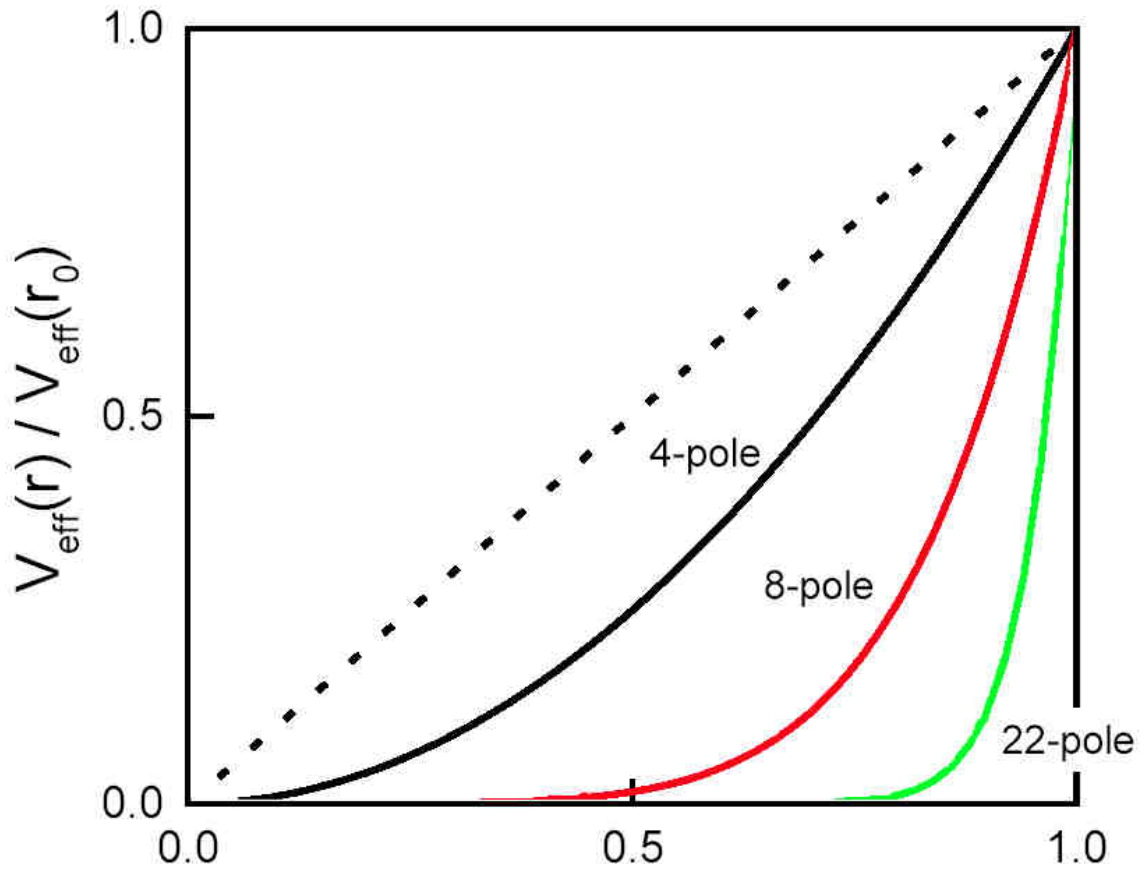


Figure 2-13 Cross-section of the effective potential surface for a quadrupole, octopole and 22-pole.

The base plate of 22-pole trap has three holes in it, just barely visible in the Figure 2-11, which allow a stream of gas to enter. The actual gas inlets are on the opposite side of the base plate, so that gas has to flow through the cold base plate before entering into the trap.

Helium is leaked into the trap using a continuous leak valve from Leybold. The pressure in the trap was estimated as 5×10^{-4} mbar corresponding to a helium number density of $4 \times 10^{14} \text{ cm}^{-3}$ at 10 K. Because the gauge (pressure meter) is mounted outside the trap there is no direct pressure measurement. It is thought that the pressure inside the trap is actually about a factor of 5× higher. The pressure gauge calibrated for N_2 reads $1.5\text{-}2.5 \times 10^{-5}$ mbar. For He the pressure is about a factor of 6× higher ($\approx 10^{-4}$ mbar).

Assuming a Langevin rate coefficient of $\approx 10^{-9} \text{ cm}^3 \text{ s}^{-1}$, bimolecular thermalising collisions occur at a frequency of $\approx 4 \times 10^5 \text{ s}^{-1}$. Therefore the ion temperature is expected to approach

the ambient trap temperature in a few milliseconds. Ions are left to cool inside the trap for 70 ms prior to firing the probe laser(s).

A potential of about 1.3 V was applied on the trap entrance lens and of about 1.9 V on the exit side. The trap itself was floated at 0.4 V with respect to the ground. The idea is to impinge the ions onto the trap with kinetic energies between 1.3 and 1.9 V, then use helium collisions to cool them so they are trapped below the 1.3 V entrance potential. All these potentials can be slightly different for a variety of ions. The small differences here come from the fact that the production and trapping conditions for different ions require different electron energies for electron impact, and slightly different extraction and trapping potentials.

2.1.4 *Daly detector.*

Ion detectors are widely used for many applications, as well as for mass spectrometry. The simplest ion detector is a Faraday cup. It is a metal cup that is usually placed in the path of the ion beam. It is attached to an electrometer which measures the ion-beam current. A Faraday cup is capable of measuring both cation- and anion-beam currents. Because a Faraday cup can only be used in an analog mode it is less sensitive than other detectors that are capable of operating in a pulse-counting mode.

A channeltron is an ion detector which can be operated in pulse counting mode and consequently is more sensitive. It has a horn-shaped continuous dynode structure that is coated on the inside with an electron emissive material. By applying a high potential to the dynode one creates continuous potential distribution along the channeltron. The high negative potential at the entrance continuously decreases till the channeltron end. An ion striking the channeltron creates secondary electrons that have an avalanche effect to create more secondary electrons and finally a current pulse.

The principle similar to channeltron is used in microchannel plate (MCP) detectors. A MCP consists of an array of glass capillaries (10-25 μm inner diameter) that are coated on the inside with a electron-emissive material. The capillaries are biased at a high voltage, and like the channeltron, an ion that strikes the inside wall one of the capillaries creates an avalanche of secondary electrons. This cascading effect creates a gain of 10^3 to 10^4 and produces a current pulse at the output.

All the detectors briefly mentioned above are usually placed in the path of the ion beam. To circumvent such difficulty one may use a Daly detector. This type of an ion detector was introduced by N.R. Daly in 1960 [68]. A Daly detector (Figure 2-14) consists of a conversion dynode, scintillator (BC400 plastic scintillator, 0.5 mm thick, from GC Technology GmbH, Freidling 12 D-84172 Buch am Erlbach.) and photomultiplier tube (R647 Hamamatsu PMT).

A critical feature of the scintillator is that it has been coated with a thin aluminum coating (slightly transparent), so that the burst of electrons coming from the dynode must pass through this aluminum coating prior to exciting the phosphor. This has two advantages. First, the highly reflective aluminum coating greatly reduces the intensity of scattered laser light that hits the detector, thereby reducing the background signal. Second, photons emitted from the phosphor that are going in the wrong direction are reflected back to the PMT tube, so that they are detected. The scintillator was custom-coated with aluminum for the J.P. Maier group by the Department of Materials Science and Metallurgy, New Museums Site, Pembroke Street, Cambridge CB23QZ, UK. The scintillator has a short pulse output, roughly 10 ns.

The dynode is a high polished metal knob at a negative high potential in a range of 20-30 kV, which emits secondary electrons when ions impinge on the surface. The secondary electrons are accelerated onto the scintillator, providing light which is then detected by the PMT. The output of the PMT is sent to a discriminator (Phillips Scientific Model 6904, 300 MHz), which has a variety of outputs. In any event, every pulse that crosses the threshold (-20 mV)

leads to the production of an output pulse (5V, 5 ns width). This is then sent to an HP5316A universal counter. The counter has a gate input, and only counts pulses received during the gate. The number of counts is displayed on a front panel as a digital value, and is also sent to the computer using a GPIB interface.

The position of the dynode is found initially by moving it backwards and forwards along the supporting rod until the electron image of the ion beam, which is formed at the scintillator, is in the middle of the latter.

The dynode and PMT are surrounded by a cylindrical grounded shield with two holes which allow both the ion and laser beams to pass through. This is critical so that the high electrical field of the Daly detector does not penetrate into the second quadrupole. This grounded shield should be highly polished and have rounded corners so that the 30 kV does not discharge to it.

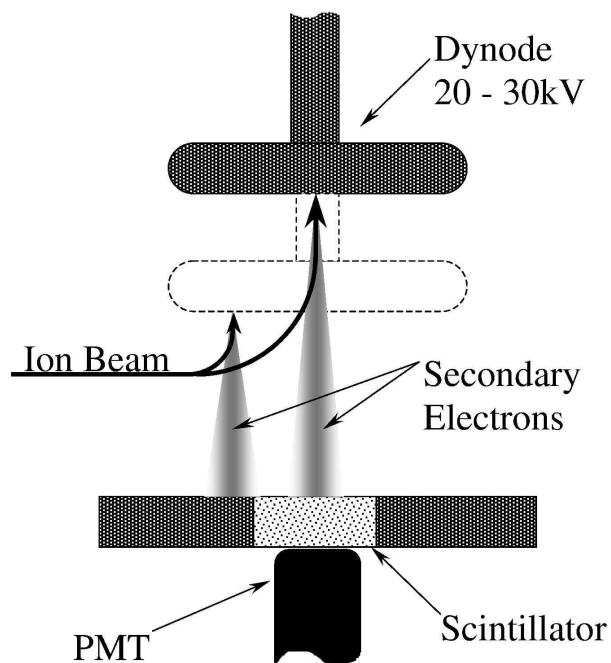


Figure 2-14 The principle scheme for the Daly detector and dynode position adjustment.

The Daly detector is an ion counting counter. It operates between $0.1-2 \times 10^6$ counts per second. The large first dynode potential provides 6 electrons per ion impact and hence the high gain of a Daly detector is about 10^7 . The detector has a low noise level, 4×10^{-20} amp, and the discrimination is small for ions in the high and low mass range. Admission of a gas to the vacuum system does not affect the gain of the detector, as no activated surfaces are situated within the vacuum.

Another advantage of the Daly detector is that the PMT and other electronics are external to the vacuum. In the event of a fault occurring in the PMT a new one can be substituted in a few minutes without letting air into the vacuum chamber. The Daly detector does not occupy the main axis of the apparatus and thus allows one to introduce a laser beam into it.

2.2 Laser optical scheme.

2.2.1 One-colour experiment.

In the present studies electronic absorption spectra of molecular ions are recorded via detection of fragments. If the excited electronic state of interest undergoes predissociation, this is a one-photon experiment. In other words, if the one-photon resonant absorption brings molecular ions above the fragmentation threshold the process is considered to be a one-photon (colour) experiment. Figure 2-15 shows an example, where the first electronically excited state of 2,4-hexadiyne cation undergoes predissociation.

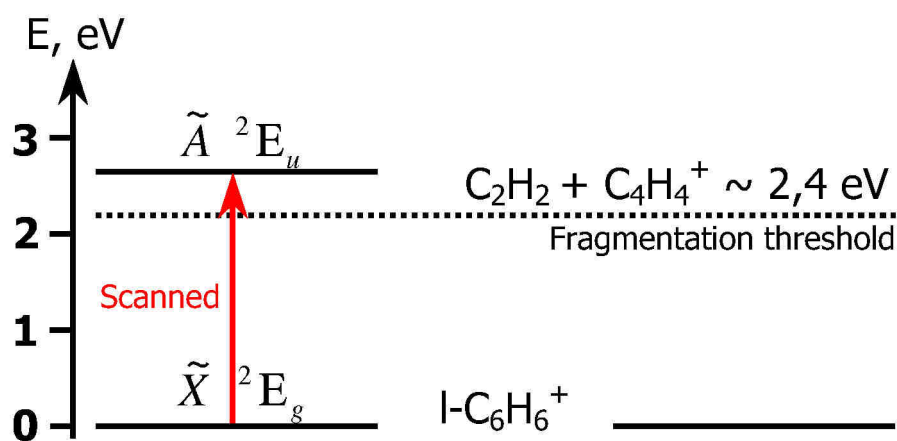


Figure 2-15 Energy diagram for 2,4-hexadiyne cation.

2,4-hexadiyne cation (linear isomer of $C_6H_6^+$) has its first electronically excited state slightly above the fragmentation threshold. After absorption of one resonant photon 2,4-hexadiyne cation dissociates to $C_4H_4^+$ and C_2H_2 . Recording the number of former cations as a function of the laser wavelength gives an electronic absorption spectrum of 2,4-hexadiyne cation. Figure 2-16 demonstrates the laser arrangement for a one-colour experiment.

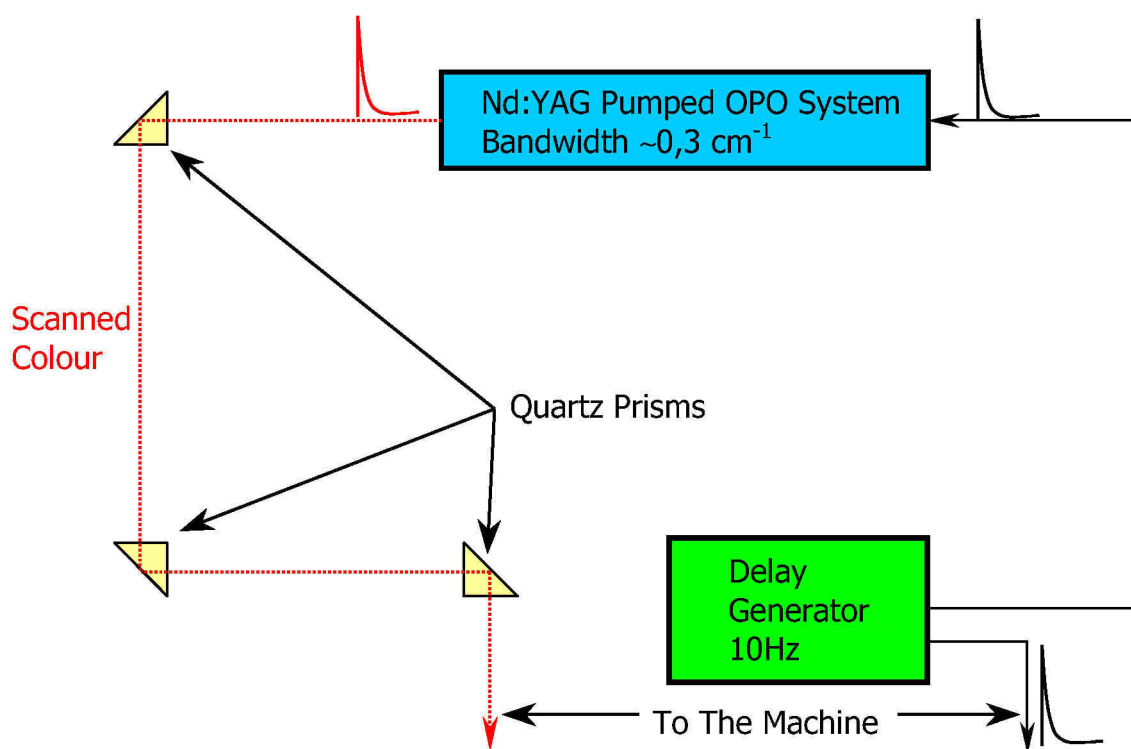


Figure 2-16 Laser arrangement for an one-colour experiment.

A narrow band (0.3 cm^{-1}) Nd:YAG pumped OPO system is externally triggered from a BNC pulse generator. The external triggering is required in order to fire the laser exactly when the ions are present in the trap. A pulse (width of $65 \mu\text{s}$) from one channel of the pulse generator is sent to the laser. Another channel of the pulse generator is sent to the external trigger input of the apparatus. By adjusting the delay between these two channels one can fire the laser at the required time.

The laser pulse is delivered to the 22-pole trap of the apparatus by three rectangular quartz prisms. The laser beam is preliminary aligned through two diaphragms. These are separated by approximately 2 meters and placed in front of a viewing port of the apparatus. Fine laser beam adjustment is usually achieved by maximizing the yield of fragment ions.

2.2.2 Two-colour experiment.

A multi-photon approach is usually required if the lowest and some of the superposed excited electronic states do not undergo predissociation. In other words, if the energy of the one resonant photon is not enough to bring a molecular ion above the fragmentation threshold. In this case an additional absorption of a second photon can make it possible.

A process in which two photons of different energies are absorbed is considered to be a two-colour experiment. Figure 2-17 shows an example of this, where the first electronically excited state of C_6H_2^+ (triacetylene cation) does not predissociate.

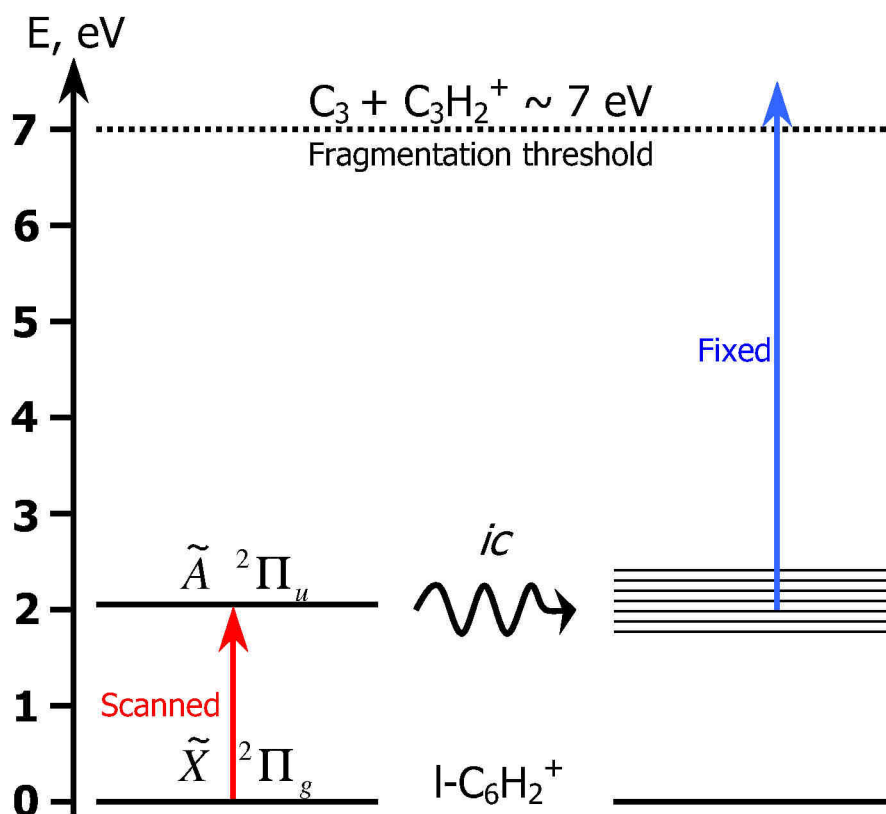


Figure 2-17 Energy diagram for triacetylene cation.

As can be seen from the figure, triacetylene cation has its first electronically excited state below the fragmentation threshold. Only the absorption of a second, more energetic, photon (of about 5eV) can dissociate triacetylene cation into $C_3H_2^+$ and C_3 neutral. Recording the number of former fragments as a function of the laser wavelength gives an electronic absorption spectrum of triacetylene cation. In Figure 2-18 the laser arrangement for a two-colour experiment is shown.

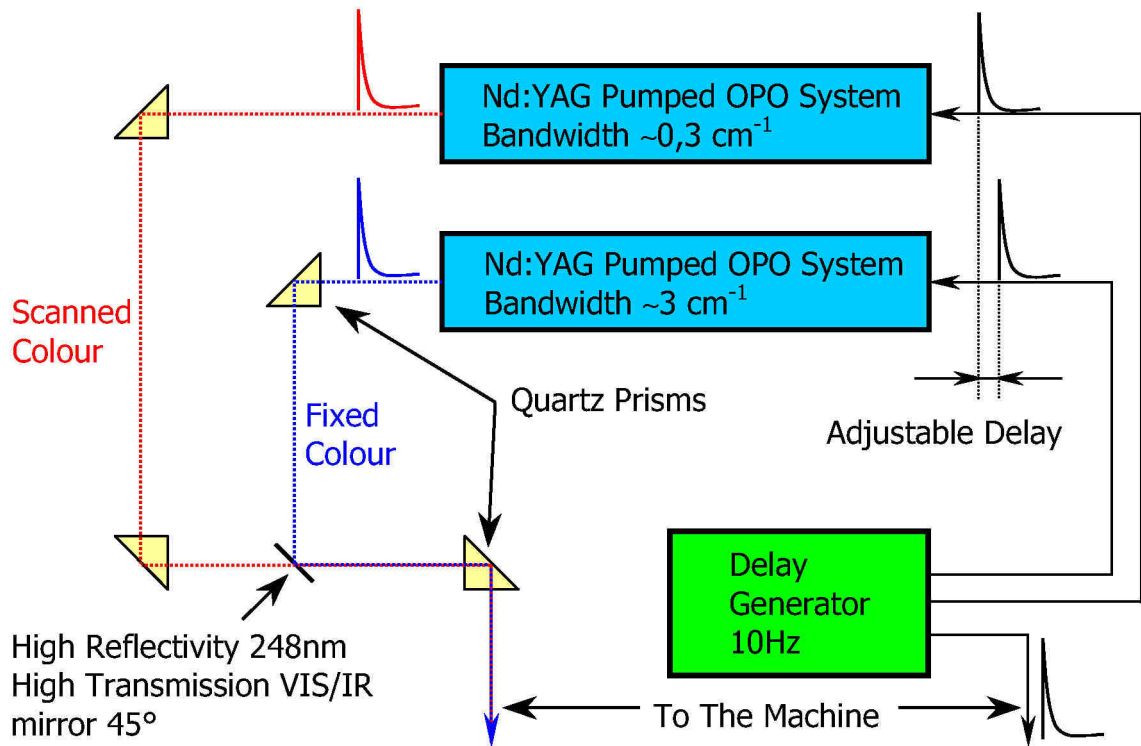


Figure 2-18 Laser arrangement for a two-colour experiment.

As one can see from the figure there are two lasers. One is a narrow band (0.3 cm^{-1}) Nd:YAG pumped OPO and the second is a broad band (3 cm^{-1}) Nd:YAG pumped OPO system. The former laser system is used to provide tunable radiation while the other one delivers the fixed wavelength. The second colour is typically in the range of 210 - 355 nm (5.9 - 3.5 eV). The two laser systems are externally triggered from a BNC pulse generator. The external triggering is required in order to fire the lasers exactly at the same time, and moreover at a time when the trapped ions are present in the 22-pole trap. Pulses (width of $65 \mu\text{s}$) from two independent channels of the pulse generator are sent to the lasers with the delay determining the relation to one another. This is necessary due to the lasers having different response times. To circumvent this difficulty one has to adjust the delay between the two trigger pulses so that the laser shots overlap in time. The third channel of the pulse generator is sent to the external trigger input of the apparatus. By adjusting the delay on this channel one can fire the laser at the required time.

The laser pulses are delivered to the 22-pole trap by a set of rectangular quartz prisms and mirror. The mirror has an usually high reflectivity for the second fixed colour and transmission for the first tunable radiation. Geometrical overlap of the two laser beams is controlled by using two diaphragms. These are separated by approximately 2 meters and placed in front of the viewing port of the apparatus. Fine alignment is usually done by maximizing the yield of fragment ions. Optimal alignment involves obtaining the maximum yield of fragments from two colours and minimum from either the first or second colour separately.

2.3 Software and data acquisition cards.

The experiment is run under software based on the Labview 7.0 platform. There are three main programs used for the experiment. The first *ABB Extrel Mass Spectrometer* is used to record the mass spectra of species produced and to filter a desired mass from all fragments. The second program, named *Nermag Mass Spectrometer*, helps to analyze the particles collected in the 22-pole trap and produced after laser exposure. The last program, named *Sunlight EX OPO Laser Spectrometer*, records the electronic absorption spectra of the trapped particles. The last program is specific to the Sunlight OPO System and cannot be used for any of the other lasers. For instance, in order to control another laser system, (e.g. ScanMate dye laser or Ekspla OPO system) one has to run a proper program.

2.3.1 ABB Extrel mass spectrometer.

The front panel (user interface) of the LabView program for ABB Extrel Mass Spectrometer is shown in Figure 2-19.

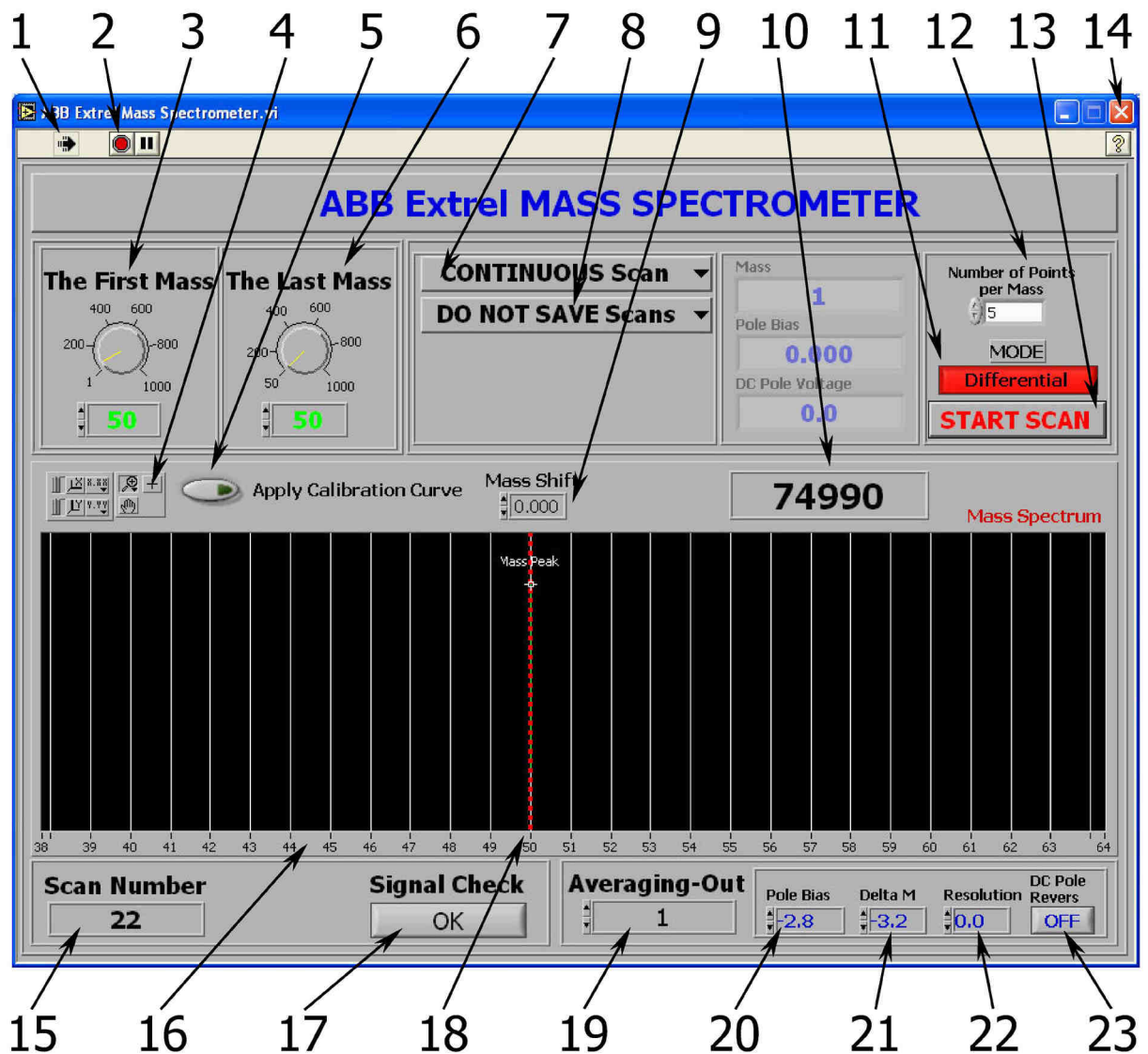


Figure 2-19 Labview program for the ABB Extrel quadrupole mass spectrometer (user interface).

In order to start program press button 1 on the left top corner of the program window. Button 2 stops the program at any time. Next step is to set the beginning and the end of the mass scan with the *first mass* (3) and *last mass* (6) dial knobs. The exact mass value can be seen on the digital display below each of the dial knobs. If the values of the *first* and *last masses* are identical then the quadrupole will transmit only one specific mass.

The mass scan can be done in a few different ways. The drop-down dialog button 7 offers three different options. One of the options is a *single scan*: after one successful mass scan the program will stop and wait until the *start scan* button (13) is pressed again. This option

is often used to occasionally check the mass spectrum's resolution. The second option is *finite scan*, which performs a multiple scans, defined by the user. This option can be used to record and average a few mass spectra. The actual scan number can be directly read out from *scan number* display (15). The last scan option makes continuous infinite scans. To set this, *continuous scan* has to be chosen. The last mode is best for fine resolution adjustment.

High resolution on the ABB Extrel mass spectrometer can be set through simultaneous adjustment of digital controls 20, 21, 22. *Pole bias* (20) defines the quadrupole DC offset in Volts and so kinetic energy of transmitted ions. *Delta M* (21) serves as a coarse adjustment of the quadrupole resolution. Fine resolution adjustment can be done by *Resolution* (22) digital control. If high resolution is still not achieved one can try to swap the DC and RF voltages on the quadrupole rods. Usually two pairs of quadrupole rods must be identical, but due to mechanical precision one can find better ion transmission by pressing the *DC Pole Reverse* button (23). When necessary the resolution (resolving DC voltages) can be turned off by pressing the 11 button which switches between *Differential* and *Integral* modes.

With the drop-down dialog button 8 one can choose whether the scan will be saved as a txt file or just displayed on the screen as a mass spectrum. Control 12 defines the scan step-size. If number of point per mass is set to 5 then the step-size will be $1/5 = 0.2$ Dalton. The number of ions at each point of the scan can be read out from digital display 10.

While a mass spectrum is recorded, scale (zoom-in or -out) can be adjusted by instruments (4). The changes are directly seen on the screen (16), where the dotted red line (18) indicates the current mass while scanning. In addition digital control *mass shift* (9) can correct the mass spectrum if the maximum of the mass peak is ± 0.5 Dalton away from the real mass. In order to have the right mass peak position over the whole range a calibration procedure must be initially performed. The calibration curve can be internally stored once and can later be applied by pressing button 5.

If the recorded spectra are noisy one can set up automatic averaging by digital control 19. In this mode recording the whole spectrum will take longer but will result in a better signal-to-noise ratio. The program window can be closed by button 14 but all set parameters will still be applied to the quadrupole.

By pressing the *signal check* button (17) the actual number of ions can be seen on big display (Figure 2-20). A few details about the *Signal check window* are presented further.

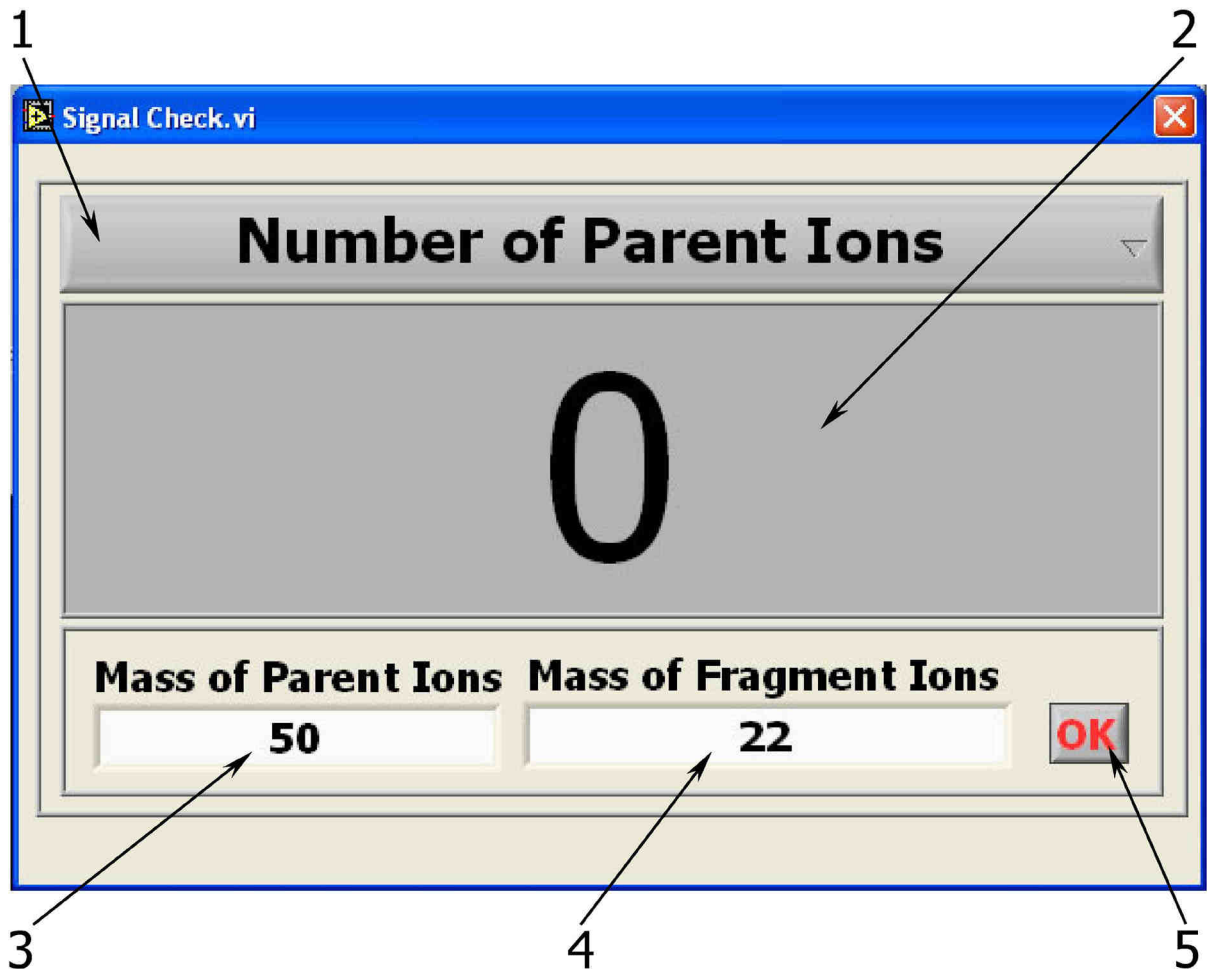


Figure 2-20 Signal check pop-up window.

The ion signal check window will automatically pop-up and will remain opened on the screen until the *ok* button (5) is pressed. This feature is useful when one performs the ion current optimization. The digits on the big display (2) can be easily seen from a distance. By initially setting two different desire masses in digital controls 3 and 4 one can check both masses by choosing the desired mass from drop-down dialog box 1.

2.3.2 Nermag mass spectrometer.

Front panel (user interface) of LabView program for Nermag Mass Spectrometer is shown on Figure 2-21.

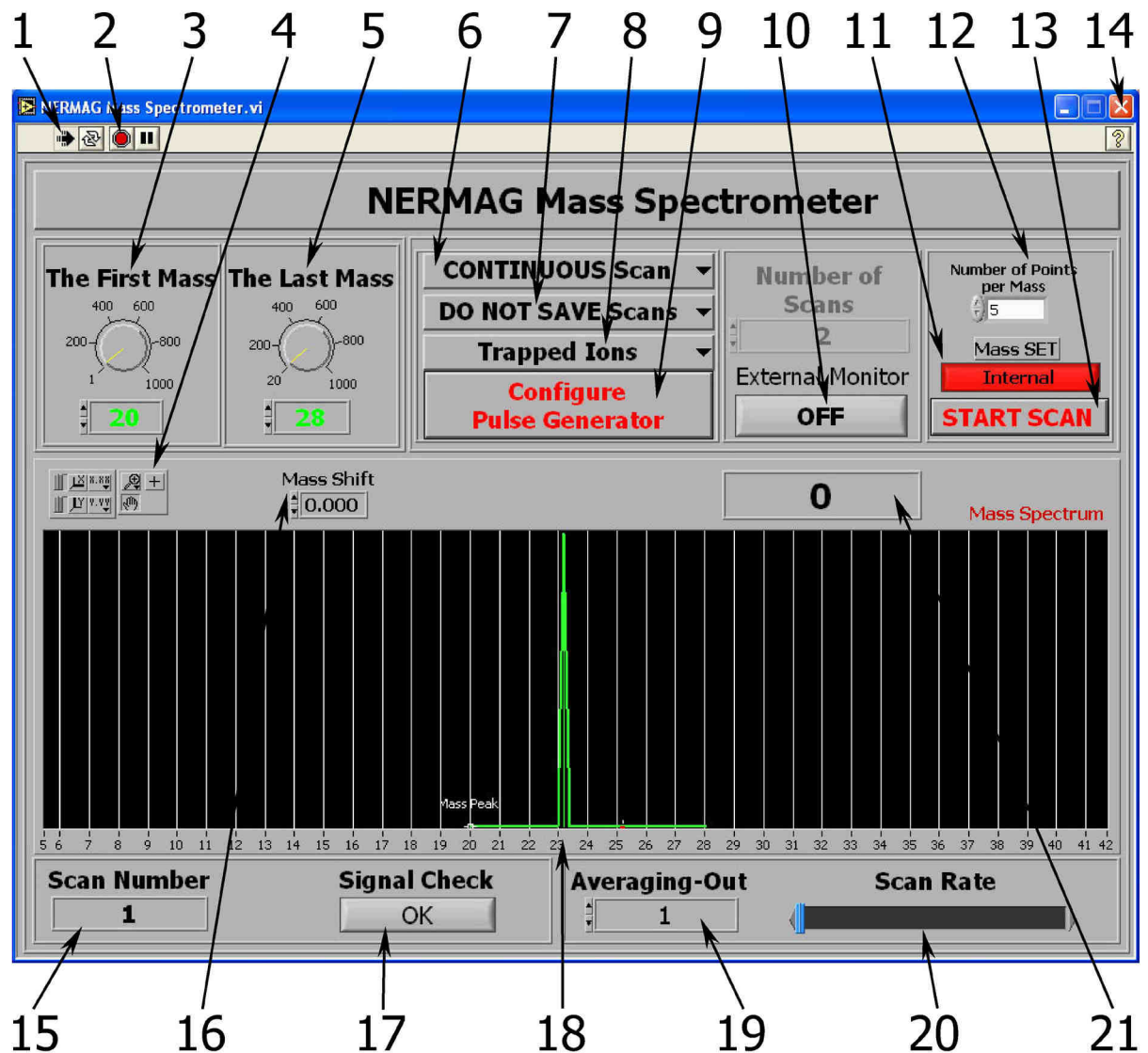


Figure 2-21 LabView program for Nermag quadrupole mass spectrometer (user interface).

In order to start the program press button 1 on the left top corner of the program window. Button 2 stops the running program 2 at any time. To set the beginning and end of the mass scan one has to adjust the desired values by the *first mass* (3) and *last mass* (5) dial knobs. The exact mass values can be seen on the digital displays below each of the dial knobs. If the values of the *first* and *last masses* are identical the quadrupole will transmit only one specific mass.

The mass scan can be done in different ways. The drop-down dialog button 6 offers three different options. One of the options is a *single scan*: after one successful mass scan the program will stop and wait until the *start scan* button (13) is pressed again. This option is often used to check the mass spectral resolution. The second option is *finite scan*, which performs multiple scans, with the number of scans defined by user in addition. This option can be used to record a few mass spectra and later average them. The actual number of scans can be read directly from the *scan number* display (15). The last option makes an infinite number of scans, using the *continuous scan* option. The last mode is best for fine resolution adjustment. Resolution on the Nermag mass spectrometer can only be adjusted manually on the quadrupole control unit.

With the drop-down dialog button 7 one can choose whether the mass spectrum will be saved as a txt file or displayed on the screen. The experimental approach can be changed by drop-down dialog button 8. This dialog button offers either to run the experiment in continuous or pulsed mode, which is required for spectroscopy on trapped ions. Continuous mode can only be used for initial adjustment in order to make sure that ions can be efficiently guided through the whole apparatus. Once ions are successfully guided, *trapped ions* mode must be chosen to further adjust the various parameters and run spectroscopic measurements.

The control 12 defines the scan step-size. If the number of points per mass is set to 5 then the step-size will be $1/5 = 0.2$ Dalton. The number of ions at each point of the scan can be read out from digital display 21. While a mass spectrum is recorded, the scale can be adjusted by the set of instruments (4) and the changes can directly be seen on the screen (18), where the dotted red line indicates the current mass while scanning. In addition, uncertainty in the mass calibration (± 0.5 Dalton) can be corrected by using the adjusted *mass shift* control (16). A calibration procedure must be initially performed in order to have the right mass peak position over the whole range of masses. The calibration curve can be internally stored and always applied to a present mass scan.

If the recorded spectra are noisy one can set up averaging by digital control 19. Recording the whole spectrum will take longer, but will result in a better signal-to-noise ratio. The scan rate can be changed through *scan rate* slider (20). By pressing the *signal check* button (17), the number of ions can be seen on the big display (Figure 2-20). The features of the *signal check* window have been previously described.

In order to be able to monitor the ion signal away from the computer on an external monitor one can apply the *external monitor* button (10). The mass can either be set from the program or manually from quadrupole control unit. By pressing button 11 one can easily switch between the two modes. The internal mode is highly recommended! The program window can be closed by button 14, but all set parameters will still be applied to the quadrupole. This button functions like an emergency stop. Note that after this procedure all unsaved data will be lost! In order to set the desired pulse sequence on the internal (software) pulse generator the *configure pulse generator* button (9) must be pressed. The following window (Figure 2-22) will pop-up and remain opened unless the *configure* button (7) is pressed.

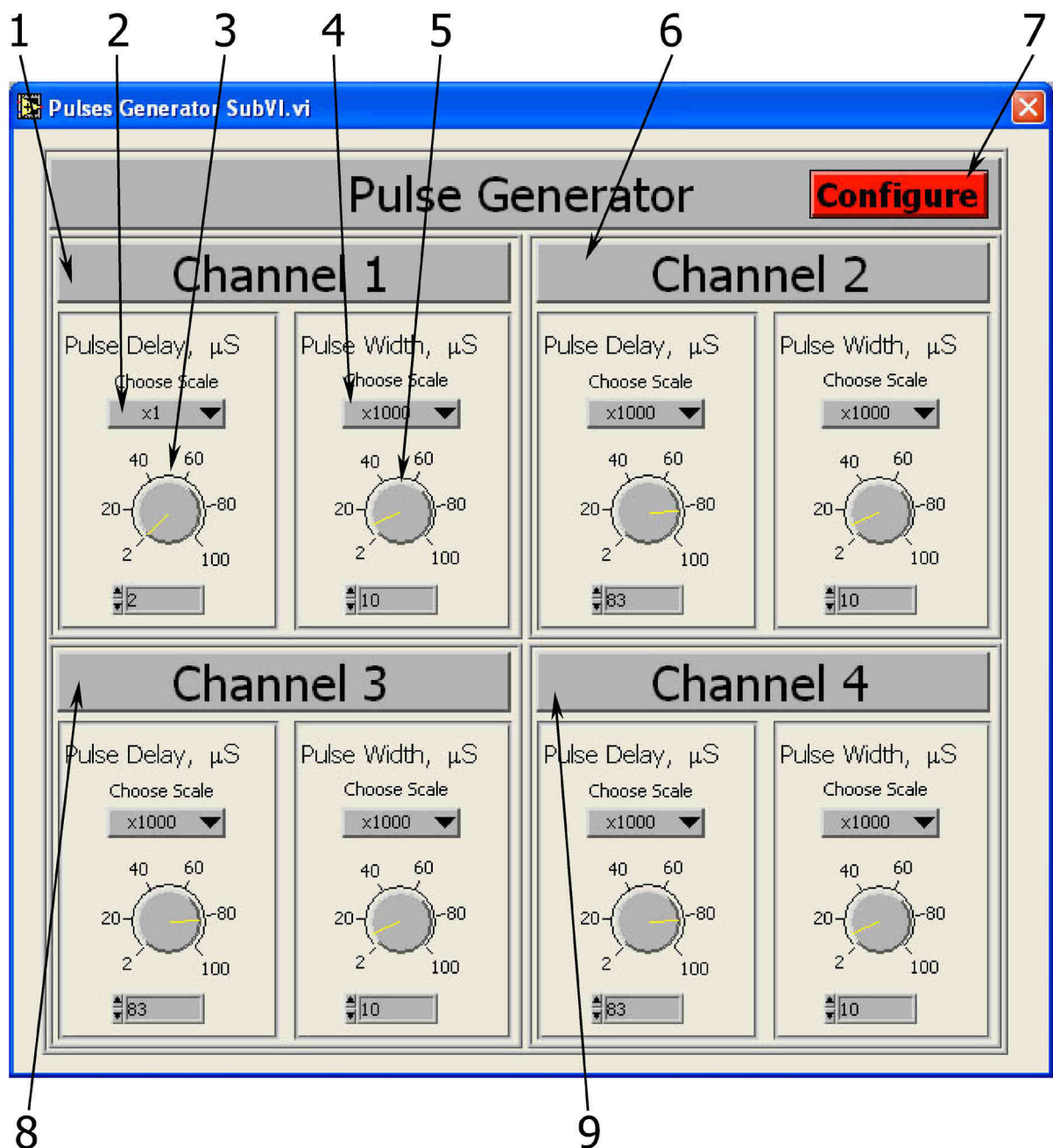


Figure 2-22 Pulse generator (front panel).

The pulse generator has four independent channels (1, 6, 8, 9) capable of delivering a single positive TTL pulse of a certain width and delay with respect to the external TTL trigger signal. *Channel 1* (1) is used to provide a pulse to one of the electrodes, which is mounted in front of the ion source, in order to chop the ion beam. *Channel 2* (6) provides a required pulse to the 22-pole trap exit electrode in order to extract trapped ions toward the Daly detector. Simultaneously, part of the output of channel 2 is sent to the counter gate input. This ensures that

counter will collect an ion signal only when ions are extracted. As one can see from Figure 2-22, each of the channels has two dial knobs. The first (e.g. 3 on channel 1) sets a proper pulse delay with respect to the trigger pulse, while the second (e.g. 5 on channel 1) sets the pulse width. The exact value can be read out from the digital displays placed below each of the dial knobs. The default scale is set to the μs regime, but can be redefined by a multiplexer available on each four channels (e.g. 2, 4 on channel 1).

2.3.3 *Sunlight EX OPO laser spectrometer.*

The front panel of LabView program, which controls laser system is shown in Figure 2-23.

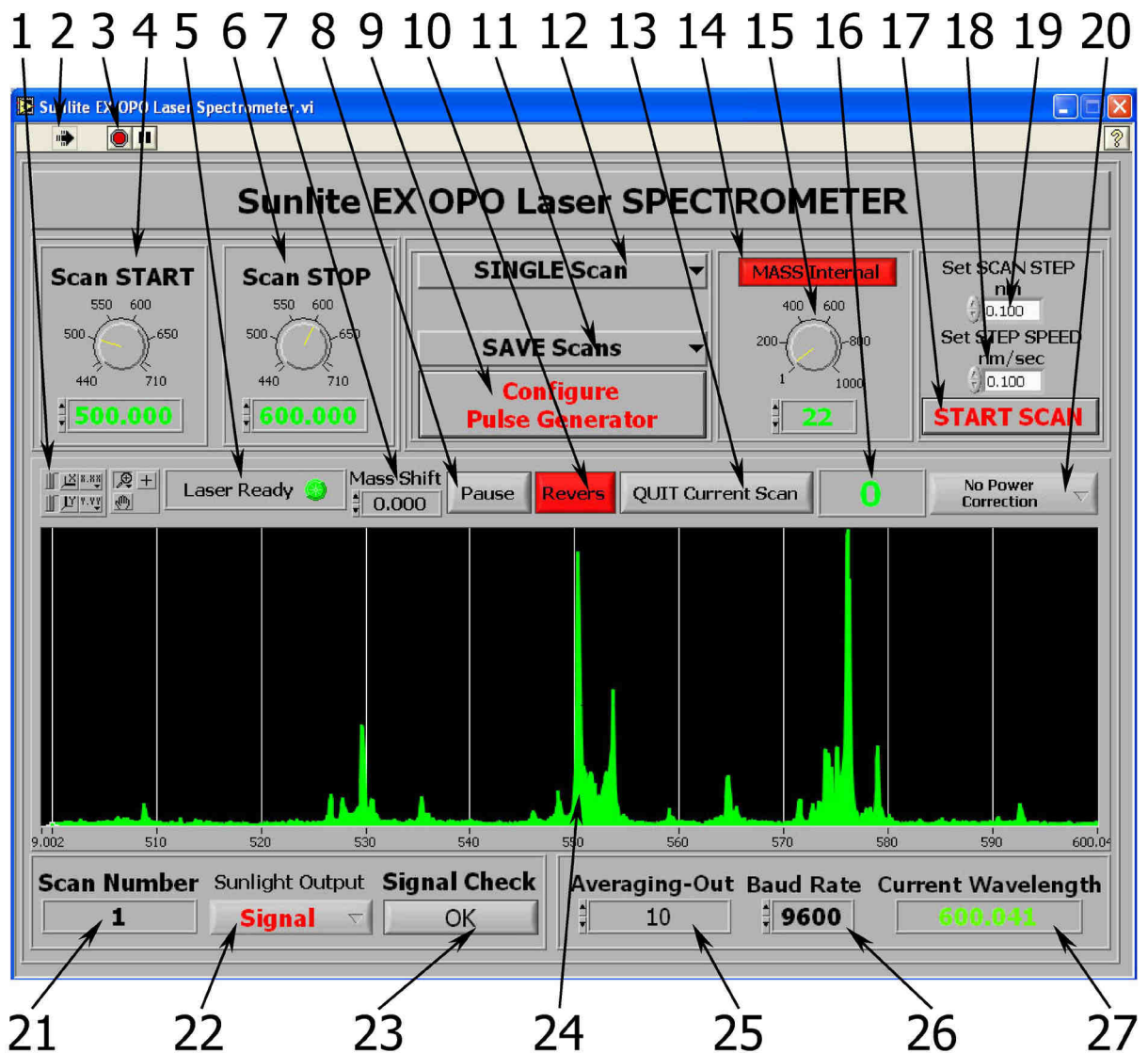


Figure 2-23 LabView program (front panel) for the Sunlight EX OPO laser system.

Before one starts the program a proper communication rate (baud rate) must be defined using the *baud rate* digital control (26). Allowed values are 1200, 2400, 4800, 9600 (default). In order to start the program press button 2 in the left top corner of the program window. Bottom 3 stops the running program at any time. The start and finish wavelength of the scan are defined by the *scan start* (4) and *scan stop* (6) dial knobs. The exact wavelength values can be seen on the digital displays below each of the dial knobs. The mass control can be done from the program or manually from quadrupole control unit. By pressing button 14 one can easily switch between the two modes. The *internal* mode is highly recommended! Dial knob 15 sets the mass of the fragment ions. The exact value can be seen on the digital display placed below the dial

knob. In addition, one has to select the right *mass shift* value (7), which must be taken from the Nermag mass spectrometer program. This ensures being on the maximum of signal of fragmented ions.

The Sunlight output is defined from dialog button 22. Output can be either signal or idler or doubled signal/idler. The wavelength scan can be performed in three different ways, as chosen by the drop-down dialog button 12. One of the options is a *single scan*: after one successful mass scan the program will stop and wait until the *start scan* button (17) is pressed again. This option is usually used for recording an absorption spectrum. The second option is a *finite scan*, which performs a set number of multiple scans. This option can be used to record and average a few absorption spectra. The actual scan number can be read from the *scan number* display (21). The last scan option involves making an infinite number of scans. Here, *continuous scan* has to be chosen. The last mode is the best for adjusting of laser power or alignment. One can directly see changes in the absorption spectrum on the screen (24).

With the drop-down dialog button 11 one can choose whether the mass spectrum will be saved as a txt file or displayed on the screen. The control 19 defines the scan step-size. The minimum step can be as small as 0.001 nm. In addition, one has to define the speed of the wavelength change (18). In order to avoid a wavelength jitter it is important that the total time of the wavelength change must not be less than 0.5 second per step. The number of fragmented ions at each particular wavelength can be read out from the digital display 16.

An absorption spectrum can be displayed on the screen either as collected or as normalized by the laser power curve. By choosing the normalization procedure from the drop-down dialog button (20), the current spectrum can be normalized either by a first or a second order correction.

The *Laser ready* indicator (5) shows the status of the laser. When the LED is green the laser has already changed the wavelength, while when red indicates that the wavelength change is still in progress. The LED should normally be either always green or blinking,

indicating a change in wavelength. The current wavelength can be read out from digital display 27.

The scale of the spectrum can be adjusted while scanning through a set of instruments (1), where changes can be seen directly on screen (24). The *Pause* button (8) can be pressed when one would like to check the laser stability, power and etc., without interfering with the current scan. After all the checks are done one may return to the spectrum acquisition by simply pressing the pause button once again.

If necessary the pulse generator can be reconfigured by pushing button 9. How to configure the pulse generator has been already discussed. The *reverse* button (10) changes the direction of the wavelength scan. Once it is pressed the stop button (6) starts blinking in order to indicate that the end wavelength value has to be changed as soon as possible. If the *reverse* button is red laser scans from blue to the red (from higher energy to lower one). If the button is blue the wavelength scans from red to the blue (from lower energy to the higher one).

The current scan can be interrupted at any time by pushing button 13. This ensures that all the data will be properly saved. A green button indicates that quitting of the current scan takes place. Please do not push any buttons. When it is grey the current scan has been successfully terminated. If the recorded spectra are noisy one can perform a signal average using digital control 25. Recording the whole spectrum will take longer time but will result in a better signal-to-noise ratio.

The *signal check* button (23), displays the number of ions (Figure 2-20). The features of the *signal check* windows have been already discussed. A laser is usually connected to a PC via RS232 port. The connection, based on optical fibers (Figure 2-24), significantly reduces any interference from parasitic electrical signals always present in a laboratory.

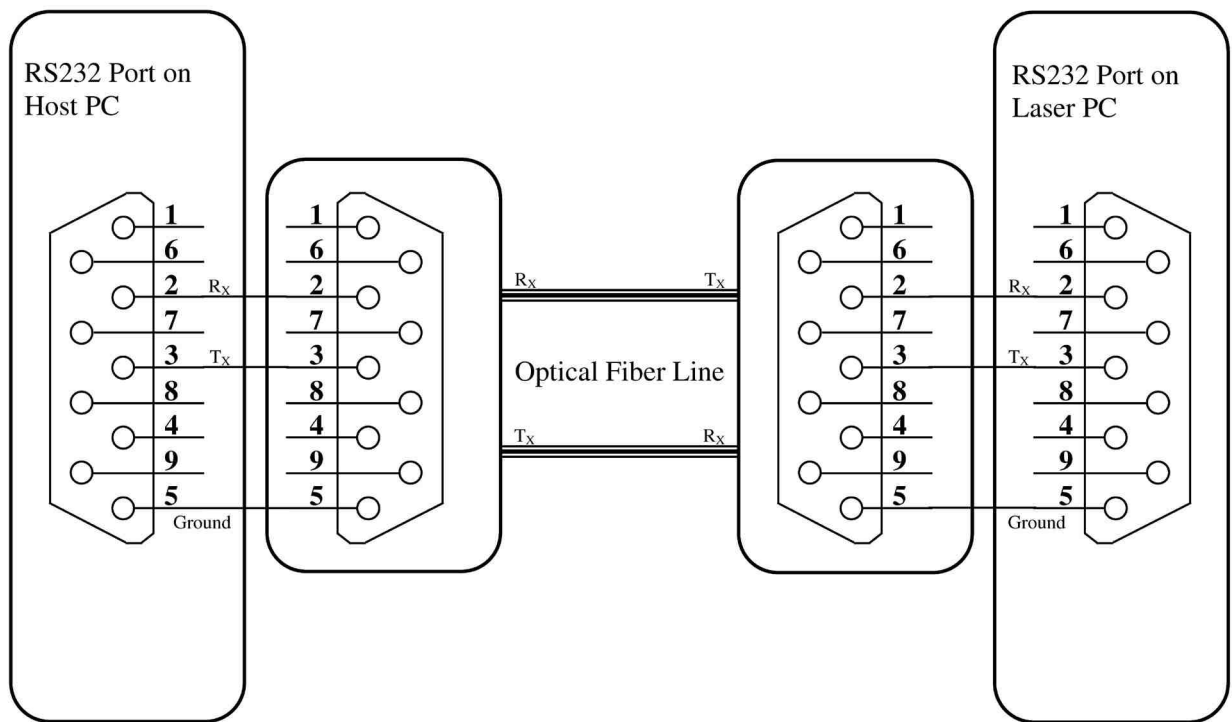


Figure 2-24 Host PC and Laser PC connection based on optical fibers.

This becomes especially important when lasers are running in a nearby laboratory. In this case a long RS232 electrical cable will not properly function.

2.3.4 Data acquisition cards and electrical connection.

There are three different types of data acquisition (DAQ) cards installed. PCI-6023E, PCI-6713 by National Instruments and PCI-DAS6014 by Measurement Computing Corporation. In the current setup these cards are named internally as *device 1*, *device 2* and *device 3*, respectively. The DAQ cards are used to provide all required analog voltages, TTL signals and high precision pulse sequence. The DAQ cards serve like a bridge between the software installed on the PC and the control units for the electronic instruments, e.g. quadrupole mass spectrometers, lasers and etc. It also helps to synchronize the operation of all the experimental equipment.

2.3.4.1 PCI-6023E (device 1).

The DAQ board (device 1) has no digital-to-analog converter outputs! It only provides up to 16 analog inputs (0 through 15). Each channel pair, ACH $\langle i, i+8 \rangle$ ($i = 0..7$), can be configured as either one differential input or two single-ended inputs. The analog inputs have 12-bit resolution. The input ranges are bipolar-only. They have four ranges of $\pm 10V$, $\pm 5V$, $\pm 500mV$, $\pm 50mV$. The ranges are software-selectable. PCI-6023E provides up to eight digital lines. Each of the lines can be configured either as digital input or output (software-selectable function). This device uses the National Instruments DAQ-STC system timing controller for time-related functions. The DAQ-STC consists of three timing groups that control analog input, analog output, and general-purpose counter/timer function. These groups include a total of seven 24-bit and three 16-bit counters and maximum timing resolution of 50 ns. The DAQ-STC enables such applications as buffered pulse generation, equivalent time sampling, and seamless changing of the sampling rate.

Table 5 gives a brief summary of the technical details and functions of the PCI-6023E board.

Table 5 A brief summary of some features of the PCI-6023E (device 1) board with technical specification.

Board Feature	Technical specification	
	Parameter	Characteristic
Analog Output	Number of outputs	Not available on this type of board
Analog Input	Number of inputs	16 (single-ended mode) 8 (differential mode)
	Signal Type and Direction	Input only
	Resolution	12-bits, 1 in 4096
	Impedance	100G Ω in parallel with 100 pF
	Protection	On 42V, Off 35V
	Input signal range	Bipolar only: $\pm 10V$, $\pm 5V$, $\pm 500mV$, $\pm 50mV$ (Software-selectable)
	Input coupling	DC
	Sampling rate	200kS/s
	Monotonicity	12-bits, guaranteed monotonic
	DNL	± 0.3 LSB typical, ± 1.0 LSB max
Digital Input / Output	Digital Type	Discrete, 5V/TTL/CMOS compatible

Counter	Number of I/O Configuration	8 8 bits, independently programmable for input or output. All pins pulled up to +5VDC via 50k Ω resistors.
	Input high voltage	2.0V min, 5.0V max
	Input low voltage	0V min, 0.8V max
	Output high voltage	4.35V min
	Output low voltage	0.4V max
	Data transfer	Programmed I/O
	Power up / reset state	Input mode (high impedance)
	User counter type	DAQ-STC
	Number of Channels	2
	Resolution	24-bit
	Frequency Scalers	1, 4-bits
	Compatibility	5V/TTL/CMOS
	GRCTRn base clock source (software selectable)	Internal 20 MHz, 100 kHz and frequency scalars 10 MHz, 100 kHz or External (GPCTRn_SOURCE)
	Internal 20 MHz clock source stability	$\pm 0.01\%$
	Counter n Gate	Available at connector (GPCTRn_GATE)
	Counter n Output	Available at connector (GPCTRn_OUT)
	Clock input frequency	20 MHz max
Pulse width (clock input)	10 ns min (in edge-detect mode)	
Pulse width (gate)	10 ns min (in edge-detect mode)	

2.3.4.2 PCI-6713 (device 2).

The board (device 2) has no analog inputs! This is a Plug and Play, analog output, digital, and timing I/O device for PCI bus computers. This card features a 12-bit digital-to-analog converter with update rates up to 1 MS/s/channel for voltage output. There are up to eight voltage output channels available. In addition, PCI-6713 card has eight lines of TTL-compatible DIO, and 24-bit counter/timers for TIO.

The National Instruments device has no DIP switches, jumpers or potentiometers, so one can easily software configure and calibrate it. This device, as well as previously described, uses the National Instruments DAQ-STC system timing groups that control the analog inputs and outputs, and general-purpose counter/timing functions. These groups include a total of seven

24-bit and three 16-bit counters and have a maximum timing resolution of 50 ns. Table 6 gives a brief summary of the technical details and functions of the PCI-6713 board.

Table 6 A brief summary of some features of the PCI-6713 (device 2) board with technical specification.

Board Feature	Technical specification Parameter	Characteristic
Analog Output	D/A Converter type	Double-buffered, multiplying
	Signal Type and Direction	Output only
	Resolution	12-bits, 1-in-4096
	Number of Channels	8 voltage output
	Voltage Range	$\pm 10V$, $\pm EXTREF$
	Monotonicity	12-bits, guaranteed monotonic
	DNL	± 0.3 LSB typ, ± 1.0 LSB max
	Slew Rate	20V/ μ s min
	Settling Time (full scale step)	3 μ s to ± 0.5 LSB accuracy
	Noise	200 μ V _{rms} , DC to 1MHz
	Current Drive	± 5 mA max
	Output short-circuit duration	Indefinite @25mA
	Output coupling	DC
	Output impedance	0.1 ohms max
	Power up and reset	DACs cleared to 0 V ± 250 mV max
Analog Input	Number of inputs	Not available on this type of board
	Digital Input / Output	Discrete, 5V/TTL/CMOS compatible
Digital Input / Output	Number of I/O	8
	Compatibility	5V/TTL/CMOS
	Configuration	8 bits, independently programmable for input or output. All pins pulled up to +5VDC via 50k Ω resistors.
	Input high voltage	2.0V min, 5.0V max
	Input low voltage	0V min, 0.8V max
	Output high voltage	4.35V min
	Output low voltage	0.4V max
	Data transfer	Programmed I/O
	Power up / reset state	Input mode (high impedance)
	Counter	User counter type
Counter	Number of Channels	2
	Resolution	24-bit
	Frequency Scalers	1, 4-bits
	Compatibility	5V/TTL/CMOS
	GRCTRn base clock source (software selectable)	Internal 20 MHz, 100 kHz and frequency scalars 10 MHz, 100 kHz or External (GPCTRn_SOURCE)
	Internal 20 MHz clock source stability	$\pm 0.01\%$
	Counter n Gate	Available at connector (GPCTRn_GATE)
	Counter n Output	Available at connector (GPCTRn_OUT)

Clock input frequency	20 MHz max
Pulse width (clock input)	10 ns min (in edge-detect mode)
Pulse width (gate)	10 ns min (in edge-detect mode)

2.3.4.3 PCI-DAS6014 (device 3).

The board (device 3) has two digital-to-analog outputs, as well as up to 16 analog inputs. Each input can be individually configured as single-ended or differential. The analog inputs have 16-bit resolution. The input ranges are bipolar-only. They have four ranges of $\pm 10V$ (currently in use), $\pm 5V$, $\pm 500mV$, $\pm 50mV$. The ranges are software-selectable.

The board provides nine user-configurable trigger/clock/gate pins. They are available at a 100-pin I/O connector. Six are configurable as inputs and three are configurable as outputs. Interrupts can be generated by up to seven ADC sources and up to four DAC sources on the PCI-DAS6014.

The board contains an 82C54 counter chip, which consists of three 16-bit counters. Clock, gate, and output signals from two of three counters are available on the 100-pin I/O connector. The third counter is used internally. Table 7 summarizes technical details of PCI-DAS6014 functions.

Table 7 A brief summary of some features of the PCI-DAS6014 (device 3) board with technical specification.

Board Feature	Technical specification	
	Parameter	Characteristic
Analog Output	D/A Converter type	Double-buffered, multiplying
	Signal Type and Direction	Output only
	Resolution	16-bits, 1-in-65536
	Number of Channels	2 voltage output
	Voltage Range	$\pm 10V$
	Monotonicity	16-bits, guaranteed monotonic
	DNL	± 2 LSB typ
	Slew Rate	15V/ μs min
	Settling Time (full scale step)	8 μs to ± 1.0 LSB accuracy
	Noise	360 μV_{rms} , DC to 400kHz BW

Analog Input	Glitch Energy	200mV @ 1µs duration mid-scale
	Current Drive	±5 mA
	Output short-circuit duration	Indefinite @25mA
	Output coupling	DC
	Output impedance	0.1 ohms max
	Power up and reset	DACs cleared to 0 V ±250mV max
	Number of inputs	16 (single-ended mode) 8 (differential mode)
	Signal Type and Direction	Input only
	Resolution	16-bits, 1 in 65536
	Impedance	100GΩ in normal operation
Digital Input / Output	Protection	On ±25V, Off ±15V
	Input signal range	Bipolar only: ±10V, ±5V, ±500mV, ±50mV (Software-selectable)
	Input coupling	DC
	Sampling rate	200kS/s min
	Monotonicity	16-bits, guaranteed monotonic
	Digital Type	Discrete, 5V/TTL compatible
	Number of I/O	8
	Configuration	8 bits, independently programmable for input or output. All pins pulled up to +5V via 47K resistors (default). Positions available for pull down to ground. Hardware selectable via solder gap.
	Input high voltage	2.0V min, 7.0V absolute max
	Input low voltage	0.8V max, -0.5V absolute min
Counter	Output high voltage	3.80V min, 4.20V typical
	Output low voltage	0.55V max, 0.22V typical
	Data transfer	Programmed I/O
	Power up / reset state	Input mode (high impedance)
	User counter type	82C54
	Number of Channels	2
	Resolution	16-bit
	Compatibility	5V/TTL
	CTRn base clock source (software selectable)	Internal 10 MHz, 100KHz or External (CTRn CLK)
	Internal 10MHz clock source stability	50 ppm
Counter n Gate	Available at connector (CTRn GATE)	
Counter n Output	Available at connector (CTRn OUT)	
Clock input frequency	10 MHz max	
High pulse width (clock input)	15 ns min	
Low pulse width (clock input)	25 ns min	
Gate width high	25 ns min	
Gate width low	25 ns min	
Input low voltage	0.8V max	
Input high voltage	2.0V min	
Output low voltage	0.4V max	
Output high voltage	3.0V min	

2.3.4.4 DAQ cards electrical connections.

The software described earlier, summarizes all the user provided settings and sends the commands to the DAQ cards. According to the commands sent, the DAQ cards provide direct voltage outputs, pulse sequences as well as analyze TTL signals or input voltages. Thus to work together at the same time the DAQ card outputs (devices 1, 2, 3) are externally connected with each other and with the controlled devices. Figure 2-25 shows all current electrical connections required for the DAQ card outputs. Table 8 summarizes the electrical connections between DAQ cards and external equipment.

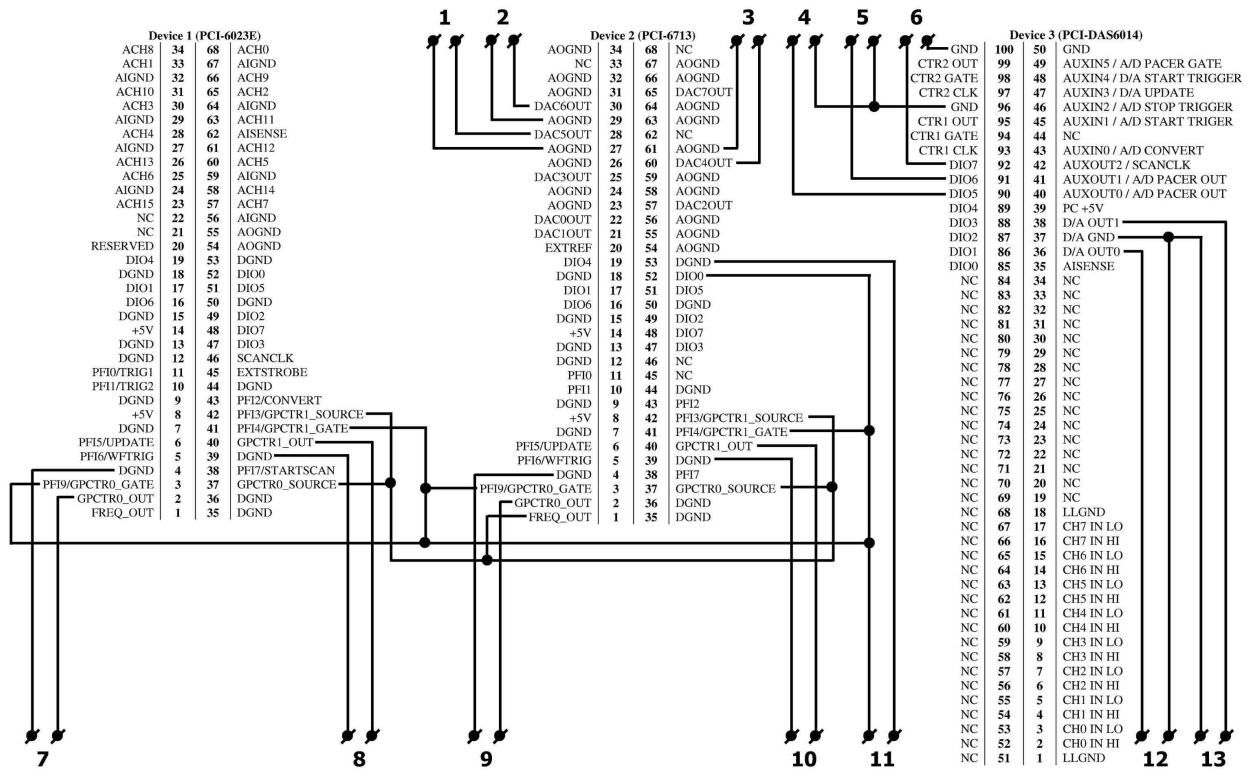


Figure 2-25 DAQ cards electrical connection diagram.

Table 8 Connections between DAQ card outputs and external electronics.

Connector Number	Data transfer	External device	Application
1	Voltage output	ABB Extrel QMS	Input: Delta M; -10...+10V, 12-bit.
2	Voltage output	ABB Extrel QMS	Input: Pole Bias; -10...+10V, 12-bit.
3	Voltage output	ABB Extrel QMS	Input: Resolution; -10...+10V, 12-bit.

4	Digital output	ABB Extrel QMS	Input: Pole Bias Reverse; TTL: low, high.
5	Digital output	ABB Extrel QMS	Input: Differential/Integral Mode; TTL: low, high.
6	Digital output	Nermag QMS	Input: External/Internal Mass Set; TTL: low, high.
7	Pulse output	Fast switch.	Input: Channel 1; Single pulse with certain delay and width. To provide a pulse of potential on source lens of the apparatus.
8	Pulse output	Fast switch.	Input: Channel 2, Ion counter gate; Single pulse with certain delay and width. To provide a pulse of potential on exit electrode of the 22-pole trap. Counter gate signal.
9	Pulse output	Fast switch.	Input: Channel 3; Single pulse with certain delay and width. Not in use.
10	Pulse output	Fast switch.	Input: Channel 4; Single pulse with certain delay and width. Not in use.
11	Digital input	BNC Pulse Generator.	Output: 10 Hz pulse sequence; External trigger for the whole experiment.
12	Analog output	ABB Extrel QMS	Input: Mass set, 0...+10V, 16-bit.
13	Analog output	Nermag QMS	Input: Mass set, 0...+10V, 16-bit.

2.3.4.5 Software pulse generator.

The Pulse generator is based on four counters. One pair of counters is built-in on the PCI-6023E board (device 1). Another pair is built-in on the PCI-6713 board (device 2). Each counter has two inputs and one output, which are shown in Figure 2-26.

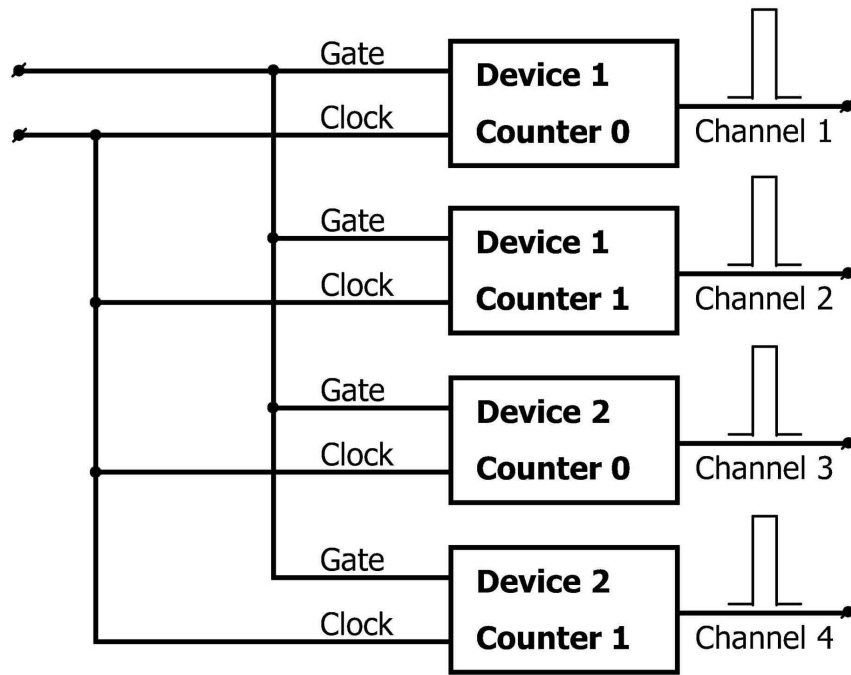


Figure 2-26 Block diagram for the software pulse generator.

Input GPCTR n _SOURCE named clock acts as a bias frequency input for counter n . GPCTR n _GATE named Gate acts as a trigger signal input. Output GPCTR n _OUT named channel provides a high precision single pulse on each falling slope of the trigger pulse.

A bias frequency of 1 MHz, taken from pin FREQ_OUT (device 2), is sent to each of four GPCTR n _SOURCE inputs. The frequency output can be configured from software to generate any kind of desired frequency value. As higher frequency is as more precise pulse width and delay one can obtain. Why it is so will become clear further on.

Each counter n configured from the *Pulse Generator* program generates a single pulse with a certain delay to a trigger signal and certain pulse width. After successful trigger counter starts counting number of bias frequency cycles. When the number of counts becomes equal to certain (software-selectable) value, the counter output GPCTR n _OUT will go from low to high value. The output will remain high unless the number of counts of bias frequency is less than a certain value. After that counter output GPCTR n _OUT will go to low again.

Thus a counter output generates a single pulse with a certain delay and width. Since the bias frequency equals to 1 MHz, time jitter will be as low as 1 μ s ($1/\Omega$).

2.4 Experimental approach.

The apparatus and experiment have been described. [54] Solid precursors, like 2,4-hexadiyne (C_6H_6) or *para*-dichlorobenzene (*p*-DCB), were placed directly into a stainless steel oven, which was heated up to the required temperature (40 $^{\circ}$ C) by a resistive wire. The vapor flowed through a 0.5 mm orifice after which electron impact ionization took place.

For gaseous precursors, like N_2O or diacetylene, sample vapours were admitted to the ionisation region through a needle valve. N_2O is commercially available and stored in a 1 L gas bottle at a pressure of around 11 bar. Diacetylene was synthesized by Jacques Lecoulre and stored in a 1 L gas bottle at a pressure not higher than 500 mbar. This was done due to diacetylene's explosive nature. Larger amounts of diacetylene must be stored as a frozen solid sample at -80 $^{\circ}$ C!

The pressure value in the ionization region was kept at $\approx 4 \times 10^{-6}$ mbar (calibrated by N_2). The ionizing electrons' energy was adjusted to be slightly above the target molecule's ionisation potential, 9 - 10 eV for *p*-DCB $^+$ and 2,4-hexadiyne, 12 - 13 eV for N_2O^+ and around 12-30 eV for diacetylene, depending on the size of the carbon chain.

The apparatus is run in a pulsed mode and the experiments were carried out at 10 Hz (Figure 2-27). The pulse sequence is generated by a software *pulse generator*, which has already been described above.

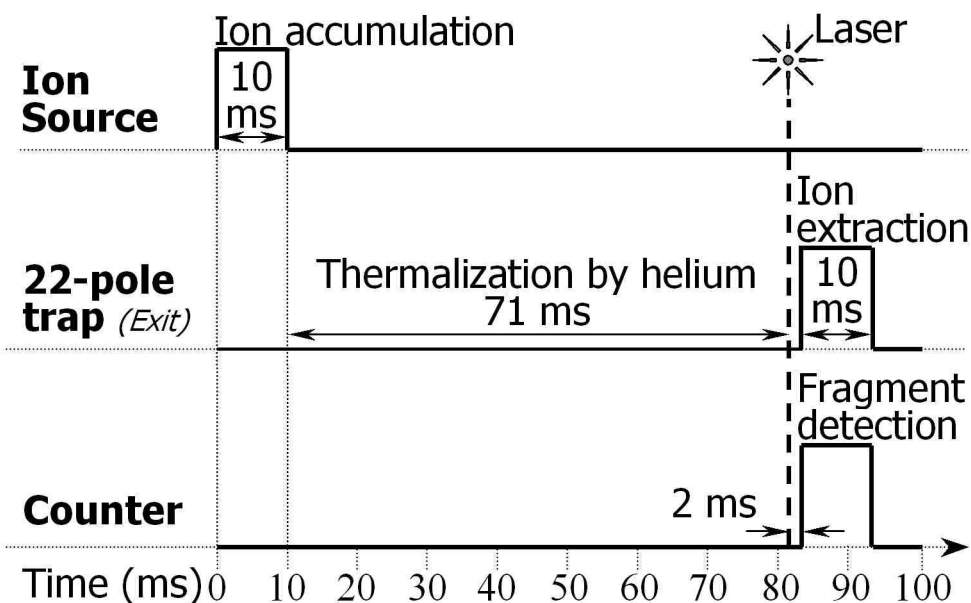


Figure 2-27 Timing and pulse sequence for the measurements carried out at 10 Hz.

Ions generated by the source are mass selected by the first quadrupole and are accumulated in the 22-pole trap for 10 ms through collisions with $\approx 10^{-4}$ mbar helium buffer gas. Following this, the potential of an electrostatic lens at the exit of the ion source is raised preventing more ions from reaching the trap. The ions are constrained in the trap by a RF field and undergo collisions with helium gas cooled by a cryostat operating at 6 K.

After being in the trap for 71 ms the ions are probed using either a one-colour or two-colour pump-probe approach. In the case of an one-colour experiment, the light (typically 3 mJ) comes from a tunable OPO laser system (0.3 cm^{-1} bandwidth). A dye laser system was used for the higher resolution (0.03 cm^{-1}) measurements.

In the case of two-colour pump-probe experiment, the light was provided from both a tunable Nd:YAG pumped OPO laser (0.3 cm^{-1}) and the fixed doubled output from a broadband OPO system (6 cm^{-1}). Tunable radiation was used to promote an electronic excitation. A subsequent UV photon was then used to initiate fragmentation of the excited ions. For optimum signals the two laser beams must be overlapped in both time and space. The laser beams were combined using a highly reflective 45° mirrors (200-355 nm). The tunable radiation

was passed through the mirror while the fixed UV beam was reflected by 90° to be collinear with it. Time overlap was monitored using two identical photodiodes; jitter was less than 10 ns.

After a laser excitation, the potential of the exit lens of the trap is lowered for 10 ms allowing the ions to exit through the second quadrupole mass filter, which is set to the mass of the photofragment ions. The latter are eventually detected by a Daly detector, the output of which is sent to a discriminator. Each detected ion produces a uniform spike (5 ns, 5 V) on the discriminator output, sent to a 300 MHz counter. The number of fragment ions is counted as a function of the laser wavelength to provide the absorption spectrum. The spectrum is normalized for photon intensity, monitored shot to shot by a photodiode. Each data point is an average of 50 cycles. Typically, $5-10 \times 10^4$ ions are trapped and irradiated on each cycle. The background fragment count (without laser light) was usually < 10 per cycle.

Chapter 3 Results and discussion.

3.1 One-photon two-colour photofragmentation spectroscopy.

3.1.1 N_2O cation.

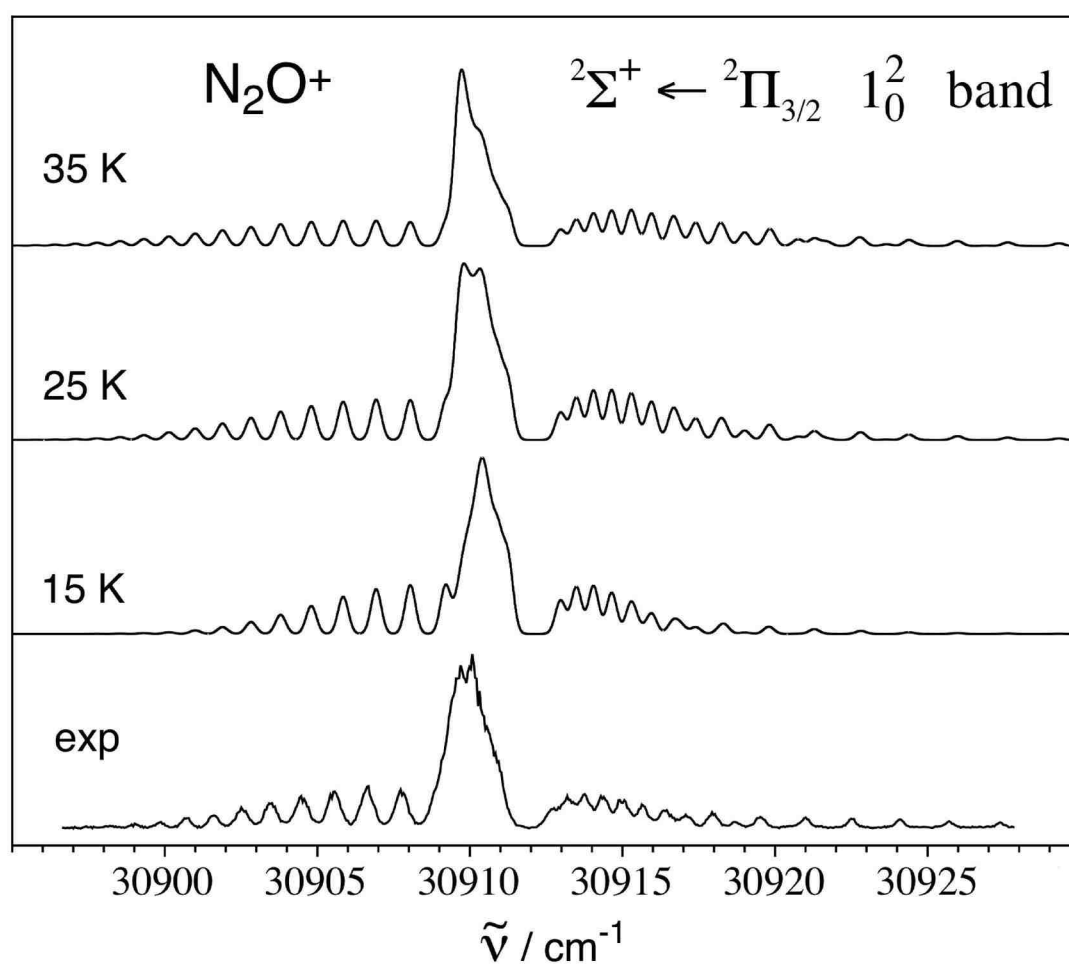


Figure 3-1 The absorption spectrum of N_2O^+ obtained by monitoring the NO^+ fragment count as a function of photon wavelength. Also shown are simulated spectra for temperatures of 15, 25 and 35 K.

The $\tilde{A} \ ^2\Sigma^+ \leftarrow \tilde{X} \ ^2\Pi_{3/2}^+$ band of N_2O^+ is shown in Figure 3-1. Also shown are simulated spectra for temperatures of 15, 25 and 35 K. [76, 77] Molecular constants used in the simulations are $B'' = 0.41157 \text{ cm}^{-1}$, $D'' = 0.2985 \times 10^{-6} \text{ cm}^{-1}$, $q'' = 1.13 \times 10^{-3} \text{ cm}^{-1}$, $A'' = 132.434 \text{ cm}^{-1}$, $B' = 0.42893 \text{ cm}^{-1}$, $D' = 0.2855 \times 10^{-6} \text{ cm}^{-1}$, and $\gamma' = 7.0 \times 10^{-4} \text{ cm}^{-1}$ and are taken from [17, 18]. It is apparent that the experimental spectrum corresponds well to the $T = 25 \text{ K}$ simulated spectrum indicating that the N_2O^+ ions' rotational degrees of the freedom are effectively cooled by collisions with the helium buffer gas. In principle it is also possible to assess the translational temperature of the N_2O^+ ions through the Doppler broadening of the rovibronic lines. However, in the present case this was not possible because the bandwidth of the OPO radiation ($\approx 0.5 \text{ cm}^{-1}$) was much greater than anticipated Doppler broadening ($\approx 0.017 \text{ cm}^{-1}$ at 25 K).

3.1.2 2,4-hexadiyne cation.

3.1.2.1 Internal temperature of 2,4-hexadiyne cation.

The electronic absorption process was monitored via the fragmentation channel leading to C_6H_5^+ , C_6H_4^+ and C_4H_4^+ .

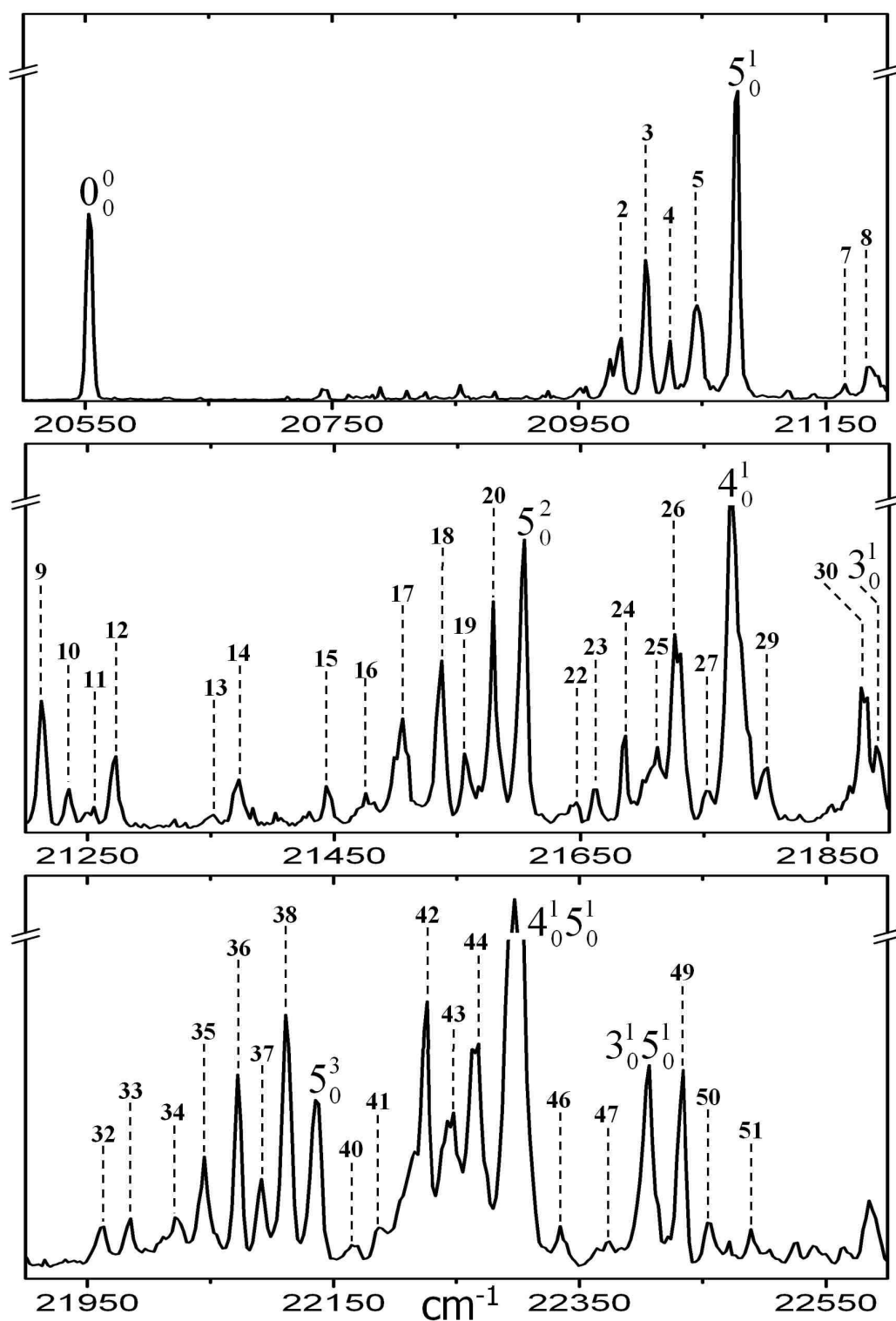


Figure 3-2 The $\tilde{A} \ ^2E_u \leftarrow \tilde{X} \ ^2E_g$ transition of 2,4-hexadiyne cation recorded (0.3 cm^{-1} resolution) via a one-photon predissociation process by monitoring the C_4H_4^+ fragment ions produced. The ions were vibrationally and rotationally relaxed to around 30 K by collisions with cryogenically cooled helium in a 22-pole radiofrequency trap.

Figure 3-2 shows the spectrum in the $20000\text{--}22850 \text{ cm}^{-1}$ range recorded by monitoring the number of C_4H_4^+ counts as function of laser frequency (0.3 cm^{-1} bandwidth). The relative

intensities of the vibronic bands differ somewhat for reasons discussed in the next section. The origin band at 20553 cm^{-1} stands alone and there is no evidence of hot bands of type ν_1^0 or ν_2^0 to lower energy, or sequence transitions ν_1^1 arising from residually populated vibrational levels in the \tilde{X}^2E_g ground state. The lowest frequency mode is around 120 cm^{-1} and thus the vibrational temperature is below 30 K. When the laser bandwidth is reduced to 0.03 cm^{-1} the rotational structure due to the K-stacks is resolved. This is seen in Figure 3-3 together with the quantum number assignment inferred in the analysis of the $\tilde{A}^2E_u \rightarrow \tilde{X}^2E_g$ emission spectrum [78].

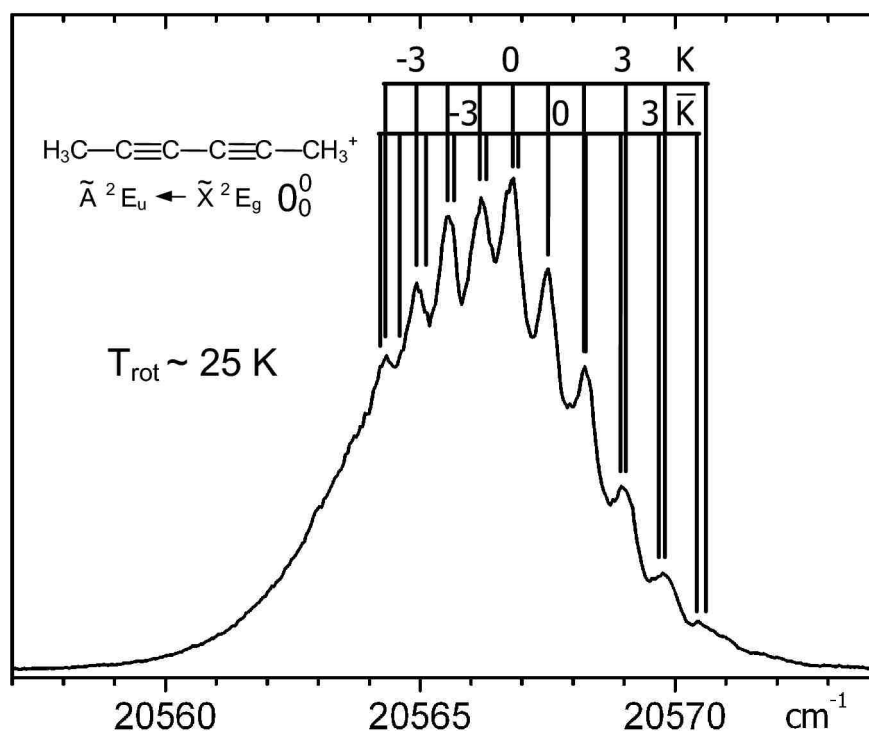


Figure 3-3 The origin band in the $\tilde{A}^2E_u \leftarrow \tilde{X}^2E_g$ transition of 2,4-hexadiyne cation detected via predissociation to C_4H_4^+ using a laser band-width of 0.03 cm^{-1} . The assignment of the K-structure is taken from [78] and the intensity distribution corresponds to a rotational temperature in the 20-30 K range.

This pattern varies with temperature and the spectrum shown in Figure 3-3 resembles closely the top trace in Figure 3-4 (reproduced from ref. [78]), i.e. a rotational temperature in the 20-30 K range.

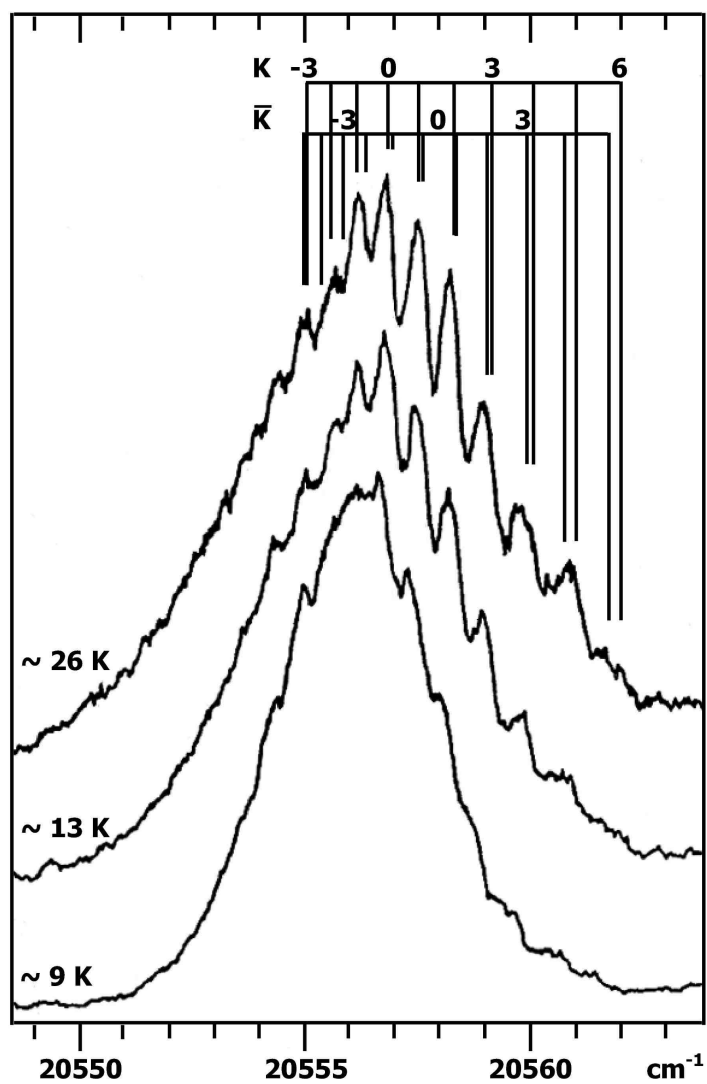


Figure 3-4 The K-structure of the origin band in the $\tilde{A} \ ^2E_u \rightarrow \tilde{X} \ ^2E_g$ transition of 2,4-hexadiyne cation. The figure is reproduced from Fig. 2 in ref. [78].

In a spectroscopic study of the related molecular ion, 1,3-pentadiyne, more details of the rotational temperature dependence on the expansion backing pressure are explicitly given [79]. The vibrational and rotational degrees of freedom are thus equilibrated to around 20-30 K.

3.1.2.2 Vibrational structure.

The electronic spectrum shows increasing complexity as the laser excitation frequency is increased. Figure 3-5 reproduces the absorption spectrum of 2,4-hexadiyne cation from ref. [33] obtained by laser induced fluorescence technique in 1980.

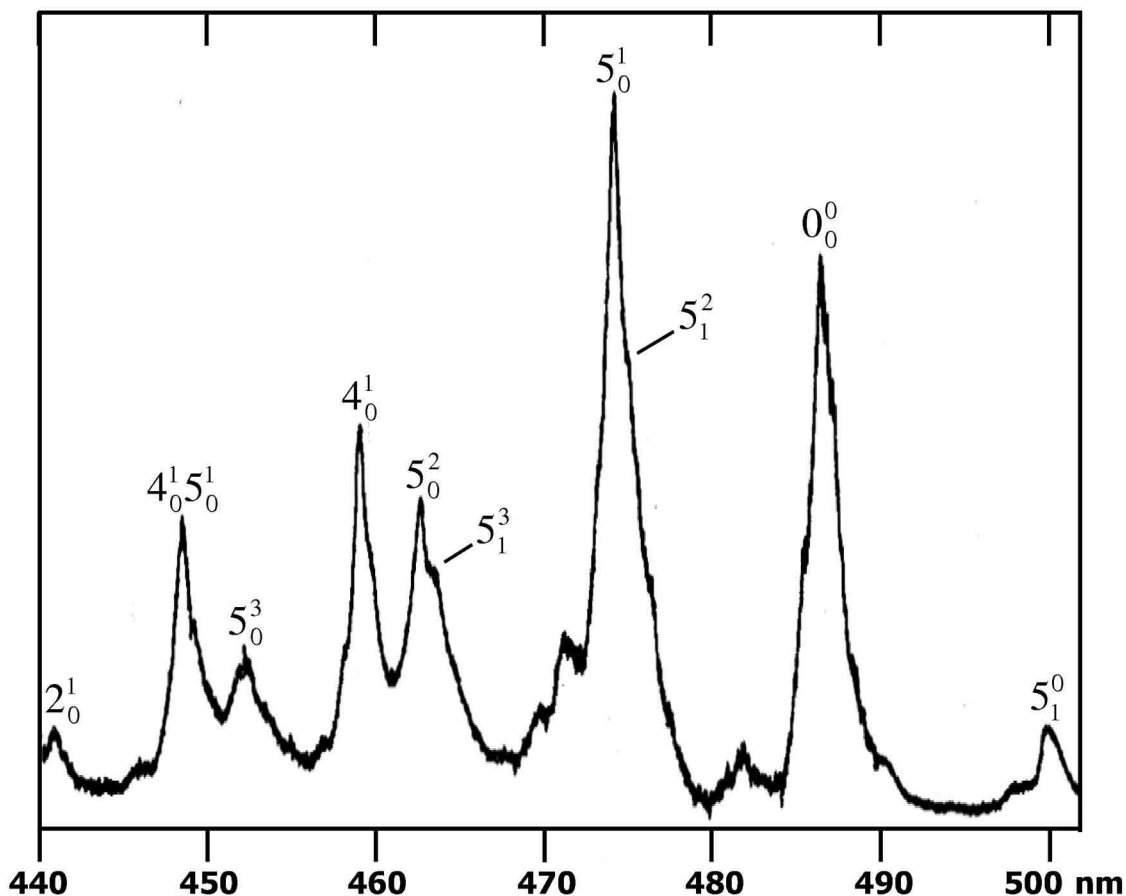


Figure 3-5 The $\tilde{A} \ ^2E_u \leftarrow \tilde{X} \ ^2E_g$ laser induced excitation spectrum of uncooled 2,4-hexadiyne cation taken in 1980 [33].

In the spectrum reported earlier, using ions relaxed to about 150 K and recorded via a laser induced fluorescence technique [33], only the totally symmetric modes (ν_1 to ν_5) appear to be strongly excited. Many more transitions are now apparent (Figure 3-2). In Table 9 the frequencies of all the observed distinct peaks in the spectrum are listed with the numbering as shown in Figure 3-2.

Table 9 Wavenumbers of vibronic bands in the $\tilde{A} \ ^2E_u \leftarrow \tilde{X} \ ^2E_g$ system of 2,4-hexadiyne cation. The numbering of the peaks is that shown in Figure 3-2.

No	Band Wavenumber (cm ⁻¹)	Relative to 0 ₀ ⁰ (cm ⁻¹)	Assignment
1	20553	0	0 ₀ ⁰
2	20984	431	
3	21004	451	
4	21024	471	
5	21046	493	
6	21079	526	5 ₀ ¹
7	21166	613	
8	21183	630	
9	21213	660	
10	21235	682	
11	21255	702	
12	21273	720	
13	21352	799	
14	21373	820	
15	21443	890	
16	21475	922	
17	21505	952	
18	21538	985	
19	21556	1003	
20	21579	1026	
21	21605	1052	5 ₀ ²
22	21647	1094	
23	21663	1110	
24	21686	1133	
25	21712	1159	
26	21726	1173	
27	21754	1201	
28	21773	1220	4 ₀ ¹
29	21801	1248	
30	21877	1324	
31	21889	1336	3 ₀ ¹
32	21961	1408	
33	21985	1432	
34	22021	1468	
35	22045	1492	
36	22072	1519	
37	22092	1539	
38	22111	1558	
39	22135	1582	5 ₀ ³
40	22165	1612	
41	22187	1634	
42	22226	1673	
43	22248	1695	
44	22268	1715	
45	22297	1744	4 ₀ ¹ 5 ₀ ¹

46	22334	1781	
47	22374	1821	
48	22407	1854	$3_0^1 5_0^1$
49	22434	1881	
50	22457	1904	
51	22489	1936	

All these are new observations leading to a detailed mapping of the $\tilde{A} \ ^2E_u$ excited electronic state manifold. The strongest bands involve the totally symmetric modes 5_0^1 , 4_0^1 and their combinations. There are too many other bands to be assigned only to transitions involving the five a_{1g} modes where the D_{3h} symmetry is retained in both electronic states, which have the frequencies of 2911, 2266, 1378, 1255 and 560 cm^{-1} in the ground state of neutral 2,4-hexadiyne [80]. For example, four distinct peaks lie just below the 5_0^1 transition (i.e. $< 500 \text{ cm}^{-1}$), which have to correspond to the excitation of the degenerate modes in two, or more, quanta. These can only be constructed from the four degenerate modes ν_{14} (350 cm^{-1}), ν_{15} (121 cm^{-1}) both of e_u symmetry, and ν_{20} (245 cm^{-1}) of e_g , where the frequencies given are the values of the neutral molecule. Thus the $14_0^1 15_0^1$, 15_0^2 , 20_0^2 transitions would each give a totally symmetric level as would 15_0^4 with several components with energies below 500 cm^{-1} . The number of such peaks increases with internal energy as more possibilities arise for the formation of totally symmetric levels by appropriate combinations of the degenerate modes, but a specific assignment would not be unambiguous. For this reason in Table 9 only the evident progressions and combinations involving totally symmetric modes are given.

The enhanced intensity of the transitions involving the degenerate modes is a result of saturation. This is illustrated in Figure 3-6 where the region around the 5_0^1 transition is recorded: *trace a* - using the same laser power as in Figure 3-2, and *b* attenuated by a factor of around 300.

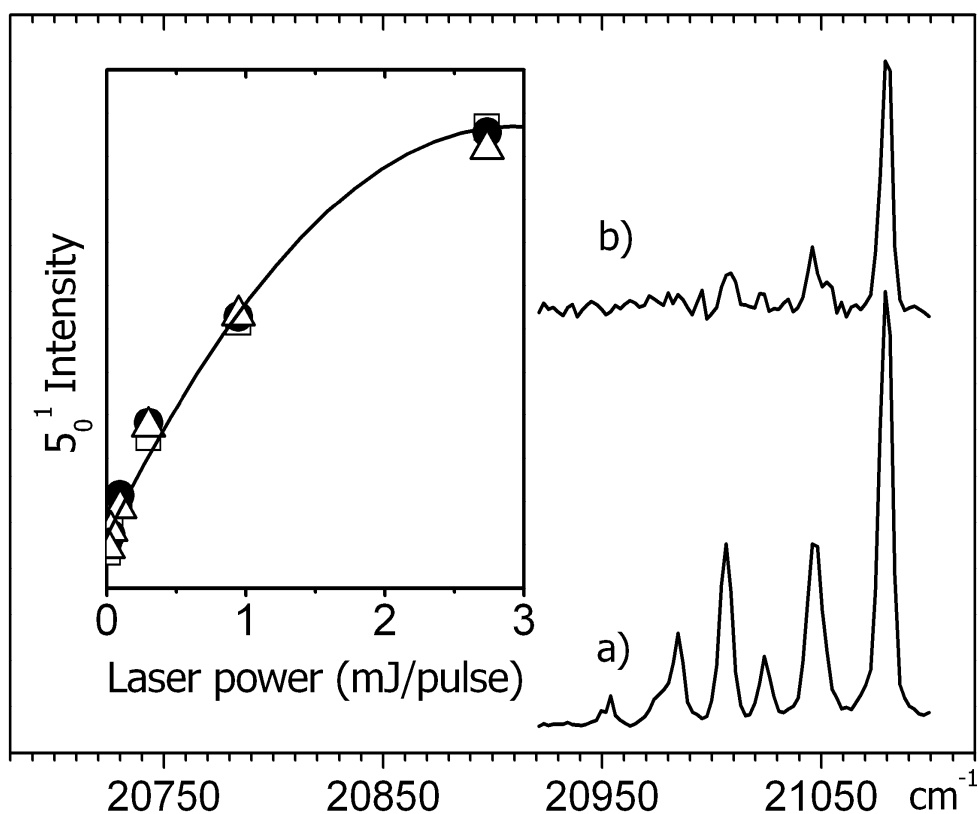


Figure 3-6 The region around the 5_0^1 transition in the $\tilde{A} \ ^2E_u \leftarrow \tilde{X} \ ^2E_g$ spectrum of 2,4-hexadiyne cation detected via predissociation to form $C_4H_4^+$ recorded: a) at 3 mJ/pulse (as in Fig. 3), b) at 9 μ J/pulse (\sim 300 times lower). The inset shows the dependence of the 5_0^1 band on laser energy indicating that the transition is saturated.

The latter measurement is a reflection of a normal absorption; the bands arising from the excitation of the degenerate modes are quite weak and reflect the Franck-Condon factors. At the higher laser density these weak transitions are saturated leading to increased intensities. At even higher powers (tens of mJ per pulse) the peaks in the spectrum broaden. The inset of Figure 3-6 shows the intensity of the 5_0^1 band plotted as function of the laser power. The non-linear dependence indicates saturation above 0.5 mJ/pulse. By this means the manifold of the vibration levels in such cold polyatomic ions is “lit-up”.

3.2 Two-photon one-colour photofragmentation spectroscopy.

3.2.1 1,4-dichlorobenzene cation.

As another test of the apparatus the spectrum of the *p*-DCB⁺ radical cation was measured over the 19100 - 22700 cm⁻¹ range by monitoring the C₆H₄Cl⁺ fragment (*i.e.*, Cl loss channel).

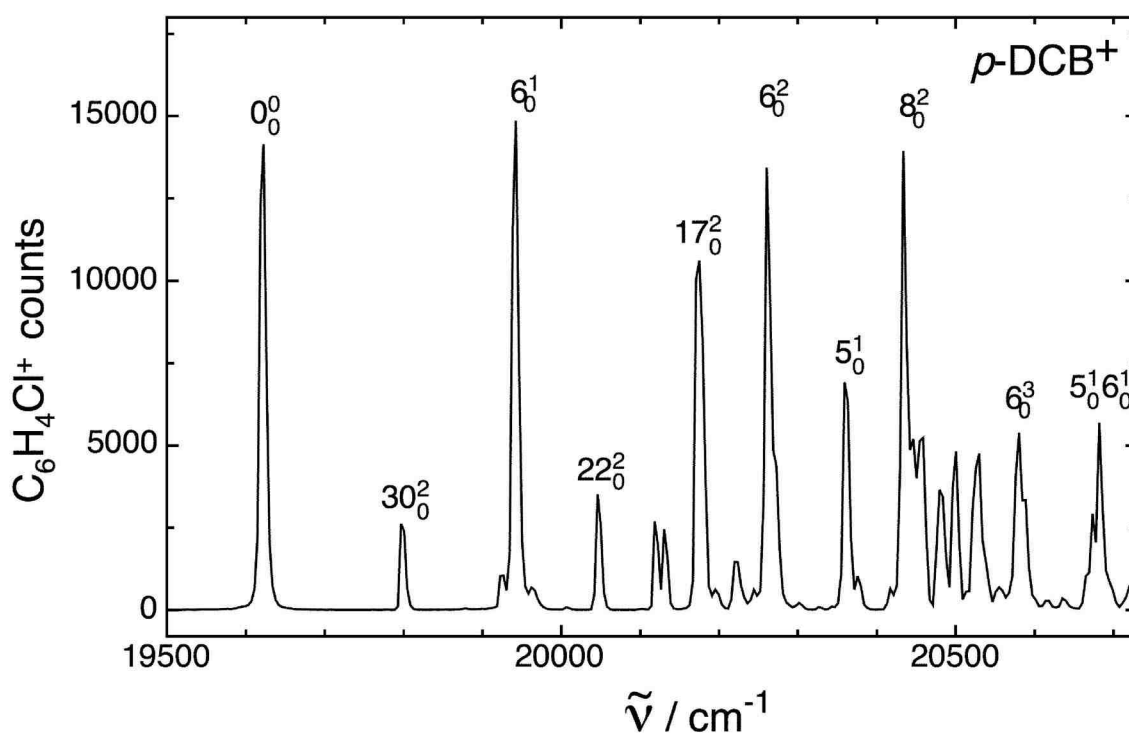


Figure 3-7 The electronic transition of the *p*-DCB⁺ radical cation over the 19500 - 20700 cm⁻¹ range obtained by monitoring the C₆H₄Cl⁺ fragment count. Wavenumbers and assignments for vibronic bands are given in Table 1.

The resulting spectrum, shown in Figure 3-7, exhibits a series of well-resolved vibronic bands that can mainly be assigned to the dipole allowed $\tilde{B}^2B_{3u} \leftarrow \tilde{X}^2B_{2g}$ transition. The excellent signal to noise ratio achieved is evident. The lower frequency bands, which have

widths of $\approx 10 \text{ cm}^{-1}$, have peak intensities that are 10^3 larger than the background level (≈ 10 counts/laser shot).

The lowest frequency transition, the $\tilde{B}^2B_{3u} \leftarrow \tilde{X}^2B_{2g} 0_0^0$ band, is observed at 19622 cm^{-1} , in excellent agreement with the value derived from the optical emission spectrum of $p\text{-DCB}^+$ ($19620 \pm 10 \text{ cm}^{-1}$) where the band was much broader (Figure 3-8). [20]

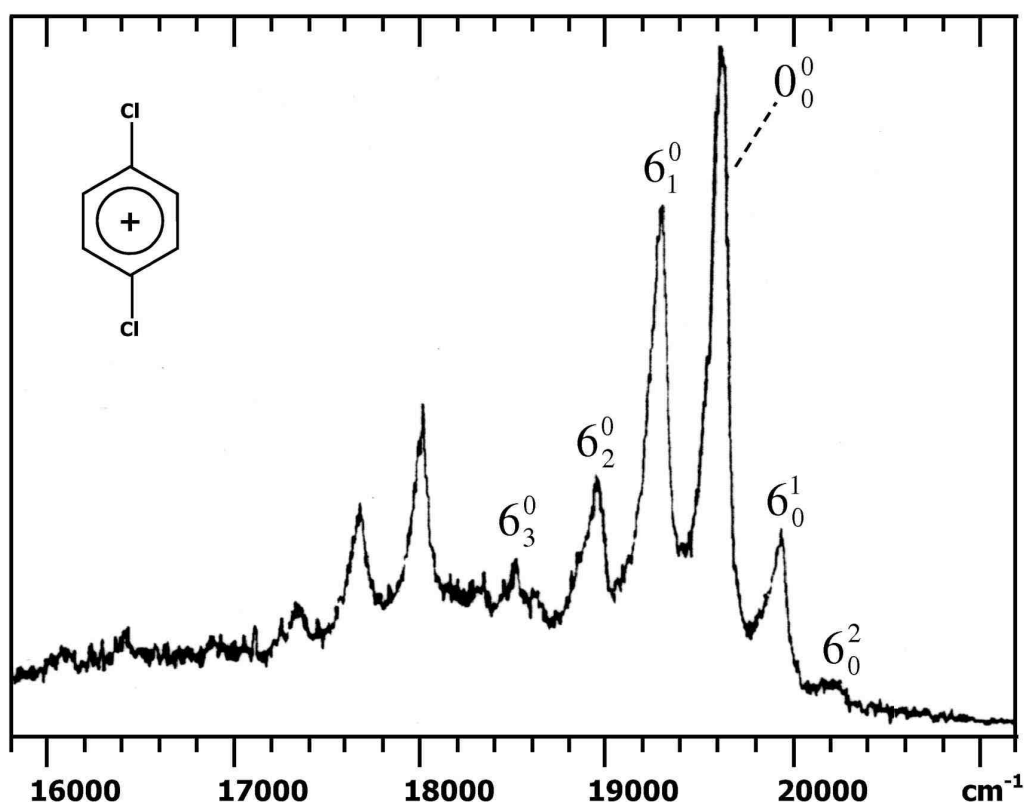


Figure 3-8 The emission spectrum of the $p\text{-DCB}^+$ radical cation over the $16000\text{-}20000 \text{ cm}^{-1}$ range obtained in 1978 [20].

For $p\text{-DCB}^+$ [21, 22, 81] the corresponding 0_0^0 transition occur at 19452 and 19212 cm^{-1} in Ne and Ar matrices respectively, representing matrix induced red shifts of 0.9 and 2.1% , respectively. Wavenumbers and assignments for the lower energy $\tilde{B}^2B_{3u} \leftarrow \tilde{X}^2B_{2g}$ transitions are listed in Table 10.

Table 10 Wavenumbers of vibronic bands for the $\tilde{B}^2B_{3u} \leftarrow \tilde{X}^2B_{2g}$ system of the p -DCB⁺ radical cation.

Band Wavenumber (cm ⁻¹)	Relative to 0 ₀ ⁰ (cm ⁻¹)	Assignment
19622	0	0 ₀ ⁰
19797	175	30 ₀ ²
19942	320	6 ₀ ¹
20046	424	22 ₀ ²
20118	496	6 ₀ ¹ 30 ₀ ²
20130	508	29 ₀ ¹ 30 ₀ ¹
20175	553	17 ₀ ²
20219	597	
20260	638	6 ₀ ²
20270	648	27 ₀ ²
20359	737	5 ₀ ¹
20434	812	8 ₀ ²
20459	837	29 ₀ ²
20479	857	16 ₀ ¹ 17 ₀ ¹
20500	878	6 ₀ ¹ 17 ₀ ²
20530	908	
20580	958	6 ₀ ³
20682	1060	5 ₀ ¹ 6 ₀ ¹ / 4 ₀ ¹

Assignments were made on the basis of a comparison between the experimental frequencies of neutral p -DCB, and with Ar matrix absorption and gas-phase emission spectra of p -DCB⁺. The prominent 320 cm⁻¹ progression, which was also observed in Ar matrix absorption spectra with a similar spacing (320 and 331 cm⁻¹), [21, 22] corresponds to the ν_6 (a_{1g}) vibration (symmetric C-Cl stretch). The enhanced spectral resolution and excellent S/N of the gas phase spectrum compared to the earlier Ar matrix absorption spectra allow us to identify a number of previously unobserved vibronic transitions including 30₀², 22₀², 6₀¹ 30₀², 29₀¹ 30₀¹, 17₀², 5₀¹, 8₀², 29₀², 16₀¹ 17₀¹ and 5₀¹ 6₀¹. Vibrational frequencies for the \tilde{B}^2B_{3u} state based on these transitions, along with corresponding values for the S_0 and S_1 states of the neutral p -DCB are given in Table 11.

Table 11 Selected vibrational frequencies bands for the S_0 and S_1 states of neutral p -DCB and for the \tilde{B}^2B_{3u} state of the p -DCB⁺ radical cation.

Mode	<i>Neutral</i> p -DCB S_0	<i>Neutral</i> p -DCB S_1	p -DCB ⁺ \tilde{B}^2B_{3u} Ar matrix	p -DCB ⁺ \tilde{B}^2B_{3u} this work	Description
5 (a_g)	747	727		737	ring def.
6 (a_g)	328	301	320 ³ 331 ⁴	320	symmetric C-Cl stretch
8 (a_u)	405	167		406	ring twist
16 (b_{2g})	687	416		581	ring twist
17 (b_{2g})	298			276	out of plane C-Cl bend
22 (b_{2u})	226	225		212	in plane C-Cl bend
26 (b_{3g})	626	538			ring def.
27 (b_{3g})	350	339		324	in plane C-Cl bend
29 (b_{3u})	485	294		420	ring twist
30 (b_{3u})	122	75		88	out of plane C-Cl bend

¹[82], ²[83, 84], ³[21], ⁴[22]

In most cases the p -DCB⁺ \tilde{B}^2B_{3u} state frequencies are similar to those of the neutral p -DCB molecule. The p -DCB⁺ spectrum becomes congested above 21000 cm⁻¹ (Figure 3-9) where the $\tilde{C}^2B_{2u} \leftarrow \tilde{X}^2B_{2g}$ transition is predicted to occur. [20]

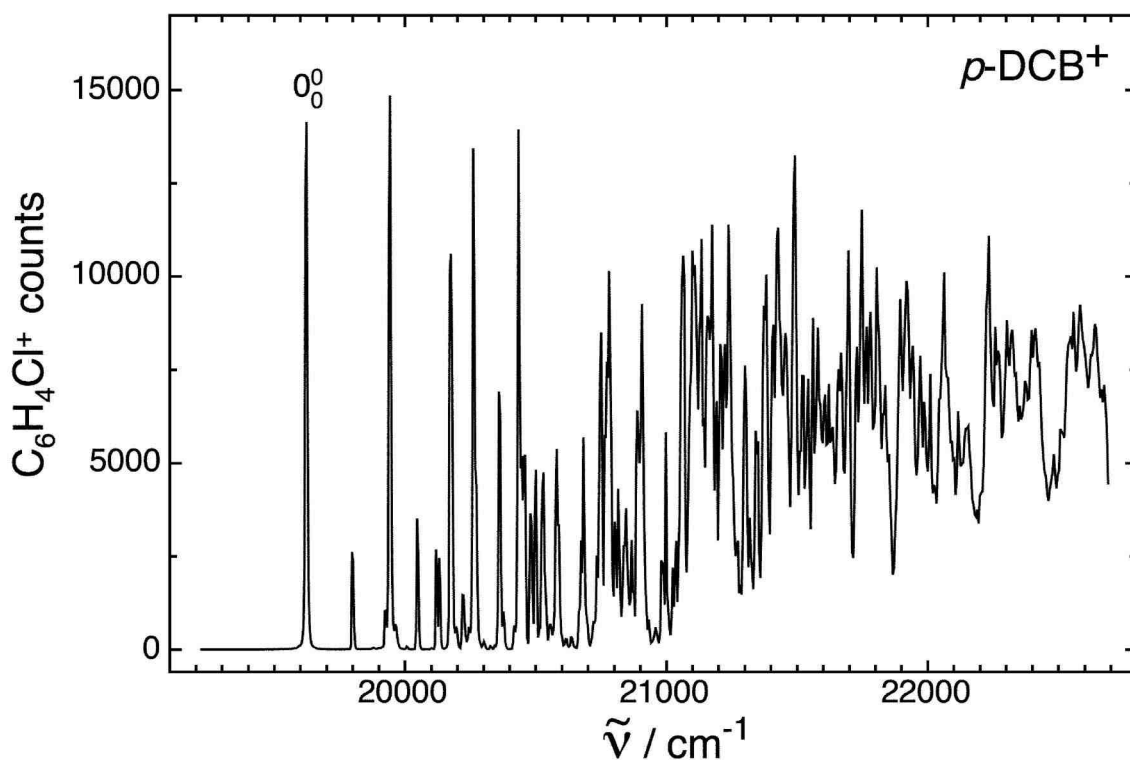


Figure 3-9 Spectrum of the $p\text{-DCB}^+$ radical cation over the 19100 - 22700 cm^{-1} range obtained by monitoring the $\text{C}_6\text{H}_4\text{Cl}^+$ fragment count as a function of photon wavelength. Transitions in the 19600 - 20700 cm^{-1} range can be assigned to the dipole allowed $\tilde{B}^2B_{3u} \leftarrow \tilde{X}^2B_{2g}$ system, while above 21000 cm^{-1} there are probably also contributions from vibronically induced $\tilde{C}^2B_{2u} \leftarrow \tilde{X}^2B_{2g}$ transitions.

Although dipole forbidden, it may be induced through vibronic coupling between the \tilde{C}^2B_{2u} and \tilde{B}^2B_{3u} states. The only mode with appropriate symmetry to couple the two states is the $\nu_9(b_{1g})$ vibration which has a frequency of 815 cm^{-1} in neutral $p\text{-DCB}$. From the photoelectron spectrum, the \tilde{C}^2B_{2u} state was estimated to lie 1045 cm^{-1} above the \tilde{B}^2B_{3u} state. It is also possible that it lies somewhat lower in energy and is effectively isoenergetic with the \tilde{B}^2B_{3u} state. [20]

The $\text{C}_6\text{H}_4\text{Cl}_2^+$ photofragmentation process is now considered. A strong photodissociation signal into $\text{C}_6\text{H}_4\text{Cl}^+$ is observed when the laser is tuned to the $\tilde{B}^2B_{3u} \leftarrow \tilde{X}^2B_{2g}$ band origin (19622 $\text{cm}^{-1} \approx 2.4$ eV) despite the fact that the energetic threshold for the process has been determined as 3.32 ± 0.18 eV, [81] around 0.9 eV above the $\tilde{B}^2B_{3u} \leftarrow \tilde{X}^2B_{2g}$ band origin.

The possibility that the $p\text{-DCB}^+$ cations absorb but a single photon and already possess sufficient internal energy to make up the deficit and take them above the fragmentation threshold is unlikely given that very sharp vibronic bands are observed in the lower energy part of the spectrum and because of the absence of vibrational hot bands. The most likely explanation is that the photofragmentation process involves the absorption of 2 photons from the same 10 ns laser pulse. Absorption of 2 photons from one laser pulse could occur in a sequential photo-absorption/internal conversion cycle illustrated in Figure 3-10.

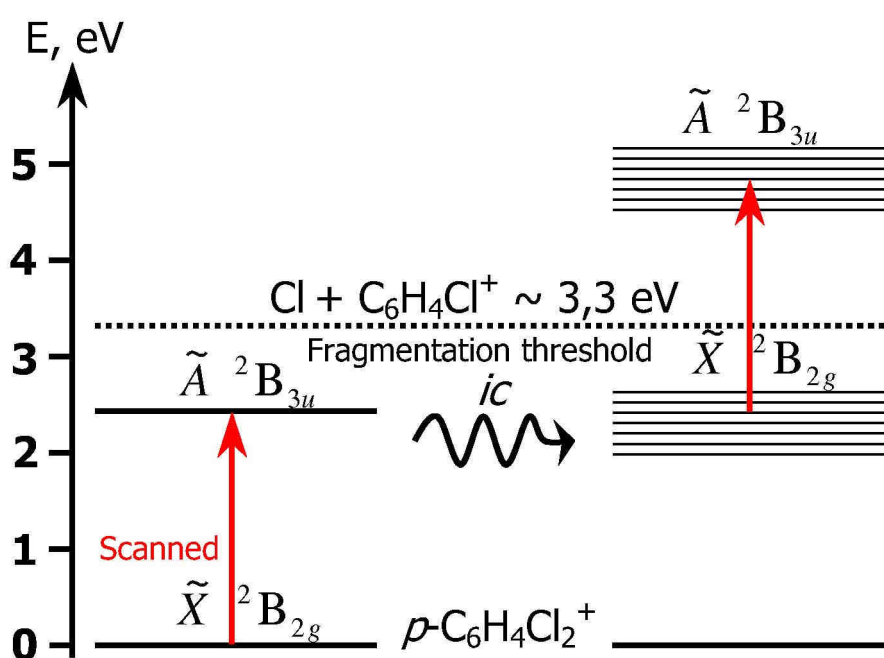


Figure 3-10 Scheme for a two photon dissociation of the $p\text{-DCB}^+$ radical cation via the $\tilde{B}^2B_{3u} \leftarrow \tilde{X}^2B_{2g}$ system. Each photon absorption is followed by rapid internal conversion to vibrationally excited levels of the \tilde{X}^2B_{2g} state. Absorption of 2 photons is sufficient to exceed the threshold for fragmentation into $\text{C}_6\text{H}_4\text{Cl}^+ + \text{Cl}$.

Resonant excitation of a $\tilde{B}^2B_{3u} \leftarrow \tilde{X}^2B_{2g}$ transition yields, through internal conversion, highly vibrationally excited \tilde{X}^2B_{2g} state ions which in turn absorb a second photon of the same frequency to produce vibrationally energized \tilde{B}^2B_{3u} state ions which then internally convert to produce \tilde{X}^2B_{2g} ions with ≈ 4.8 eV of vibrational energy. The second absorption step

would access \tilde{B}^2B_{3u} state levels with 2.4 eV of vibrational energy where the density of vibrational states is high. This sequential process seems feasible given that very rapid internal conversion from the $\tilde{B}^2B_{3u} 0^0$ level has been deduced from emission studies ($k_{ic} \approx 10^{11} \text{ s}^{-1}$). [20] Internal conversion for higher \tilde{B}^2B_{3u} vibronic levels is likely to be even more rapid. Based on the coincidence measurements, $\text{C}_6\text{H}_4\text{Cl}_2^+$ ions with $E_{vib} = 4.8 \text{ eV}$ would dissociate at rates of $10^4 - 10^5 \text{ s}^{-1}$ (*i.e.* on timescales $< 1 \text{ ms}$). [85]

It is interesting to note that the Ar matrix $\tilde{B}^2B_{3u} \leftarrow \tilde{X}^2B_{2g}$ absorption spectrum is dominated by the 0_0^0 band and the ν_6 progression, with the 6_0^n intensities dropping as n increases. While the 0_0^0 and 6_0^n bands also occur in the gas phase photodissociation spectrum, other transitions that might be expected to have much lower Franck-Condon factors, such as the 22_0^2 , 17_0^2 , and 8_0^2 bands, also appear with comparable intensities. Furthermore, the photodissociation spectrum becomes increasingly congested above 21000 cm^{-1} with sharp peaks protruding from a broad intense background. There are several possible causes for the intensity differences in the matrix and resonant 2 photon photodissociation spectra. The most important effect is probably saturation of the first $\tilde{B}^2B_{3u} \leftarrow \tilde{X}^2B_{2g}$ absorption step due to high laser powers so that the intensities of Franck-Condon weak transitions are boosted. Secondly, as the laser frequency is increased and higher vibronic levels are accessed in the \tilde{B}^2B_{3u} manifold in the first absorption step, the second photon absorption step will be to higher energies in the \tilde{B}^2B_{3u} manifold where the density of vibrational states is larger (see Figure 3-10). For this reason it is more likely that a second photon will be absorbed and that the molecules will dissociate yielding a detectable fragment signal. If this is the case, the consequence would be that the intensities of the higher frequency $\tilde{B}^2B_{3u} \leftarrow \tilde{X}^2B_{2g}$ vibronic bands would be enhanced relative to the lower ones.

The sharp, narrow bands observed for the $\tilde{B} \ ^2B_{3u} \leftarrow \tilde{X} \ ^2B_{2g}$ system in the current study can be contrasted with the broad features observed for the $\tilde{E} \leftarrow \tilde{X} \ ^2B_{2g}$ system of uncooled p -DCB⁺ radical cations in a RF ion trap over the 312 - 327 nm range. [86]

The spectrum obtained by monitoring C₆H₃⁺ photofragments showed a single broad feature (fwhm \approx 200 cm⁻¹), which corresponds to the $\tilde{E} \leftarrow \tilde{X} \ 0_0^0$ transition observed in the Ar matrix, superimposed on a broad background. The helium buffer gas cooling is presumably responsible for the far narrower vibronic bands (fwhm \approx 8 cm⁻¹) observed using our apparatus.

3.3 Two-photon two-colour photofragmentation spectroscopy.

3.3.1 Polyacetylene cations.

The origin bands observed for the $A \ ^2\Pi - X \ ^2\Pi$ electronic transitions of HC₄H⁺ through HC₁₆H⁺ are shown in Figure 3-11.

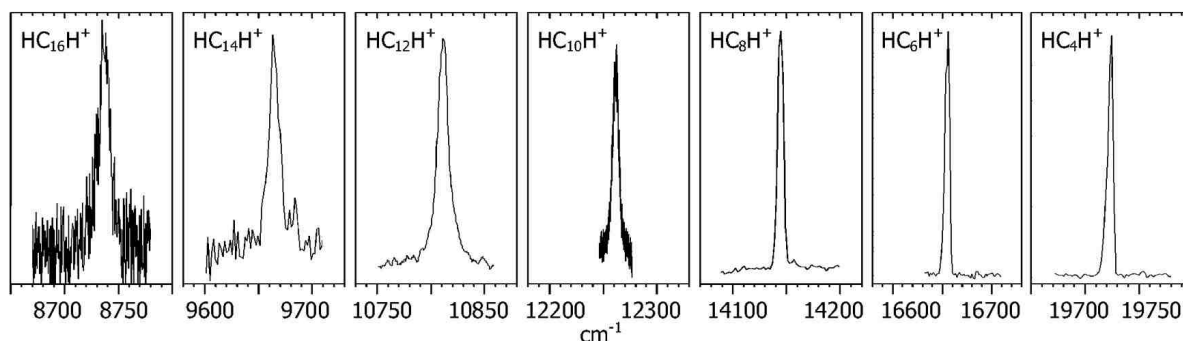


Figure 3-11 Gas phase origin bands observed for the $A \ ^2\Pi - X \ ^2\Pi$ transition of the HC_{2n}H⁺ species.

and are summarized in Table 12.

Table 12 Observed band maxima (nm) for the $A^2\Pi - X^2\Pi$ polyacetylene cation series in the gas phase, the estimated oscillator strengths f_{0-0} and inferred upper limits for the column densities N_{\max} in diffuse clouds.

Species	Transition	$\lambda_{\max, \text{air}}$	f_{0-0}	$N_{\max} / 10^{12} \text{ cm}^{-2}$
HC_4H^+	$A^2\Pi_u - X^2\Pi_g$	506.8	0.04 ^a	1
HC_6H^+	$A^2\Pi_g - X^2\Pi_u$	600.2	0.06 ^b	0.5
HC_8H^+	$A^2\Pi_u - X^2\Pi_g$	706.8	0.08 ^c	0.3
HC_{10}H^+	$A^2\Pi_g - X^2\Pi_u$	815.4	0.10 ^c	0.2
HC_{12}H^+	$A^2\Pi_u - X^2\Pi_g$	924.7	0.12 ^c	0.1
HC_{14}H^+	$A^2\Pi_g - X^2\Pi_u$	1034.6	0.14 ^c	
HC_{16}H^+	$A^2\Pi_u - X^2\Pi_g$	1144.0	0.16 ^c	

^a[87], ^b[53], ^cEstimated from trend (see text)

The bands are not rotationally resolved because the rotational constants vary from 0.15 cm^{-1} for HC_4H^+ to less than 0.01 cm^{-1} for species larger than HC_{10}H^+ . The best laser resolution obtained was 0.3 cm^{-1} . In addition lifetime broadening might occur as a result of intramolecular processes. A shift in the origin band to the red is observed as the number of carbon atoms in the chain increases (Figure 3-12). Also of note is that photostability and oscillator strength have been reported to increase with the number of carbon atoms as well. [38]

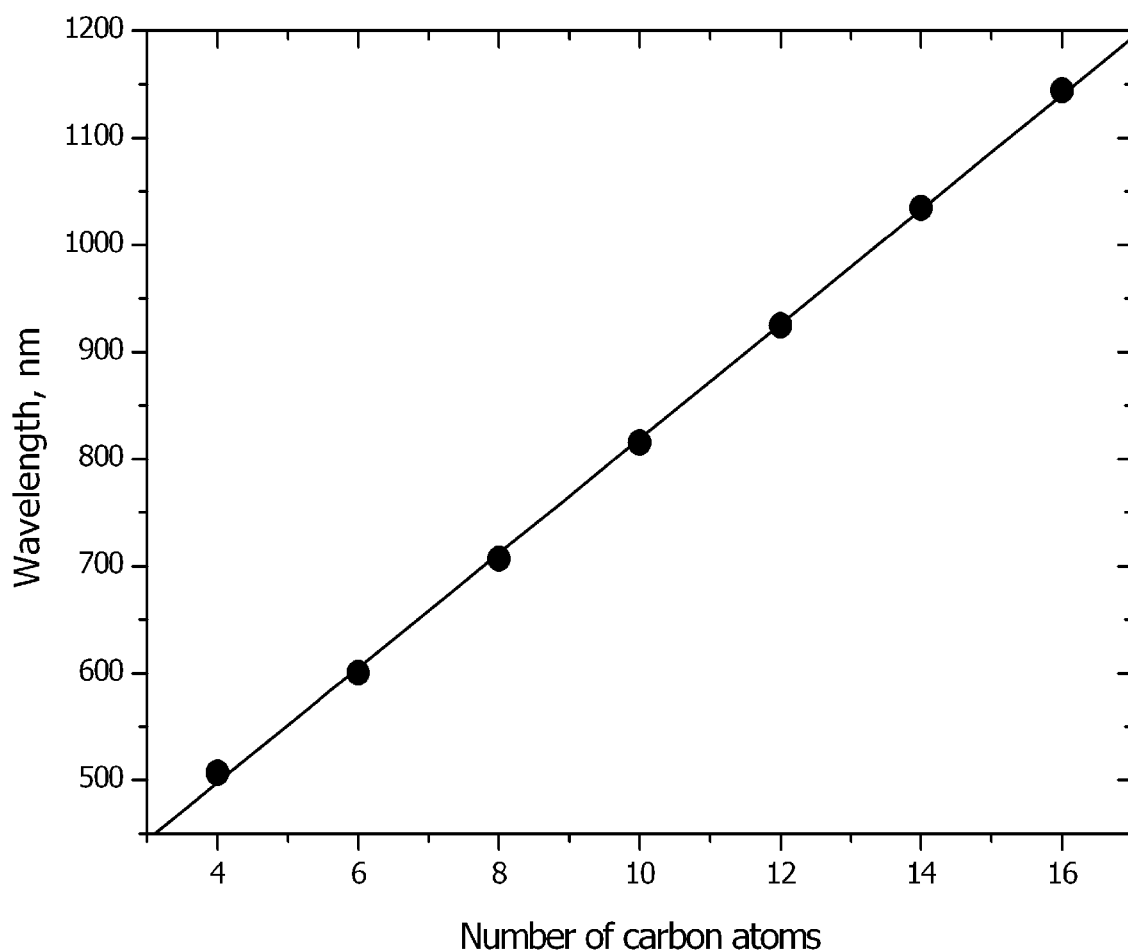


Figure 3-12 The linear relationship between the number of carbon atoms and the location of the origin band ($A^2\Pi - X^2\Pi$) in the gas phase for the polyacetylene cations $HC_{2n}H^+$.

Simulating the rotational profile of HC_6H^+ using spectroscopic constants taken from the literature [38] demonstrated that temperatures as low as 30 K were obtained (Figure 3-13). [88]

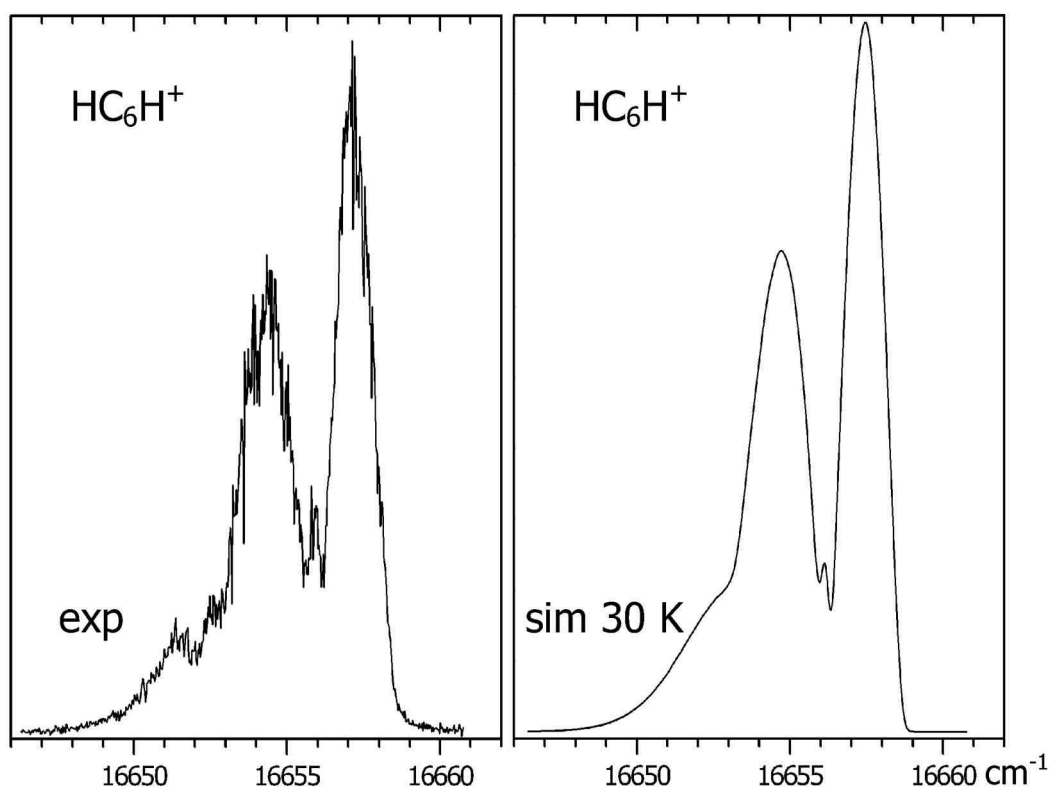


Figure 3-13 A simulation of the rotational profile for the $A \ ^2\Pi_g - X \ ^2\Pi_u$ transition of HC_6H^+ demonstrates that temperatures of 30 K were obtained in the ion trap.

Two spin orbit bands would be expected from a $A \ ^2\Pi - X \ ^2\Pi$ transition for the $^2\Pi_{3/2} - ^2\Pi_{3/2}$ and the $^2\Pi_{1/2} - ^2\Pi_{1/2}$ components. The intensity ratio of their two origin bands is determined by the temperature and the spin-orbit splitting in the ground state ($A'' \sim -33 \text{ cm}^{-1}$). [89] The separation between the two bands is determined by the difference in spin orbit constants in the excited and ground states ($\Delta A = A' - A'' \sim 2 \text{ cm}^{-1}$). In the spectra presented, however, only the $A \ ^2\Pi_{3/2} - X \ ^2\Pi_{3/2}$ transitions are observed due to the cold temperatures obtained through the collisional cooling process.

Previous studies have shown that for HC_4H^+ approximately 80% of the ions in the $v'=0$ level of the $A \ ^2\Pi_u$ state fluoresce, with minor channels losing energy through non-radiative processes. [53] The cited experiment measured fluorescent lifetimes of 71 ns, 17 ns, and <6 ns for the chain species HC_4H^+ , HC_6H^+ , and HC_8H^+ , respectively. The quantum yield, however, was found to decrease as the chain size lengthened, indicating that the non-radiative channel

of relaxation becomes more important as the size of the radical increases. Figure 3-14 shows agreement with such a result; the lifetimes of the excited ions held in the 22-pole ion trap were probed by delaying the length of time between the excitation and fragmentation laser pulses.

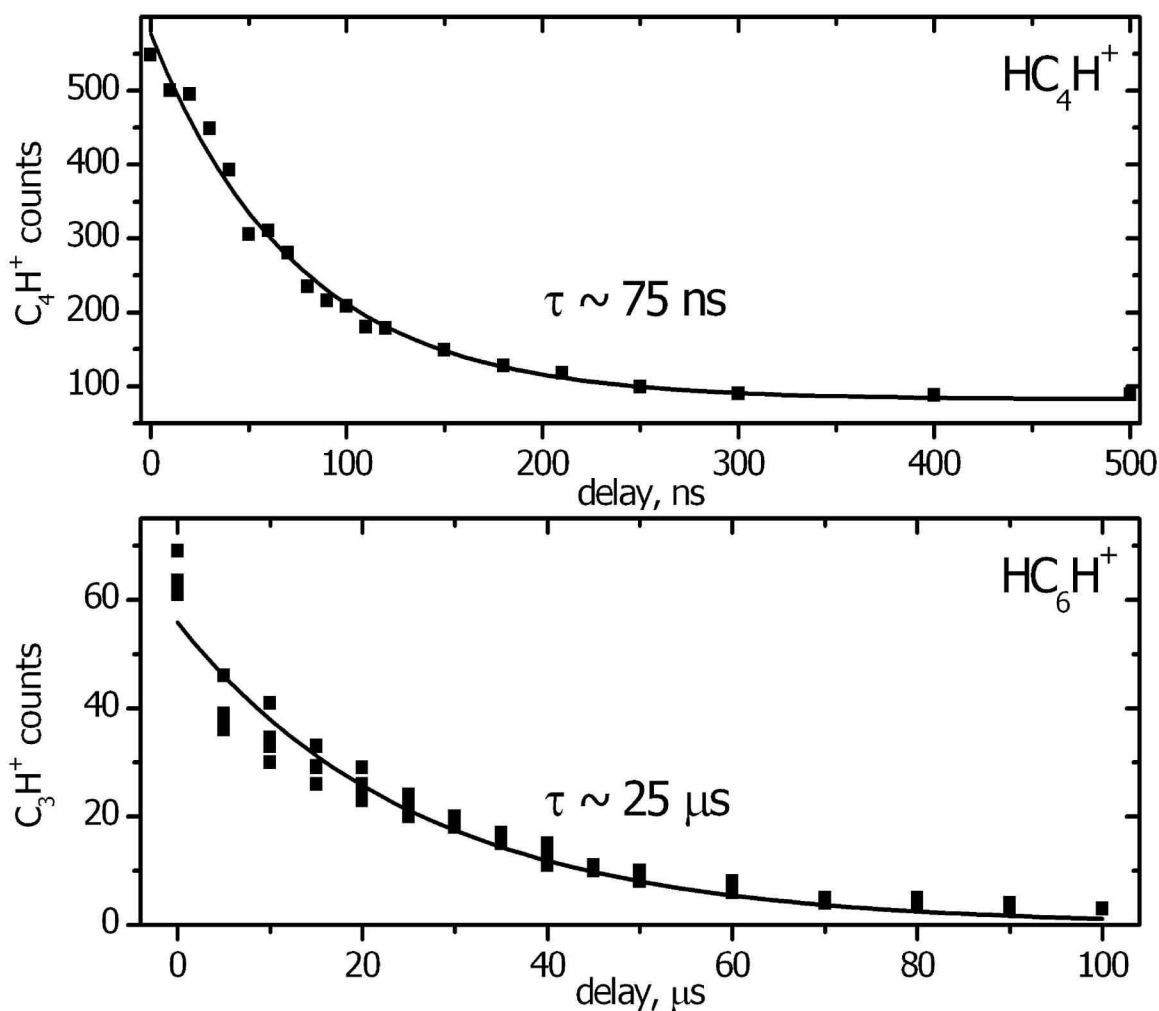


Figure 3-14 Cooling dynamics of HC_4H^+ and HC_6H^+ observed by varying the delay between pump (507 or 600 nm) and probe (210 or 248 nm) lasers while monitoring the intensity of the C_4H^+ or C_3H^+ fragment ions.

Diacetylene cation was found to have an excited lifetime on the order of 75 ns. Longer chains, on the other hand, demonstrated significantly longer lifetimes ($> \mu\text{s}$). As the number of carbon atoms in the polyacetylene cations increases the radiative decay channel becomes a more minor process.

These results are similar to the findings observed when examining the excited state lifetimes of the protonated polyacetylenes, HC_nH_2^+ of C_{2v} symmetry, in the same ion trap. [54]

For the $n=6,8$ species it was concluded that an internal conversion process occurred on a sub-ns time scale; whether the excited ions crossed into a lower lying triplet state or into the ground state's highly excited vibrational manifold could not be determined. TD-DFT calculations indicated that more than a few triplet states were accessible through an intersystem crossing from the B^1A_1 singlet state that was being probed. In the case of the polyacetylene cations the spin forbidden quartet states, $^4\Pi_u$ and $^4\Pi_g$, lie higher in energy in the linear geometry than the doublet states that are accessed in this experiment. [89] Calculations for HC_4H^+ and HC_6H^+ , however, show that the quartet states drop closer toward the vicinity of the doublet states as the molecules bend. Therefore the quartet states could also play a role in the dynamics observed, similar to the triplet states for the protonated polyacetylene species. The long lifetimes observed in the trap may thus be attributed to a population of molecules in either the ground state's highly excited vibrational levels or in the close lying quartet states. Excited radicals lose their internal energy through collisions with the cooled helium buffer gas, resulting in a vibrational to translational energy transfer which gradually cools the ions. Given the background pressure of the buffer gas (approximately 4×10^{-4} mbar) and the size of the cold ion trap, an estimated 1 collision per μs occurs between the excited polyacetylene cation species and the helium gas.

3.3.2 Protonated polyacetylene cations.

The spectra were recorded for the regions where the respective transitions were first observed in neon matrices after mass selected deposition. [63] 345 nm and 248 nm UV laser light was chosen as the probe wavelength for $HC_8H_2^+$ and $HC_6H_2^+$ respectively. Loss of both C_3H_2 and C_3H was monitored as the fragmentation channels for both $HC_8H_2^+$ and $HC_6H_2^+$ cations.

The electronic absorption spectrum of $HC_8H_2^+$, observed by measuring the fragment ion C_5H^+ , is shown in Figure 3-15.

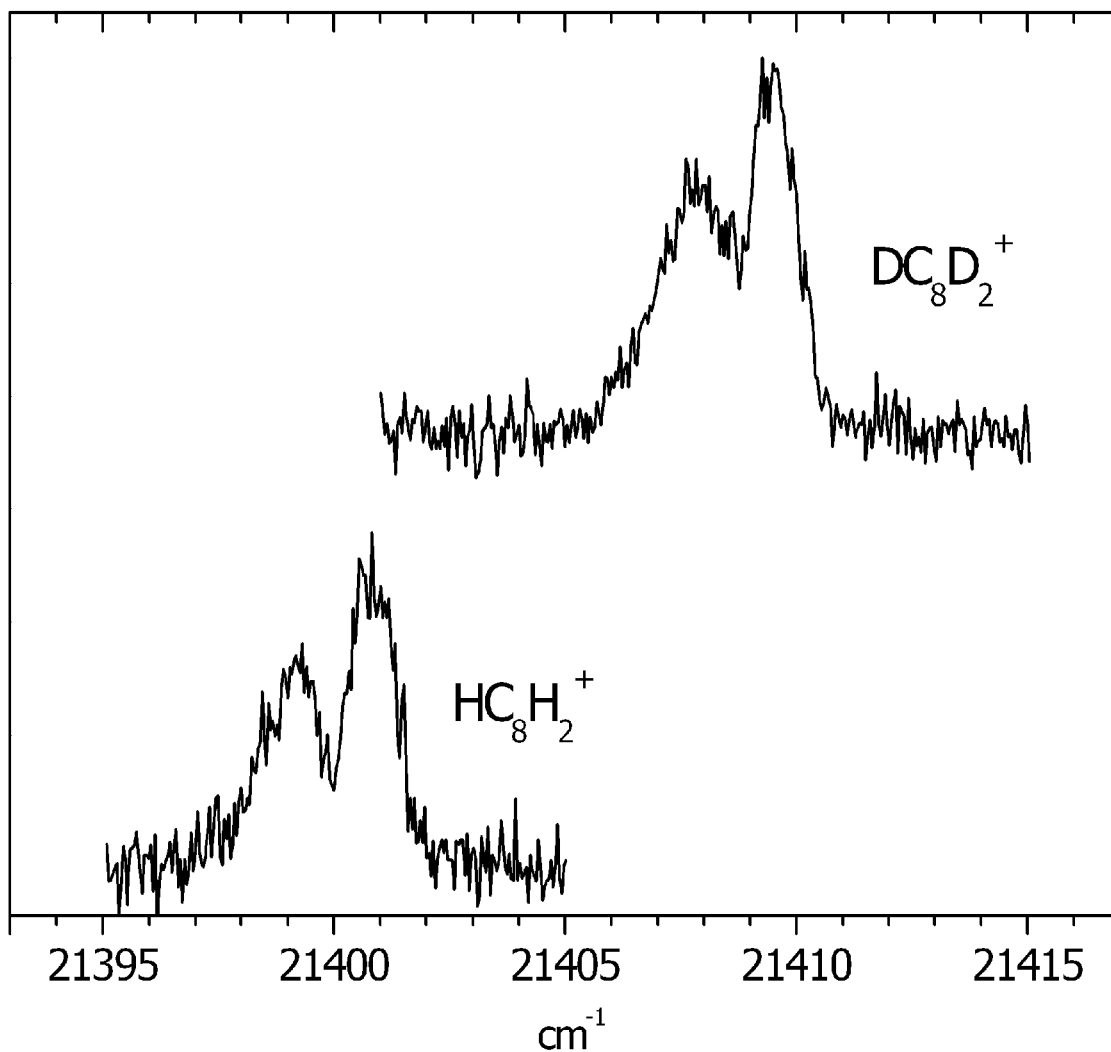


Figure 3-15 The origin band in the $B^1A_1 \leftarrow X^1A_1$ electronic transition for $HC_8H_2^+$ and $DC_8D_2^+$ recorded via a two-photon two-colour photofragmentation process by monitoring the C_5H^+ or C_5D^+ fragment ions produced.

The transition appears in the gas phase around $21,400\text{ cm}^{-1}$; a 14 cm^{-1} blue shift from the neon matrix value. [63] This result is consistent with the polyacetylene cation series in which gas to Ne matrix shifts amounted to no greater than one percent of the transition's frequency. [38] The corresponding transition for the deuterated species, $DC_8D_2^+$, is also shown in Figure 3-15. The deuterated species has a blue shift (8 cm^{-1}) with respect to $HC_8H_2^+$ and displays a similar rotational profile. Figure 3-16 shows the same $HC_8H_2^+$ transition in higher detail.

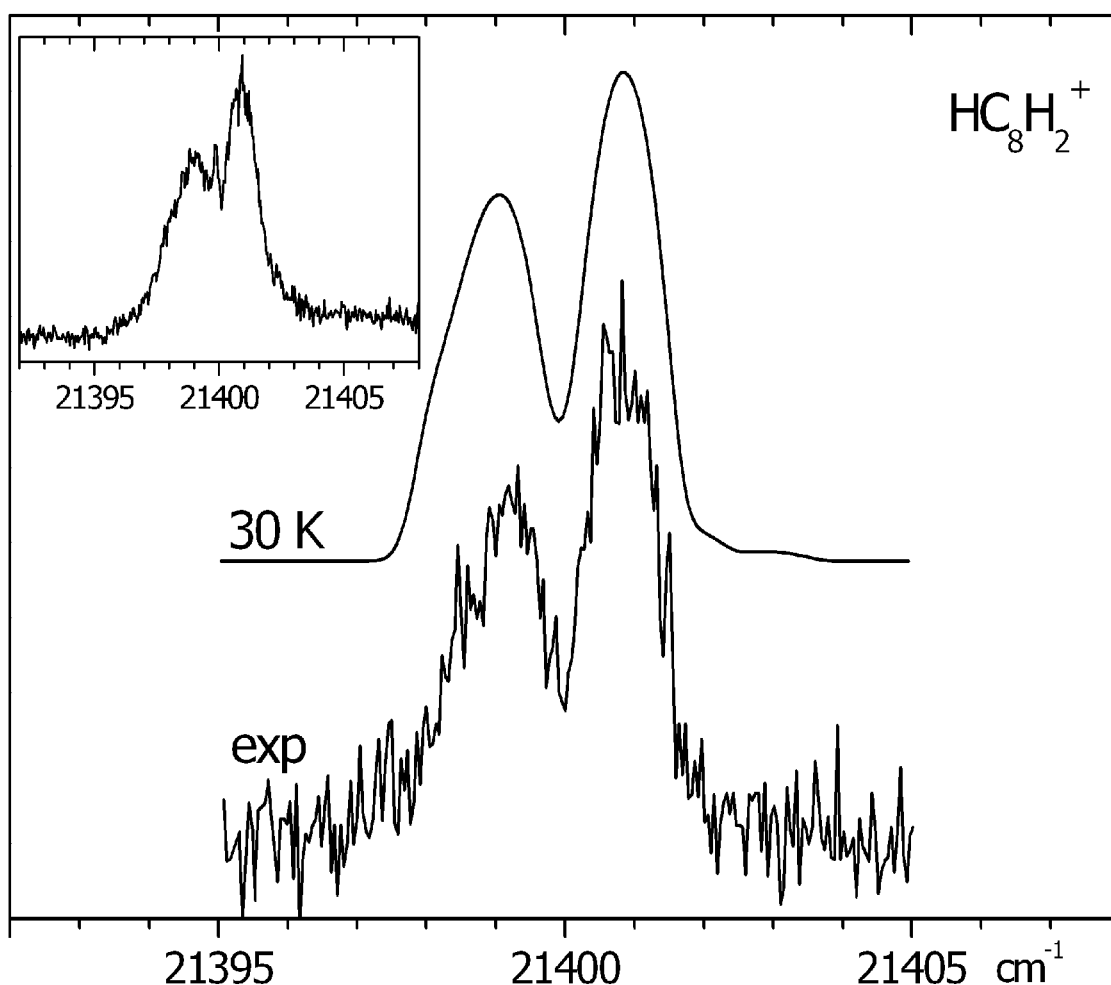


Figure 3-16 The origin band in the $B^1A_1 \leftarrow X^1A_1$ electronic transition for the HC_8H_2^+ cation, recorded via a two-photon two-colour photofragmentation process by monitoring the C_5H^+ fragment ions produced. Above the spectrum lies the simulated fit and an inset demonstrates the effects of saturating the transition (see text).

The band is not rotationally resolved because the rotational constant for HC_8H_2^+ is on the order of 0.02 cm^{-1} (*vide infra*) and the bandwidth of the OPO laser was 0.3 cm^{-1} . It is possible, however, to interpret the band in terms of unresolved P and R branch contours. The width of the peak is about 4 cm^{-1} . Saturation effects were observed upon increasing power of the scanned laser. Specifically, P and R branches were broadened and a visible Q branch became more apparent, as shown in the inset of Figure 3-16. Figure 3-17 shows the similar electronic transition for HC_6H_2^+ , observed by monitoring the fragment ion C_3H^+ .

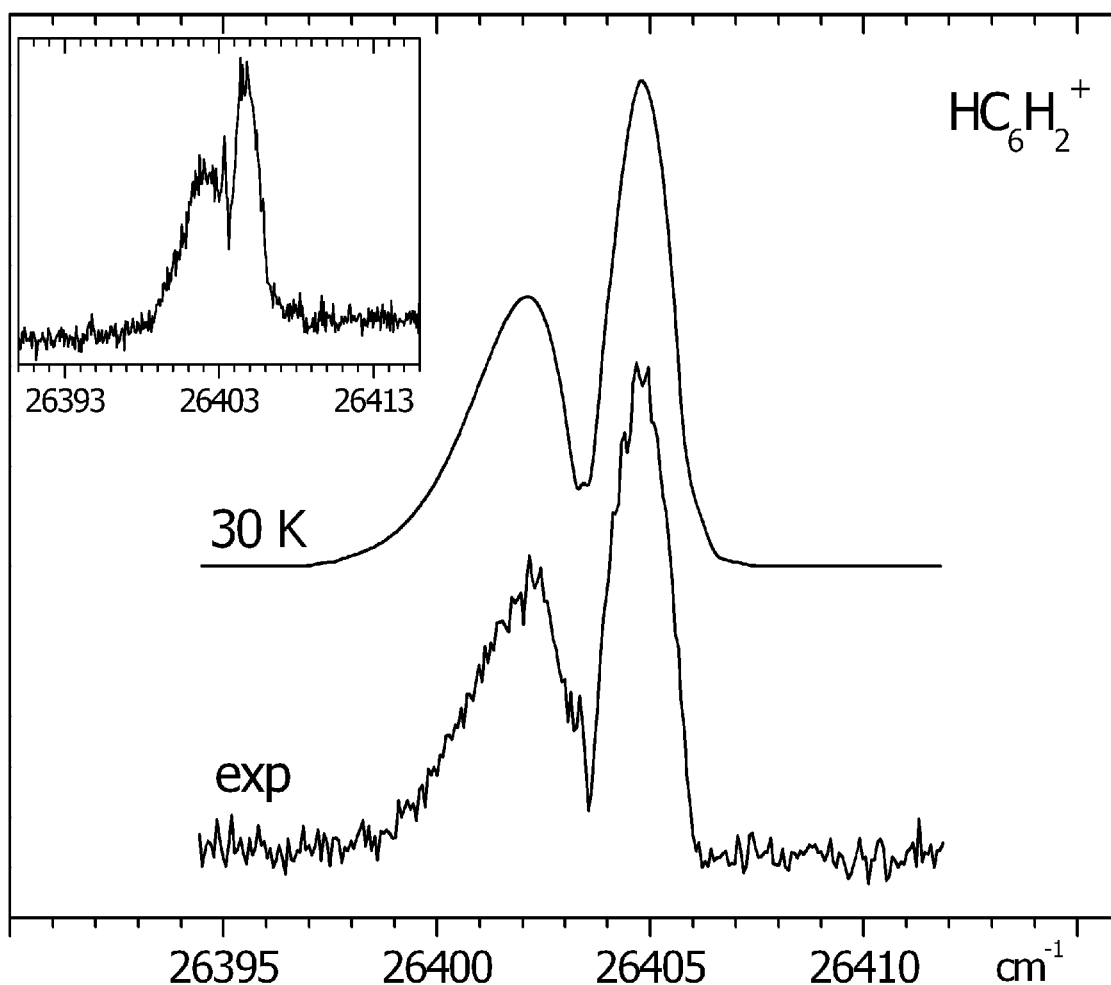


Figure 3-17 The origin band in the $B^1A_1 \leftarrow X^1A_1$ electronic transition for the HC_6H_2^+ cation, recorded via a two-photon two-colour photofragmentation process by monitoring the C_3H^+ fragment ions produced. Above the spectrum lies the simulated fit and an inset demonstrates the effects of saturating the transition (see text).

The transition occurs near $26,404 \text{ cm}^{-1}$ in the gas phase, 10 cm^{-1} red shifted with respect to the same transition observed in Ne matrices. The unresolved rotational profile has a width of 6 cm^{-1} . The rotational constant for HC_6H_2^+ is on the order of 0.04 cm^{-1} and the laser resolution obtained without the use of an internal etalon was 0.15 cm^{-1} . An inset in Figure 3-17 demonstrates the effects of increasing the laser power: saturation leads to a broadened profile and an increase in the relative intensity of the Q-branch.

There are a number of possible structures for the $\text{HC}_{2n}\text{H}_2^+$ species. Previous analysis from the IR spectra of the mass-selected HC_nH_2^+ ($n = 4, 6, 8$) ions in a neon matrix [63] concluded that the linear protonated form is preferred by the presence of C-H stretches in the CH_2 group and totally symmetric C-C stretches along the carbon skeleton. Calculations can give insight

into the geometries of the studied species as well. These have shown that a linear C_{2v} structure is the most stable isomer for the $HC_4H_2^+$ species; [60] it can be argued that the interactions of the π -type orbitals on all four carbon atoms inevitably form the linear carbon backbone. On this basis one might expect that collisional relaxation of the larger chain species ($HC_6H_2^+$ and $HC_8H_2^+$) will likely result in linear C_{2v} structures as well. To confirm this assumption calculations on the ground state of both $HC_6H_2^+$ and $HC_8H_2^+$ have been performed using the B3LYP functional. [90, 91] A DFT B3LYP/cc-pVTZ level calculation verified a C_{2v} symmetry for these larger chains and revealed a 1A_1 electronic ground state for both species (Figure 3-18).

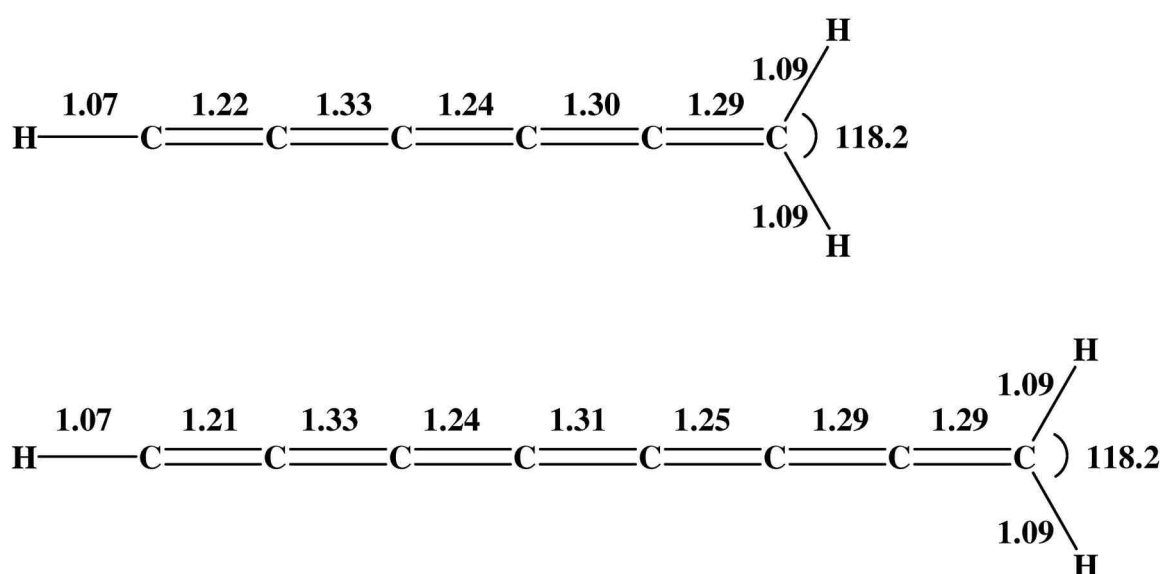


Figure 3-18 Calculated structures of the ground state $HC_6H_2^+$ and $HC_8H_2^+$ using the DFT B3LYP/cc-pVTZ level of theory.

Table 13 . Inferred ground ($X \ ^1A_1$) and excited ($B \ ^1A_1$) state rotational constants. (Constant B refers to $1/2(B + C)$).

	$HC_6H_2^+$	$HC_8H_2^+$
T_0 / cm^{-1}	26,404.0 ^a	21,399.8 ^a
B'' / cm^{-1}	0.0433 ^b	0.0187 ^b
B' / cm^{-1}	0.0426 ^a	0.0186 ^a
B'' / B'	1.01	1.13
A'' / cm^{-1}	9.585 ^b	9.612 ^b

A' / cm^{-1}	9.8 ^a	9.8 ^a
^a Via TSF procedure		
^b From DFT geometry calculated at the B3LYP/cc-pVTZ level		

The DFT calculation also yields the ground state rotational constants (Table 14). Because the electronic transitions in Figures 3-15, 3-16, 3-17 are not rotationally resolved it is necessary to rely on calculations to obtain information concerning the spectroscopic properties of the excited states. Thus a TD-DFT calculation, also at the DFT B3LYP/cc-pVTZ level of theory, was carried out for the three lowest lying electronic transitions (Table 14).

Table 14 Calculated vertical excitation energies (eV) and oscillator strengths.

Species	State	TD-DFT (cc-pVTZ)	f	CIS (cc-pVDZ)	f	Experiment
HC ₆ H ₂ ⁺	¹ A ₂	1.55	0.00	1.79	0.00	3.27 eV
	¹ A ₁	3.44	0.01	3.91	0.03	
	¹ A ₂	3.82	0.00	4.13	0.00	
HC ₈ H ₂ ⁺	¹ A ₂	1.25	0.00	1.66	0.00	2.60 eV
	¹ A ₁	2.75	0.01	3.36	0.07	
	¹ A ₂	3.15	0.00	3.57	0.00	

This predicts that only a vertical transition to the second excited electronic state is dipole allowed. Therefore the origin band observed in the spectrum can be assigned as $B \ ^1A_1 \leftarrow X \ ^1A_1$, a parallel a-type transition.

While the TD-DFT calculations can determine the symmetry of the excited state, a more comprehensive calculation can verify if the transition actually populates a bound state. Both a HF and a CIS calculation on the ground and excited states for both species were performed using the cc-pVDZ basis set. The results, also shown in Table 14, indeed indicate convergences to excited state geometries that demonstrate the same symmetries as the TD-DFT

calculation. Thus both methods are able to confirm a parallel transition, which is in accord with the absence of K-structure expected for perpendicular bands in the observed spectrum.

As the rotational structure is unresolved a least squares procedure called “total spectrum fitting” (TSF) was used to obtain the molecular constants. [92] The spectrum of an asymmetric top molecule is characterized by the rotational constants A , B , and C in both the ground and excited states, the transition frequency, temperature, spin statistical weights, a FWHM of Gaussian line shape, and an amplitude and base line bias. This can yield spectroscopic constants for the excited upper state. The ground state rotational constants A'' , B'' , and C'' were fixed using the results from the DFT calculation at the B3LYP/cc-pVTZ level, the transition frequency was taken from the experimental spectrum, and the temperature was modeled at 30 K. The simulations are shown in Figures 3-16, 3-17, and the results of the fitting procedure are tabulated in Table 13. In general the A' constants could be varied significantly ($\pm 0.1 \text{ cm}^{-1}$) and still give reasonable profile fits which qualitatively match the experimental spectra. This variation also introduced large errors in both the A' constants and ΔA , as well as in T_0 . For both of these species a proper analysis awaits the measurement of a rotationally resolved spectrum.

From both the calculations and the experiments one can conclude that the ions undergo a minimal change in geometry during the $B^1A_1 \leftarrow X^1A_1$ electronic transition from the ground state to the second excited state: specifically, ΔA changes by no more than 2 % for HC_6H_2^+ and HC_8H_2^+ , indicating that the hydrogen atoms occupy a similar geometry and the bond angles are comparable in the two states. Also, for both ions the ratio of B''/B' is close to unity, as would be expected for a long chain in which only a minor change in molecular geometry takes place during the electronic excitation.

Scanning to the blue of the origin band of HC_8H_2^+ at 467.25 nm revealed the presence of a vibrational band in the excited state. Located at 457.2 nm, this band matches well with the

matrix band observed at 457.5 nm: a 472 cm^{-1} C-C stretch. Other vibrational bands were not sought.

In order to understand how the two-photon process proceeds the deactivation of the protonated species in the bound excited electronic state was studied by varying the time delay between the scanned and fixed fragmentation lasers. From this time dependence (Figure 3-19) one can speculate about the dynamics occurring in the ion trap.

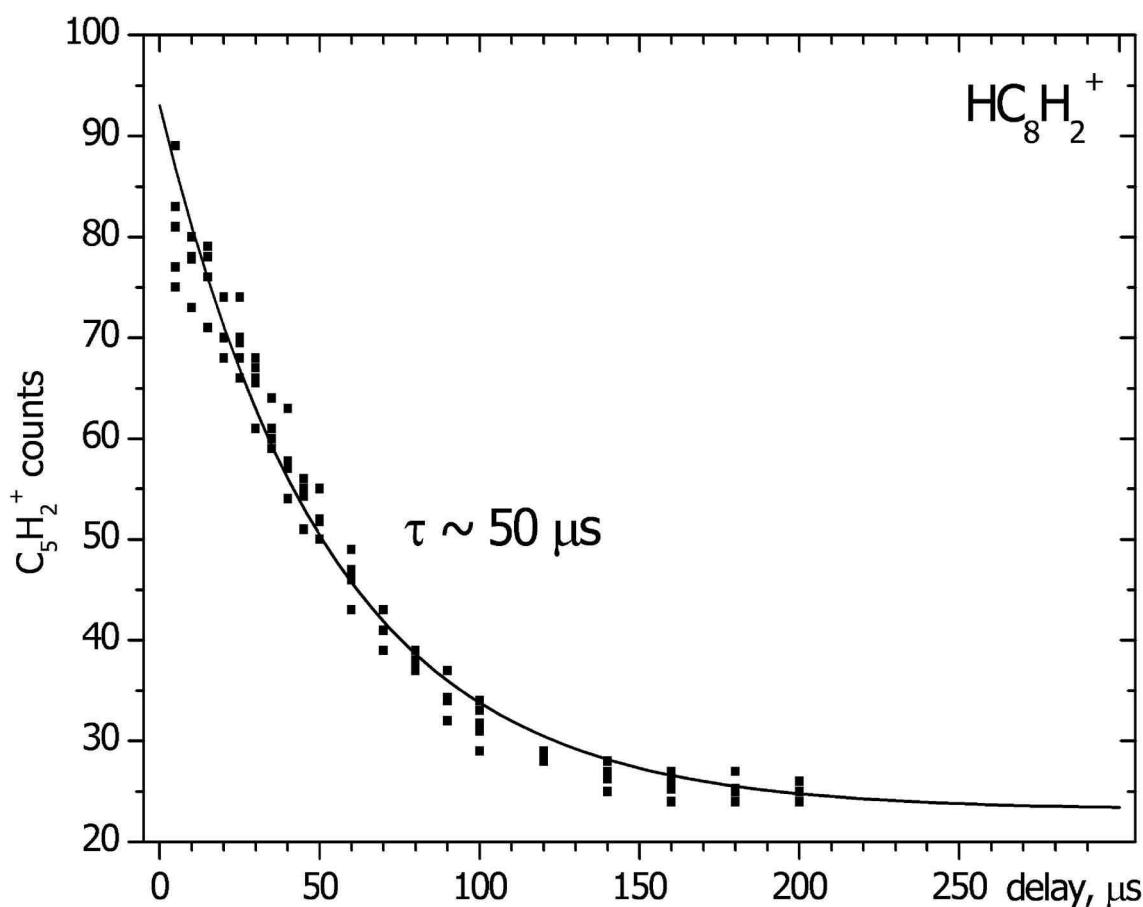


Figure 3-19 Cooling dynamics of excited HC_8H_2^+ , observed by varying the delay between the 467.30 nm pump and 248 nm probe lasers while monitoring the intensity of the C_5H_2^+ fragment ions.

A search for the $\text{HC}_8\text{H}_2^+ B^1\text{A}_1 \leftarrow X^1\text{A}_1$ origin band using a laser induced fluorescence spectrometer revealed no detectable signal, thus demonstrating that there must be a fast depopulation of the excited state to the ground state on a subnanosecond time scale. The measured time constant from the decay trace shown in Figure 3-19, however, lies in the μs

time regime is thus related to subsequent collisional deactivation: given the background pressure of the buffer gas ($\approx 4 \times 10^{-4}$ mbar) and the size of the cold trap, an estimated 1 collision per μs occurs between the excited protonated polyacetylene species and the helium gas, resulting in a vibrational to translational energy transfer which gradually cools the hot ions. Figure 3-20 depicts the observed scenario: a conversion process depopulates the B^1A_1 excited state faster than the radiative decay to X^1A_1 , leading to a long lived excited population in either the ground state or a triplet manifold.

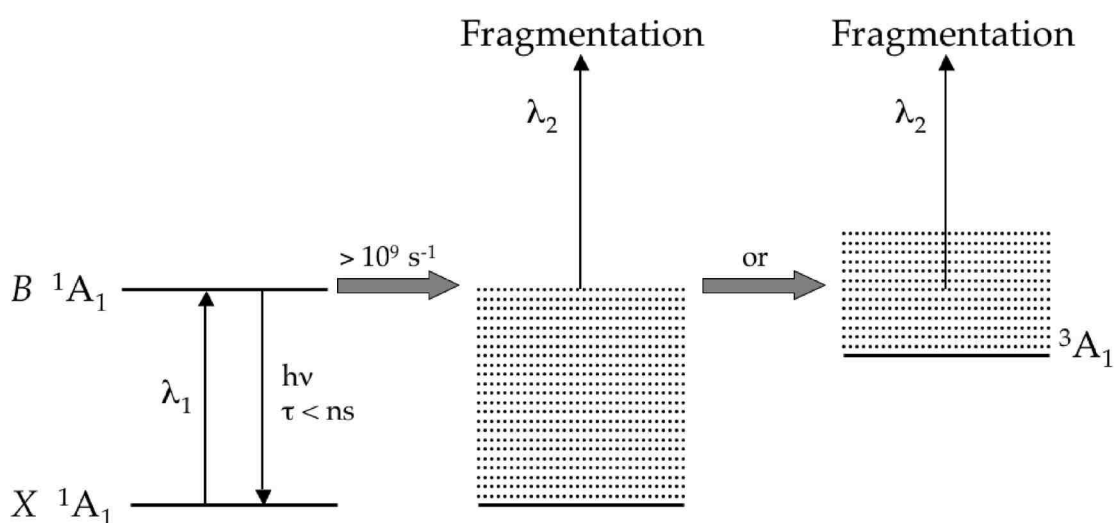


Figure 3-20 Lack of fluorescence indicates that the excited electronic state B^1A_1 obtained using λ_1 is short lived ($< \text{ns}$), thus decaying through an intermolecular process. A longer lived state, which exists either as a highly excited vibrational X^1A_1 or a triplet manifold (e.g. 3A_1), is subsequently depopulated through collisions with the helium buffer gas.

The second UV photon in the experiment then fragments the ions found in either of these longer lived energy levels. Whether the excited ions cross into a lower lying triplet state or are internally converted into the ground state's highly excited vibrational manifold is not certain.

The DFT theory predicts an electron configuration of $(2b_2)^2(2b_1)^2(3b_2)^2(3b_1)^2$ for the four highest occupied molecular orbitals of HC_6H_2^+ , leaving the $(4b_2)^0(4b_1)^0(5b_2)^0(5b_1)^0$ orbitals open for excitation (HC_8H_2^+ , by analogy, should have a similar electron configuration). For comparison, a previous DFT calculation on HC_4H_2^+ places the lowest lying triplet state

approximately 1.4 eV higher in energy than the singlet ground state, with the only difference in geometry being a slightly lengthened H₂C-C bond in the triplet state. [60] However, the lowest lying triplet state for HC₆H₂⁺, as predicted using a simple TD-DFT calculation, is a ³A₂ state with an electron configuration of (2b₂)²(2b₁)²(3b₂)²(3b₁)¹(4b₂)¹, thus rendering an intersystem crossing from the excited ¹A₁ manifold to this triplet state doubly forbidden. According to the TD-DFT calculations, at least two to three triplet states of ³A₁ and ³A₂ symmetry lie between *B* ¹A₁ and *X* ¹A₁ for both HC₆H₂⁺ and HC₈H₂⁺ (HC₈H₂⁺: ³A₂ (0.8 eV), ³A₂ (1.8 eV), ³A₂ (2.1 eV), ³A₁ (2.8 eV), HC₆H₂⁺: ³A₂ (1.0 eV), ³A₂ (2.3 eV), ³A₂ (2.6 eV), ³A₁ (3.4 eV)). This leaves open the possibility that one of these triplet states is absorbing the UV photon leading to fragmentation.

Chapter 4 Conclusions.

The apparatus was developed to study the electronic spectra of large organic ions, which may be of astronomical relevance. In order to obtain and compare the laboratory electronic absorption spectra with interstellar absorptions, the internal degrees of the ions have to be cooled to temperatures appropriate to interstellar space, 20 - 100 K. This has been achieved as the recorded electronic spectra of N_2O^+ and $p\text{-DCB}^+$ demonstrate. In the case of N_2O^+ , the rotational temperature achieved is 25 K and for $p\text{-DCB}^+$ the narrowness of the vibronic bands and the absence of hot bands shows that the vibrational degrees of freedom have been cooled to comparable temperatures. The resulting absorption spectrum of $p\text{-DCB}^+$, rich in vibronic structure, can be assigned to numerous modes in the excited state and their frequencies are inferred. The photofragment spectrum is a result of absorption of two photons in a process involving sequential internal conversion.

The analysis of the rotational K-structure resolved on the origin band of the $\tilde{A} \ ^2E_u \leftarrow \tilde{X} \ ^2E_g$ transition of 2,4-hexadiyne cation, and the absence of sequence vibrational bands, indicate that the approach developed to study the electronic spectra of larger polyatomic cations which have been collisionally relaxed to temperatures relevant to the interstellar medium is successful. In the present case the vibrational and rotational degrees of freedom are equilibrated to 20-30 K. The system studied here was selected because one photon transitions were known to lead to fragmentation from the excited electronic state and the K-structure was resolvable. The richness of the vibronic spectrum is obtained by saturating the weak transitions and thus may be used to deduce vibrational frequencies in the excited electronic state in larger, cold ions.

The gas phase $A \ ^2\Pi - X \ ^2\Pi$ origin bands of seven different polyacetylene cation chains have been recorded, with HC_{12}H^+ , HC_{14}H^+ , and HC_{16}H^+ presented for the first time.

A two-colour two-photon pump-probe experiment was used to dissociate the polyatomic species in a 22-pole ion trap, which led to efficient cooling of the studied species through collisional relaxation with cryogenically cooled helium. This allows a comparison of laboratory collected spectra to astrophysical observations. In this series the data for HC_4H^+ through HC_8H^+ were previously compared to the diffuse interstellar bands (DIB) literature and revealed no distinct matches. [5] A consultation of similar references [4, 93-96] also yields no corresponding features for HC_{10}H^+ . In the case of HC_{12}H^+ , HC_{14}H^+ , and HC_{16}H^+ the comparison is difficult due to the fact that there are few detectable DIBs reported longward of 800 nm. A recent study compiled DIB data up to 963 nm; [93] however no matches corresponding to the origin band of HC_{12}H^+ were found.

An upper limit to the column density for this series can be estimated from $N_{\text{max}} (\text{cm}^{-2}) = \frac{1.13 \times 10^{20} W_{\text{max}}}{\lambda^2 f}$, where f is the oscillator strength of the electronic transition and W_{max} represents the equivalent width. Experimental oscillator strengths have been reported for HC_4H^+ and HC_6H^+ (Table 1). [53, 87] Extrapolating this trend for longer chains yields $f_{0-0} = 0.08$, $f_{0-0} = 0.10$, and $f_{0-0} = 0.12$ for HC_8H^+ , HC_{10}H^+ , and HC_{12}H^+ . [5, 97] Using estimated equivalent widths $W_{\text{max}} = 10 \text{ m}\text{\AA}$ as the sensitivity limit for DIB detection in the visible region gives the upper limit column densities shown in Table 12.

The gas phase electronic spectra of two protonated polyacetylene chains have been reported for the first time. A two-colour two-photon pump-probe experiment was used to dissociate the polyatomic species in a 22-pole ion trap, which allowed efficient cooling of the studied species through collisional relaxation with cryogenically cooled helium. This enables a comparison of laboratory collected spectra to astrophysical observations.

The observed origin band (467.3 nm) in the electronic spectrum of HC_8H_2^+ does not correspond with any known feature listed in the diffuse interstellar bands (DIB) literature. [95, 96] In the case of HC_6H_2^+ , the origin band at 378.7 lies in a region where there are no detectable DIBs, with the exception of some shallow broad absorptions. [4] An upper limit to the column

density of HC_8H_2^+ can be estimated from $N_{\text{max}}(\text{cm}^{-2}) = \frac{1.13 \times 10^{20} W_{\text{max}}}{\lambda^2 f}$. Here, a calculated oscillator strength f (0.03) is taken from the TD-DFT calculation and an equivalent width, W_{max} , of 10 mÅ is assumed as the sensitivity limit for DIB detection in the visible region based on the weakest detectable features usually observed. [95] As a result an upper limit for the column density of HC_8H_2^+ in diffuse clouds is on the order of 10^{12} cm^{-2} .

The absence of rotational structure makes a clear cut assignment of the geometry difficult. Calculations and spectra from mass selected species trapped in neon matrices show that the protonated form, HC_nH_2^+ of C_{2v} symmetry, is the structure observed. Through modeling the band profile in the measured gas phase spectra both upper and lower state spectroscopic constants were determined. The measurement of rotationally resolved spectra will be able to confirm these proposed C_{2v} structures.

Chapter 5 Outlook.

The experiments have proven that the apparatus, based on a 22-pole trap, is capable of cooling the vibrational and rotational degrees of freedom of large cations to temperatures relevant for the ISM. In order to improve performance, further modifications are suggested and outlined below.

Reorienting the ion source could improve the operation by reducing background pressure. The position of the current source causes some difficulties: because it creates a relatively high background pressure in mass the spectrometer's chamber. In order to prevent sparking in the quadrupoles the background pressure must be reduced.

The current experimental setup also allows neutrals enter the mass spectrometer, which can be then ionized or fragmented by UV laser light, resulting in a noticeable background, that can hide weaker spectral features. Finally, having the main axis of the whole apparatus free from the ion source will make laser alignment easier. To circumvent all these difficulties one should install the ion source perpendicular with respect to the main axis of the apparatus (Figure 5-1)

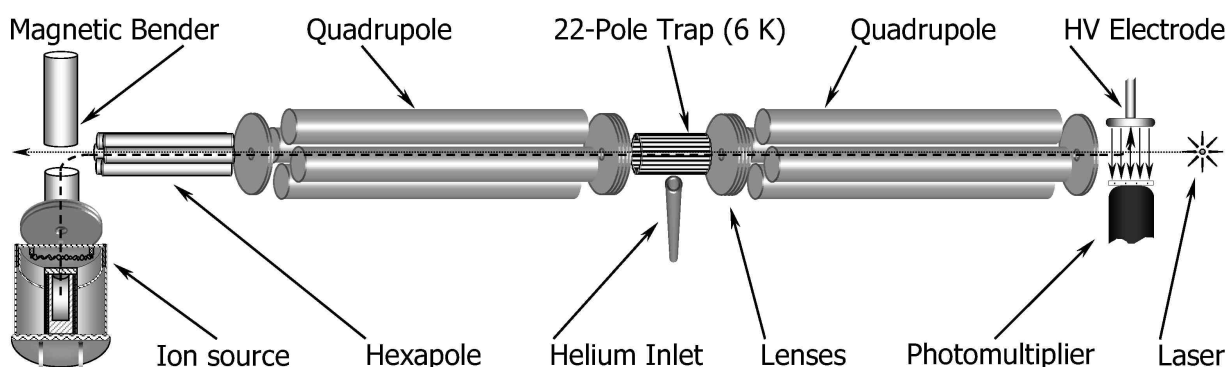


Figure 5-1 Simplified sketch of the modified apparatus.

As can be seen in the figure, ions generated in the source are then bent by 90 degrees through a magnetic field. The magnetic bender is followed by a hexapole, which guides the ions into the first quadrupole mass spectrometer. With such a configuration most of the neutrals will end up in the turbopump of the source chamber, allowing only charged particles to enter the rest of the apparatus. By filling the hexapole with room temperature helium buffer gas the ion's velocities can be equilibrated, resulting in a better mass resolutions.

The second proposed improvement is to install a piezzo-electric valve. Currently helium buffer gas enters the 22-pole trap by continuous flow. On one hand, this allows one to measure the cooling rate of an ion's excited electronic state through collision with cryogenically cooled helium. However, the presence of helium gas also limits the measurement of the real lifetime of the excited state. To do this one must eliminate all helium just before the laser excitation. In order to be able to do this it would be nice to fill the trap with helium for only a short amount of time.

The piezzo valve can easily generate very short ($\sim 10 \mu\text{s}$) and intense gas pulses. This will create a high number of helium atoms in the trap for a short time. At 5 K high concentration of helium gas will create ion-helium complexes between the large ions and helium through three body collisions. As a result, absorption of one resonant photon will lead to a rapid dissociation of these complexes. An absorption spectrum of the large ions can thus be measured by recording the number of these ionic complexes versus the wavelength of tunable laser radiation.

BIBLIOGRAPHY.

1. Douglas, A.E., *Origin of diffuse interstellar lines*. Nature, 1977. **269**(5624): p. 130-132.
2. Maier, J.P., *Electronic spectroscopy of carbon chains*. Journal of Physical Chemistry A, 1998. **102**(20): p. 3462-3469.
3. Fulara, J., Shnitko, I., Batalov, A., Maier J.P., *Electronic absorption spectra of linear and cyclic C_n^+ $n=7-9$ in a neon matrix*. Journal of Chemical Physics, 2005. **123**(4): p. 044305 1-6.
4. Herbig, G.H., *The diffuse interstellar bands*. Annual Review of Astronomy & Astrophysics, 1995. **33**: p. 19-73.
5. Motylewski, T., Linnartz, H., Vaizert, O., Maier, J.P., Galazutdinov, G.A., Musaev, F.A., Krelowski, J., Walker, G.A.H., Bohlender, D.A., *Gas-phase electronic spectra of carbon-chain radicals compared with diffuse interstellar band observations*. Astrophysical Journal, 2000. **531**(1): p. 312-320.
6. Maier, J.P., Walker, G.A.H., Bohlender, D.A., *Limits to interstellar C_4 and C_5 toward ζ ophiuchi*. Astrophysical Journal, 2002. **566**(1): p. 332-335.
7. Ding, H., Pino, T., Güthe, F., Maier, J.P., *Gas phase electronic spectrum of C_3H in the visible*. Journal of Chemical Physics, 2001. **115**(15): p. 6913-6919.
8. Lucas, R., Liszt, H.S., *Comparative chemistry of diffuse clouds. I. C_2H and C_3H_2* . Astronomy & Astrophysics, 2000. **358**(3): p. 1069-1076.
9. Maier, J.P., Walker, G.A.H., Bohlender, D.A., *On the possible role of carbon chains as carriers of diffuse interstellar bands*. Astrophysical Journal, 2004. **602**(1): p. 286-290.

10. Maier, J.P., Lakin, N.M., Walker, G.A.H., Bohlender, D.A., *Detection of C₃ in diffuse interstellar clouds*. *Astrophysical Journal*, 2001. **553**(1): p. 267-273.
11. Monninger, G., Förderer, M., Gürtler, P., Kalhofer, S., Petersen, S., Nemes, L., Szalay, P.G., Krätschmer, W., *Vacuum ultraviolet spectroscopy of the carbon molecule C₃ in matrix isolated state: experiment and theory*. *Journal of Physical Chemistry A*, 2002. **106**(24): p. 5779-5788.
12. Forney, D., Freivogel, P., Grutter, M., Maier, J.P., *Electronic absorption spectra of linear carbon chains in neon matrices. IV. C_{2n+1} n=2-7*. *Journal of Chemical Physics*, 1996. **104**(13): p. 4954-4960.
13. Boguslavskiy, A.E., Ding, H., Maier, J.P., *Gas-phase electronic spectra of C₁₈ and C₂₂ rings*. *Journal of Chemical Physics*, 2005. **123**(3): p. 034305 1-7.
14. Dunbar, R.C., *Photofragmentation of molecular ions*. In *Molecular Ions: Spectroscopy, Structure, and Chemistry*, Ed. T.A. Miller And V.E. Bondybey. 1983, North-Holland: Amsterdam. 231.
15. Callomon, J.H., Creutzberg, F., *The electronic emission spectrum of ionized nitrous oxide, N₂O⁺: A ²Σ⁺ → X ²II*. *Philosophical Transactions of The Royal Society of London. Series A, Mathematical and Physical Sciences*, 1974. **277**(1266): p. 157-189.
16. Klapstein, D., Maier, J.P., *Lifetimes of N₂O⁺(A ²Σ⁺) and COS⁺(A ²II) in selected vibronic levels*. *Chemical Physics Letters*, 1981. **83**(3): p. 590-593.
17. Frey, R., Kakoschke, R., Schlag, E.W., *Spectroscopy of molecular ions: Laser-induced fragmentation spectra of N₂O⁺, A ²Σ⁺ ↔ X ²II*. *Chemical Physics Letters*, 1982. **93**(3): p. 227-231.
18. Larzillière, M., Jungen, Ch., *Fast ion beam laser spectroscopy of N₂O⁺. Effects of orbital angular momentum and vibrational anharmonicity*. *Molecular Physics*, 1989. **67**(4): p. 807-837.

19. Orth, R.G., Dunbar, R.C., *Photodissociation of nitrous oxide cation*. Journal of Chemical Physics, 1977. **66**(4): p. 1616-1620.
20. Maier, J.P., Marthaler, O., *Emission spectra of radical cations of 1,3-dichlorobenzene, 1,4-dichlorobenzene and 1,3,5-trichlorobenzene in the gas phase*. Chemical Physics, 1978. **32**(3): p. 419-427.
21. Friedman, R.S., Kelsall, B.J., Andrews, L., *Vibronic absorption spectra of dichloro- and dibromobenzene cations in solid argon at 20 K*. Journal of Physical Chemistry, 1984. **88**(10): p. 1944-1950.
22. Szczepanski, J., Personette, W., Pellow, R., Chandrasekhar, T.M., Roser, D., Cory, M., Zerner, M., Vala, M., *Vibrational and electronic spectra of matrix-isolated para-dichlorobenzene radical cations*. Journal of Chemical Physics, 1992. **96**(1): p. 35-43.
23. Motylewski, T., Linnartz, H., Vaizert, O., Maier, J.P., Galazutdinov, G.A., Musaev, F.A., Krelowski, J., Walker, G.A.H., Bohlender, D.A., *Gas-phase electronic spectra of carbon-chain radicals compared with diffuse interstellar band observations*. Astrophysical Journal, 2000. **531**(1): p. 312-320.
24. Khoroshev, D., Araki, M., Kolek, P., Birza, P., Chirokolava, A., Maier, J.P., *Rotationally resolved electronic spectroscopy of a nonlinear carbon chain radical $C_6H_4^+$* . Journal of Molecular Spectroscopy, 2004. **227**(1): p. 81-89.
25. Nolting, D., Marian, C., Weinkauff, R., *Protonation effect on the electronic spectrum of tryptophan in the gas phase*. Physical Chemistry Chemical Physics, 2004. **6**(10): p. 2633-2640.
26. Duncan, M.A., *Infrared spectroscopy to probe structure and dynamics in metal ion-molecule complexes*. International Reviews in Physical Chemistry, 2003. **22**(2): p. 407-435.

27. Pino, T., Boudin, N., Bréchnignac, P., *Electronic absorption spectrum of cold naphthalene cation in the gas phase by photodissociation of its van der Waals complexes*. Journal of Chemical Physics, 1999. **111**(16): p. 7337-7347.
28. Dzhonson, A., Gerlich, D., Bieske, E.J., Maier, J.P., *Apparatus for the study of electronic spectra of collisionally cooled cations: para-dichlorobenzene*. Journal of Molecular Structure, 2006. **795**(1-3): p. 93-97.
29. Dunbar, R.C., *Photodissociation of trapped ions*. International Journal of Mass Spectrometry, 2000. **200**(1-3): p. 571-589.
30. Duncan, M.A., *Frontiers in the spectroscopy of mass-selected molecular ions*. International Journal of Mass Spectrometry, 2000. **200**(1-3): p. 545-569.
31. Rolland, D., Specht, A.A., Blades, M.W., Hepburn, J.W., *Resonance enhanced multiphoton dissociation of polycyclic aromatic hydrocarbons cations in an RF ion trap*. Chemical Physics Letters, 2003. **373**(3-4): p. 292-298.
32. Klapstein, D., Leutwyler, S., Maier, J.P., *The emission spectrum of the 2,4-hexadiyne cation in a supersonic free jet*. Chemical Physics Letters, 1981. **84**(3): p. 534-538.
33. Maier, J.P., Misev, L., *Laser induced excitation spectra of the cations of 1,3-pentadienes, $R-(C\equiv C)-H_2^+$, $R = CH_3, CD_3$, ($A^2E \leftarrow X^2E$) and of 2,4-hexadienes, $R-(C\equiv C)-R_2^+$, $R = CH_3, CD_3$, ($A^2E_u \leftarrow X^2E_g$) in the gaseous phase*. Chemical Physics, 1980. **51**(3): p. 311-318.
34. Forster, P., Maier, J.P., Thommen, F., *Radiative and non-radiative decay rates of alkyl substituted diacetylene cations at selected energies within their 2A states determined via photoelectron-photon coincidence measurements*. Chemical Physics, 1981. **59**(1-2): p. 85-90.
35. Dannacher, J., *Photoelectron-photoion-coincidence measurements on 2,4-hexadiyne*. Chemical Physics, 1978. **29**(3): p. 339-344.

36. Freivogel, P., Fulara, J., Lessen, D., Forney, D., Maier, J.P., *Absorption spectra of conjugated hydrocarbon cation chains in neon matrices*. Chemical Physics, 1994. **189**(2): p. 335-341.
37. Smith, A.M., Agreiter, J., Härtle, M., Engel, C., Bondybey, V.E., *Rare gas matrix studies of absorption and fluorescence of reactive intermediates formed in discharges through acetylene*. Chemical Physics, 1994. **189**(2): p. 315-334.
38. Cias, P., Vaizert, O., Denisov, A., Mes, J., Linnartz, H., Maier, J.P., *Electronic gas-phase spectrum of the pentaacetylene cation*. Journal of Physical Chemistry A, 2002. **106**(42): p. 9890-9892.
39. Klapstein, D., Kuhn, R., Maier, J.P., Ochsner, M., Zambach, W., *Emission and laser excitation spectra of the $A^2\Pi_u \leftrightarrow X^2\Pi_g$ transition of rotationally cooled triacetylene cation*. Journal of Physical Chemistry, 1984. **88**(22): p. 5176-5180.
40. Lecoultre, J., Maier, J.P., Rösslein, M., *Geometric structure of diacetylene cation in the $X^2\Pi_g$ and $A^2\Pi_u$ electronic states*. Journal of Chemical Physics, 1988. **89**(10): p. 6081-6085.
41. Pfluger, D., Motylewski, T., Linnartz, H., Sinclair, W.E., Maier, J.P., *Rotationally resolved $A^2\Pi_u \leftarrow X^2\Pi_g$ electronic spectrum of tetraacetylene cation*. Chemical Physics Letters, 2000. **329**(1-2): p. 29-35.
42. Pfluger, D., Sinclair, W.E., Linnartz, H., Maier, J.P., *Rotationally resolved electronic absorption spectra of triacetylene cation in a supersonic jet*. Chemical Physics Letters, 1999. **313**(1-2): p. 171-178.
43. Sinclair, W.E., Pfluger, D., Linnartz, H., Maier, J.P., *Rotationally resolved $A^2\Pi_g \leftarrow X^2\Pi_u$ electronic spectrum of triacetylene cation by frequency modulation absorption spectroscopy*. Journal of Chemical Physics, 1999. **110**(1): P. 296-303.

44. Homann, K.-H., *Soot formation in premixed hydrocarbon flames*. *Angewandte Chemie-International Edition*, 1968. **7**(6): p. 414-427.
45. McCarthy, M.C, Travers, M.J., Kovács, A., Gottlieb, C.A., Thaddeus, P., *Eight new carbon chain molecules*. *Astrophysical Journal Supplement Series*, 1997. **113**(1): p. 105-120.
46. Shindo, F., Benilan, Y., Guillemin, J.-C., Chaquin, P., Jolly, A., Raulin, F., *Ultraviolet and infrared spectrum of C₆H₂ revisited and vapor pressure curve in Titan's atmosphere*. *Planetary and Space Science*, 2003. **51**(1): P. 9-17.
47. Tielens, A.G.G.M., Snow, T.P., editors, *The diffuse interstellar bands; Laboratory studies of proposed carriers*, Dordrecht, Kluwer, 1995, ISBN 0-7923-3629-1.
48. Kloster-Jensen, E., Haink, H.-J., Christen, H., *The electronic spectra of unsubstituted mono- to pentaacetylene in gas-phase and in solution in range 1100 to 4000 Å*. *Helvetica Chimica Acta*, 1974. **57**(6): p. 1731-1744.
49. Heath, J.R., Zhang, Q., O'Brien, S.C., Curl, R.F., Kroto, H.W., Smalley, R.E., *The formation of long carbon chain molecules during laser vaporization of graphite*. *Journal of the American Chemical Society*, 1987. **109**(2): p. 359-363.
50. Stein, S.E., Fahr, A., *High-temperature stabilities of hydrocarbons*. *Journal of Physical Chemistry*, 1985. **89**(17): p. 3714-3725.
51. Roberge, W.G., Jones, D., Lepp, S., Dalgarno, A., *Interstellar photodissociation and photoionization rates*. *Astrophysical Journal Supplement Series*, 1991. **77**(2): p. 287-297.
52. Allan, M., Heilbronner, E., Kloster-Jensen, E., Maier, J.P., *The II-states of tetraacetylene radical cation*. *Chemical Physics Letters*, 1976. **41**(2): p. 228-230.

53. Allan, M., Kloster-Jensen, E., Maier, J.P., *Emission spectra of radical cations of diacetylene ($A^2\Pi_u \rightarrow X^2\Pi_g$), triacetylene ($A^2\Pi_g \rightarrow X^2\Pi_u$) and tetraacetylene ($A^2\Pi_u \rightarrow X^2\Pi_g, 0_0^0$), and lifetimes of some vibronic levels of the A states.* Chemical Physics, 1976. **17**(1): p. 11-18.
54. Dzhonson, A., Jochnowitz, E.B., Kim, E., Maier, J.P., *Electronic absorption spectra of the protonated polyacetylenes $HC_{2n}H_2^+$ ($n=3, 4$) in the gas phase.* Journal of Chemical Physics, 2007. 126(4): p. 044301 1-5.
55. Kloster-Jensen, E., Haink, H.-J., Christen, H., *The electronic spectra of unsubstituted mono- to pentaacetylene in gas-phase and in solution in range 1100 to 4000 $\overset{0}{\text{A}}$.* Helvetica Chimica Acta, 1974. **57**(6): p. 1731-1744.
56. Pino, T., Ding, H.B., Güthe, F., Maier, J.P., *Electronic spectra of the chains $HC_{2n}H$ ($n=8-13$) in the gas phase.* Journal of Chemical Physics, 2001. **114**(5): p. 2208-2212.
57. Anand, S., Schlegel, H.B., *Dissociation of benzene dication $[C_6H_6]^{2+}$: exploring the potential energy surface.* Journal of Physical Chemistry A, 2005. **109**(50): p. 11551-11559.
58. Botschwina, P., Schramm, H., Sebald, P., *A theoretical investigation of $H_2C_4H^+$ and the proton affinity of HC_4H .* Chemical Physics Letters, 1990. **169**(1-2): p. 121-126.
59. Petrie, S., Knight, J.S., Freeman, C.G., MacLagan, R.G.A.R., McEwan, M.J., Sudkeaw, P., *The proton affinity and selected ion/molecule reactions of diacetylene.* International Journal of Mass Spectrometry and Ion Processes, 1991. **105**(1): p. 43-54.
60. Schröder, D., Loos, J., Schwarz, H., Thissen, R., Roithova, J., Herman, Z., *Does ionized diacetylene have a positive proton affinity?* International Journal of Mass Spectrometry, 2003. **230**(2-3): p. 113-121.

61. Deakyne, C.A., Meot-Ner (Mautner), M., Buckley, T.J., Metz, R., *Proton affinities of diacetylene, cyanoacetylene, and cyanogen*. Journal of Chemical Physics, 1987. **86**(4): p. 2334-2342.
62. Scott, G.B.I., Fairley, D.A., Freeman, C.G., McEwan, M.J., Adams, N.G., Babcock, L.M., *$C_mH_n^+$ reactions with H and H₂: an experimental study*. Journal of Physical Chemistry A, 1997. **101**(27): p. 4973-4978.
63. Batalov, A., Fulara, J., Shnitko, I., Maier, J.P., *Electronic absorption spectra of the protonated polyacetylenes H₂C_nH⁺ (n=4, 6, 8) in neon matrixes*. Journal of Physical Chemistry A, 2006. **110**(35): p. 10404-10408.
64. Turner, B.E., Herbst, E., Terzieva, R., *The physics and chemistry of small translucent molecular clouds. XIII. The basic hydrocarbon chemistry*. Astrophysical Journal Supplement Series, 2000. **126**(2): p. 427-460.
65. Araki, M., Cias, P., Denisov, A., Fulara, J., Maier, J.P., *Electronic spectroscopy of the nonlinear carbon chains C₄H₄⁺ and C₈H₄⁺*. Canadian Journal of Chemistry, 2004. **82**(6): p. 848-853.
66. Birza, P., Motylewski, T., Khoroshev, D., Chirokolava, A., Linnartz H., Maier, J.P., *CW cavity ring down spectroscopy in a pulsed planar plasma expansion*. Chemical Physics, 2002. **283**(1-2): p. 119-124.
67. Dzhonson, A., Maier, J.P., *Electronic absorption spectra of cold organic cations: 2,4-hexadiyne*. International Journal of Mass Spectrometry, 2006. **255**: p. 139-143.
68. Daly, N.R., *Scintillation type mass spectrometer ion detector*. Review of Scientific Instruments, 1960. **31**(3): p. 264-267.
69. McLachlan, N.W., *Theory and applications of Mathieu functions*. 1947, New York: Oxford University Press.

70. Röttgen, M., Judai, K., Antonietti, J.-M., Heiz, U., Rauschenbach, S., Kern, K., *Conical octopole ion guide: design, focusing, and its application to the deposition of low energetic clusters*. Review of Scientific Instruments, 2006. **77**(1): p. 013302 1-6.
71. Gerlich, D., *Ion-neutral collisions in a 22-pole trap at very low energies*. Physica Scripta, 1995. **T59**: p. 256-263.
72. Parks, J.H., Pollack, S., Hill, W., *Cluster experiments in radio frequency Paul traps: Collisional relaxation and dissociation*. Journal of Chemical Physics, 1994. **101**(8): p. 6666-6685.
73. Schlemmer, S., Lescop, E., Richthofen, J.V., Gerlich, D., Smith, M.A., *Laser induced reactions in a 22-pole ion trap: $C_2H_2^+ + hv_3 + H_2 \rightarrow C_2H_3^+ + H$* . Journal of Chemical Physics, 2002. **117**(5): p. 2068-2075.
74. Gerlich, D., *Inhomogeneous RF fields: a versatile tool for the study of processes with slow ions*. Advances in Chemical Physics, 1992. **82**(1): p. 1-176.
75. Jones, R., Gerlich, D., Anderson, S.L., *Simple radio-frequency power source for ion guides and ion traps*. Review of Scientific Instruments, 1997. **68**(9): p. 3357-3362.
76. Tan, X. *Diatomic: A powerful spectral simulation program for diatomic molecules*. In The Ohio State University 57th International Symposium on Molecular Spectroscopy. 2002. Columbus.
77. Tan, X., *Diatomic: A spectral simulation program for diatomic molecules on windows platforms*, Release 1.28 ed., 2004.
78. Klapstein, D., Kuhn, R., Leutwyler, S., Maier, J.P., *Emission spectra of supersonically cooled dimethyldiacetylene cations*. Chemical Physics, 1983. **78**(2): p. 167-173.

79. Leutwyler, S., Klapstein, D., Maier, J.P., *Emission spectra of supersonically cooled methyldiacetylene cations*. Chemical Physics, 1983. **78**(2): p. 151-166.
80. Nielsen, C.J., *The vibrational spectra of 2,4-hexadiyne (dimethyldiacetylene), 2,4-hexadiyne- d_6 and 2,4-hexadiyne-1,1,1- d_3* . Spectrochimica Acta, Part A: Molecular and Biomolecular Spectroscopy, 1983. **39A**(11): p. 993-1005.
81. Muntean, F., Heumann, L., Armentrout, P.B., *Modeling kinetic shifts in threshold collision-induced dissociation. Case study: Dichlorobenzene cation dissociation*. Journal of Chemical Physics, 2002. **116**(13): p. 5593-5602.
82. Green, J.H.S., *Vibrational spectra of benzene derivatives - VI: p-Disubstituted compounds*. Spectrochimica Acta Part A: Molecular Spectroscopy, 1970. **26**(7): p. 1503-1513.
83. Rohlfig, E.A., Rohlfig, C.M., *Resonant two-photon ionization spectroscopy of jet-cooled p-dichlorobenzene*. Journal of Physical Chemistry, 1989. **93**(1): p. 94-101.
84. Sands, W.D., Moore, R., *Fluorescence excitation spectroscopy of jet cooled p-dichlorobenzene and p-dichlorobenzene- d_4* . Journal of Physical Chemistry, 1989. **93**(1): p. 101-107.
85. Olesik, S., Baer, T., Morrow, J.C., *Dissociation rates of energy-selected dichloro- and dibromobenzene ions*. Journal of Physical Chemistry, 1986. **90**(16): p. 3563-3568.
86. Sasaki, T., Mikami, N., *Trapped ion photodissociation spectroscopy. Photodissociation of p-dichlorobenzene cation*. Chemical Physics Letters, 1993. **209**(4): p. 379-382.
87. Maier, J.P., Thommen, F., *Radiative and nonradiative decay rates of state selected $H-(C\equiv C)_2-H^+$, $D-(C\equiv C)_2-D^+$, $A^2\Pi_u$ determined by a photoelectron-*

- photon coincidence technique*. Journal of Chemical Physics, 1980. **73**(11): p. 5616-5619.
88. Pgopher, *A program for simulating rotational structure*. <http://pgopher.chm.bris.ac.uk>.
89. Komiha, N., Rosmus, P., Maier, J.P., *Low lying quartet states in diacetylene, triacetylene and benzene radical cations*. Molecular Physics, 2006. **104**(20-21): p. 3281-3285.
90. Becke, A.D., *Density-functional thermochemistry. III. The role of exact exchange*. Journal of Chemical Physics, 1993. **98**(7): p. 5648-5652.
91. Lee, C., Yang, W., Parr, R.G., *Development of the Colle-Salvetti correlation-energy formula into a functional of the electron density*. Physical Review B, 1988. **37**(2): p. 785-789.
92. Araki, M., Motylewski, T., Kolek, P., Maier, J.P., *Electronic absorption spectrum of a nonlinear carbon chain: trans-C₆H₄⁺*. Physical Chemistry Chemical Physics, 2005. **7**(10): p. 2138-2141.
93. Cox, N.L.J., Kaper, L., Foing, B.H., Ehrenfreund, P., *Diffuse interstellar bands of unprecedented strength in the line of sight towards high-mass X-ray binary 4U 1907+09*. Astronomy & Astrophysics, 2005. **438**(1): p. 187-199.
94. Galazutdinov, G.A., Musaev, F.A., Krelowski, J., Walker, G.A.H., *Narrow diffuse interstellar bands: a survey with precise wavelengths*. The Astronomical Society of the Pacific, 2000. **112**(771): p. 648-690.
95. Jenniskens, P., Desert, F.-X., *A survey of diffuse interstellar bands (3800-8680 Å⁰)*. Astronomy & Astrophysics Supplement Series, 1994. **106**(1): p. 39-78.

96. Tuairisg, S.O., Cami, J., Foing, B.H., Sonnentrucker, P., Ehrenfreund, P., *A deep echelle survey and new analysis of diffuse interstellar bands*. *Astronomy & Astrophysics Supplement Series*, 2000. **142**(2): p. 225-238.
97. Watson, J.K.G., *Homologous series of diffuse interstellar bands*. *Astrophysical Journal*, 1994. **437**(2): p. 678-682.

Curriculum Vitae

Personal

Name: Anatoly G. Dzhonson
Address: Byfangweg 6,
CH-4051 Basel
Switzerland
Office Phone: +41612673806
Mobile phone: +41764144267
Private phone: +41335349997
E-mail: Anatoly.Dzhonson@unibas.ch
Home Page: <http://www.chemie.unibas.ch/~dzhonson>
Date of birth: October 28th, 1978
Place of birth: Poronaisk, Sakhalin region, Russia
Marital status: Single
Children: No
Citizenship: Russian Federation



Education

- 2002 - 2007** **PhD-student**, Research Group of Prof. Dr. J.P. Maier. Department of Chemistry, University of Basel, Switzerland. **PhD completion in February 2007.**
- 2000 - 2002** Novosibirsk State University, Department of Natural Sciences, Novosibirsk, Russia. **Master Diploma in Physical Chemistry, 2002.**
- 1996 - 2000** Novosibirsk State University, Department of Natural Sciences, Novosibirsk, Russia. **Bachelor Diploma in Chemistry, Ecology and Management of Nature, 2000.**
- 1994 - 1996** Specialized Scientific Study Center of Novosibirsk State University, Novosibirsk, Russia.
- 1986 - 1994** Primary and Secondary School №2, Poronaisk, Sakhalin region, Russia.

List of publications

- A.G. Dzhonson, E.B. Jochnowitz, and J.P. Maier “**Electronic gas-phase spectra of lager polyacetylene cations**”. *Journal of Physical Chemistry, In Press*.
- A.G. Dzhonson, E.B. Jochnowitz, E. Kim, and J.P. Maier “**Electronic absorption spectra of the protonated polyacetylenes $\text{HC}_{2n}\text{H}_2^+$ (n=3, 4) in the gas phase**”. *Journal of Chemical Physics, Volume 126, January 2007, Pages 044301 1-5*.
- A.G. Dzhonson and J.P. Maier “**Electronic absorption spectra of cold organic cations: 2,4-hexadiyne**”. *International Journal of Mass Spectrometry, Volume 255, October 2006, Pages 139-143*.
- A.G. Dzhonson, D. Gerlich, E.J. Bieske and J.P. Maier “**Apparatus for the study of electronic spectra of collisionally cooled cations: para-dichlorobenzene**”. *Journal of Molecular Structure, Volume 795, Issues 1-3, August 2006, Pages 93-97*.
- V.M. Syutkin, B.V. Bol'shakov and A.G. Dzhonson “**On the relation between oxygen diffusion and secondary relaxation in glassy n-butanol**”. *Chemical Physics, Volume 324, Issues 2-3, May 2006, Pages 307-313*.
- A.E. Boguslavskiy, A.G. Dzhonson, and J.P. Maier “**The electronic spectra of carbon chains, rings, and ions of astrophysical interest**”. *Astrochemistry; From laboratory studies to astronomical observations, Volume 855, December 2005, Pages 201-208*.
- B.V. Bolshakov and A.G. Dzhonson “**On the number of amorphous phases in n-butanol: Kinetics of free radicals oxidation by oxygen in frozen n-butanol**”. *Journal of Non-Crystalline Solids, Volume 351, Issue 5, March 2005, Pages 444-454*.
- B.V. Bolshakov and A.G. Dzhonson “**On the number of amorphous phases in n-butanol**”. *Doklady Physical Chemistry, Volume 393, Numbers 1-3, November 2003, Pages 318-320(3)*.